

DISSERTATION

BALANCED AND TRANSIENT ASPECTS OF THE INTERTROPICAL CONVERGENCE
ZONE

Submitted by

Alex O. Gonzalez

Department of Atmospheric Science

In partial fulfillment of the requirements

For the Degree of Doctor of Philosophy

Colorado State University

Fort Collins, Colorado

Summer 2015

Doctoral Committee:

Advisor: Wayne H. Schubert

Eric D. Maloney

Thomas Birner

Donald J. Estep

Copyright by Alex O. Gonzalez 2015

All Rights Reserved

ABSTRACT

BALANCED AND TRANSIENT ASPECTS OF THE INTERTROPICAL CONVERGENCE ZONE

The Intertropical Convergence Zone (ITCZ) is one of the primary drivers of tropical circulations and because of its interactions with the extratropics, contributes significantly to Earth's general circulation. This dissertation investigates dynamical aspects of the ITCZ using a variety of analytical and numerical models.

In the first chapter, we learn that deep and shallow balanced Hadley circulations are forced by deep diabatic heating and Ekman pumping at the top of the boundary layer, respectively. Also, when the ITCZ is located off of the equator there is an inherent asymmetry between the winter and summer Hadley cells due to the anisotropic nature of the inertial stability.

The second study examines shallow and deep vertical motions over the eastern Pacific Ocean (80°W – 150°W) using the Year of Tropical Convection reanalysis (YOTC). Vertical motions in the eastern Pacific tend to be bimodal, with both shallow and deep vertical motions occurring throughout the year. Shallow vertical motions are typically narrow and restricted to low latitudes (ITCZ-like) while deep vertical motions tend to be broad and are located poleward of shallow regimes, except during El Niño conditions.

The study of balanced Hadley circulations is also extended to investigate the role of transient aspects of the Hadley circulation. The solutions illustrate that inertia-gravity wave packets emanate from the ITCZ and bounce off a spectrum of turning latitudes when the ITCZ is switched on at various rates. These equatorially trapped wave packets cause the Hadley cells to pulsate with periods of 1–3 days.

In the last part of this dissertation, we focus on boundary layer aspects of the formation of the ITCZ. Since the ITCZ boundary layer is a region of significant meridional convergence, meridional advection should not be neglected. Using a zonally symmetric slab boundary layer model, shock-like structures appear in the form of near discontinuities in the horizontal winds and near singularities in the vorticity and Ekman pumping after 1–2 days. The numerical model also agrees well with dynamical fields in YOTC while adding important details about the boundary layer pumping and vorticity.

In closing, we believe that the ITCZ is a highly transient region vital to the general circulation of the atmosphere, and many of its features can be explained by dry dynamics.

ACKNOWLEDGMENTS

First and foremost, I must thank my advisor, Dr. Wayne H. Schubert. He has provided me with an unbelievable amount of insight and inspiration. His work ethic is like no one I have ever met and he is one of the nicest people I know. These characteristics have made him an amazing mentor and friend. Next I would like to thank my fiancée, Bridget. She has been there through my ups and downs as a graduate student, and she has always encouraged me. I also could not have gotten through graduate school without the support of my family and closest friends. They have also been very supportive throughout my time at CSU. I would like to thank my committee: Dr. Donald J. Estep, Dr. Eric D. Maloney, and Dr. Thomas Birner for their time and insight on this project. I would also like to thank the SOARS program as well as CMMAP for the financial support and career opportunities at conferences and NCAR. Finally, I have to thank the Schubert Research Group for their technical help and words of encouragement. Thanks to Rick Taft for providing me with technical help when I needed it, especially when it came to debugging my Fortran code. Thank you Paul Ciesielski, for help with observational data and for giving me suggestions on parts of my manuscripts. And last but not least, thanks Chris Slocum for putting up with me as an officemate. We both were always productive but it was always nice to have stimulating conversations, whether it be about our work or about politics or whatever else.

Research support has been provided by the National Science Foundation under Grants ATM-0837932 and AGS-1250966, and under the Science and Technology Center for Multi-Scale Modeling of Atmospheric Processes, managed by Colorado State University through cooperative agreement No. ATM-0425247.

TABLE OF CONTENTS

Abstract	ii
Acknowledgments	iv
Chapter 1. Introduction	1
Chapter 2. Balanced Dynamics of Deep and Shallow Hadley Circulations	4
2.1. Synopsis	4
2.2. Introduction	5
2.3. Model equations	8
2.4. Vertical transform	13
2.5. Solution of the horizontal structure equation via the Green's function	16
2.6. Deep overturning circulations	21
2.7. Shallow overturning circulations	29
2.8. Asymmetrical nature of the Hadley circulation	39
2.9. Concluding remarks	44
Chapter 3. Deep and Shallow Vertical Motions in the Tropical Eastern Pacific in the YOTC reanalysis	48
3.1. Synopsis	48
3.2. Introduction	49
3.3. Data	50
3.4. Results	51
3.5. Concluding remarks	59

Chapter 4. Transient Hadley Circulations	63
4.1. Synopsis	63
4.2. Introduction	64
4.3. Model equations	68
4.4. Solution via Hermite transforms	71
4.5. Transient Hadley circulations forced by a switch-on of ITCZ convection	74
4.6. Examples using $m = 0, 1, 2$ diabatic heating	78
4.7. Analysis of the inertia-gravity wave packets	90
4.8. Concluding remarks	93
Chapter 5. Shock-like Structures in the ITCZ Boundary Layer	96
5.1. Synopsis	96
5.2. Introduction	96
5.3. Slab boundary layer model	102
5.4. Heuristic argument I	104
5.5. Heuristic argument II	111
5.6. Numerical simulation of ITCZ shocks - Idealized u_g forcing	118
5.7. Numerical simulation of ITCZ shocks - YOTC reanalysis forcing	132
5.8. Concluding remarks	142
References	144
Appendix A. Vertical transform	151
Appendix B. Calculation of h_m and $\mathcal{Z}_m(z)$	154
Appendix C. Characteristic form	159

CHAPTER 1

Introduction

The tropical atmosphere is a vital component in Earth's weather and climate. It plays a significant role in transporting energy, momentum, and moisture poleward. One of the primary drivers of tropical-extratropical transport is the Hadley circulation (Halley 1686; Hadley 1735; Held and Hou 1980; Hoskins 1996). Until recently, the Hadley circulation was thought to have been mostly driven by deep convection in the Intertropical Convergence Zone (ITCZ) (Schneider and Lindzen 1977; Held and Hou 1980; Lindzen and Hou 1988; Hack et al. 1989). Now we know that shallow convection and boundary layer processes in the ITCZ play a significant role in the exchange of energy, momentum, and moisture between the tropics and the extratropics (Lindzen and Nigam 1987; Stevens et al. 2002; Zhang et al. 2004; Zhang and Hagos 2009; Back and Bretherton 2009a).

Chapter 2 of this dissertation explores analytical solutions for deep and shallow Hadley circulations in a zonally symmetric framework. The results suggest that both Hadley circulations can be described by the same partial differential equations with the same shaping parameters. Therefore, the asymmetries between the winter and summer hemisphere Hadley cells are a part of the same dynamical system, with the main difference being their forcing. In the deep Hadley circulation diabatic heating in the ITCZ is the main forcing, while Ekman pumping at the top of the ITCZ boundary layer is the primary forcing for the shallow Hadley circulation.

The next chapter focuses on shallow and deep vertical motions over the eastern Pacific Ocean (80°W – 150°W) using the Year of Tropical Convection reanalysis (YOTC). YOTC was a two year

project of enhanced satellite coverage, especially over the tropical oceans, where the transient dynamics are not well understood. The analysis that is performed characterizes the vertical profile of the vertical motion as either being shallow or deep. Along with an analysis of sea surface temperatures and diabatic heating, it appears that shallow vertical motions are typically narrow and restricted to low latitudes (ITCZ-like) while deep vertical motions tend to be broad and typically are found poleward of shallow regimes, except during the El Niño conditions of May 2009–April 2010. During the summer months of May–October, deeper rising motions seem to correspond with warmer sea surface temperatures while the months of February–April exhibit significant differences near the equator. In particular, February–April 2009 illustrate a double shallow ITCZ structure, while February–April 2010 had a single ITCZ just north of the equator with both shallow and deep rising motions.

In Chapter 4, we extend the study of balanced, zonally symmetric Hadley circulations to investigate the role of transient aspects of the zonally symmetric Hadley circulation. We mainly focus on the Hadley circulations forced by diabatic heating of the external mode and first two internal modes. The solutions illustrate the fundamental result that inertia-gravity wave packets emanate from the ITCZ and bounce off a spectrum of turning latitudes when the ITCZ is switched on at various rates. These packets are therefore equatorially trapped and cause the Hadley cells to pulsate with periods of 1–3 days. Past studies, such as Wunsch and Gill (1976), have shown evidence of equatorially-trapped oceanic inertia-gravity waves in sea level and surface meridional wind data over the Pacific Ocean. It is possible that the tropical atmosphere may contain a considerable amount of inertia-gravity wave activity which our present observational systems are not capable of detecting. Therefore, this theoretical work serves as motivation for future observational work on inertia-gravity waves in the tropics.

Chapters 2–4 analyze dynamical aspects of deep and shallow overturning circulations strictly above the boundary layer. Also, we made a number of simplifying assumptions about the dynamical and thermodynamical processes in the ITCZ, which act as the primary forcing for large-scale tropical circulations. In the final chapter, we devise a high-resolution, zonally symmetric, slab boundary layer model to study dynamical aspects in the ITCZ. The main motivation for this work is recent research showing evidence of shock-like structures in the boundary layer of tropical cyclones (Williams et al. 2013; Slocum et al. 2014). Also, satellite imagery often shows narrow zonally elongated strips of tropical convection, especially in the central and eastern Pacific. When the boundary layer meridional inflow is large enough in the ITCZ, the neglect of the meridional advection terms is not justifiable. With the inclusion of these terms in the slab boundary layer model an embedded Burgers’ equation (Burgers 1948) appears in the meridional momentum equation. When the model is forced by a broad low pressure region just above the boundary layer, near discontinuities form in both the zonal and meridional winds after about 2 days. Along with these near discontinuities, near singularities arise in the vorticity and Ekman pumping. The numerical model also agrees well with dynamical fields in YOTC while adding important details about the boundary layer pumping and vorticity.

CHAPTER 2

Balanced Dynamics of Deep and Shallow Hadley Circulations

2.1. SYNOPSIS

This chapter examines the dynamics of large-scale overturning circulations in the tropical atmosphere using an idealized zonally symmetric model on the equatorial β -plane. Under certain simplifications of its coefficients, the elliptic partial differential equation for the transverse circulation can be solved by first performing a vertical transform to obtain a horizontal structure equation, and then using Green's function to solve the horizontal structure equation. When deep diabatic heating is present in the Intertropical Convergence Zone (ITCZ), the deep Hadley circulation is of first order importance. In the absence of deep diabatic heating, the interior circulation associated with Ekman pumping cannot penetrate deep into the troposphere because the resistance of fluid parcels to horizontal motion (i.e., inertial stability) is significantly smaller than their resistance to vertical motion (i.e., static stability). In this scenario, only a shallow Hadley circulation exists. The shallow overturning circulation is characterized by meridional velocities as large as 7 m s^{-1} at the top of the boundary layer, in qualitative agreement with observations in the tropical eastern Pacific. The meridional asymmetry between the winter and summer deep and shallow Hadley cells is attributed to the anisotropy of the inertial stability parameter, and as the ITCZ widens meridionally or as the forcing involves higher vertical wavenumbers, the asymmetry between the winter and summer cells increases.

2.2. INTRODUCTION

Zhang et al. (2004) have presented comprehensive observations of shallow meridional overturning circulations in the tropical eastern Pacific. As illustrated in Fig. 2.1, this shallow overturning circulation resembles the deep Hadley circulation in many respects, but its cross-equatorial return flow is located just above the top of the boundary layer instead of just below the tropopause. Schneider and Lindzen (1977), Tomas and Webster (1997), and Trenberth et al. (1997) emphasized the importance of shallow overturning circulations in the tropics before the observations in Zhang et al. (2004).

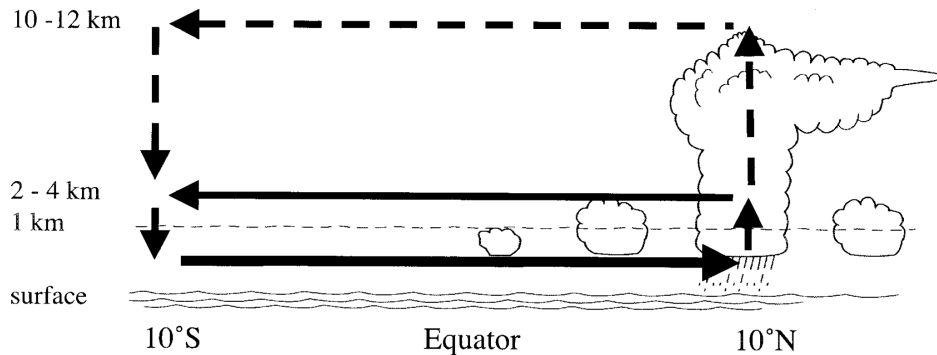


FIG. 2.1. Schematic cross section of the deep (dashed lines) and shallow (solid lines) meridional circulations in the tropical eastern Pacific. Adapted from Figure 1 of Zhang et al. (2004), © American Meteorological Society, and used with permission.

Schneider and Lindzen (1977) illustrated a large-scale overturning circulation confined below 800 hPa forced by a zonally symmetric sea surface temperature (SST) distribution. They explain that the circulation is confined to the boundary layer due to the vertical variation of small-scale turbulent mixing that they assumed. Tomas and Webster (1997) suggested that a shallow divergent circulation exists in all tropical ocean basins, but is most prominent in basins such as the eastern Pacific, where cross equatorial SST gradients are strongest. They describe the shallow overturning circulation as a secondary circulation that acts to advect absolute vorticity across the equator,

allowing the Intertropical Convergence Zone (ITCZ) to form off of the equator. Trenberth et al. (1997) performed an Empirical Orthogonal Function (EOF) analysis on the divergent part of the tropical wind field in the National Centers for Environmental Prediction–National Center for Atmospheric Research (NCEP–NCAR) and European Centre for Medium-Range Weather Forecasts (ECMWF) global model reanalysis products in the tropics. The first EOF mode represented deep overturning circulations while the second EOF mode represented shallow overturning circulations. Shallow overturning circulations were present in the eastern Pacific, west Africa, the Atlantic, North America, and South America. Yin and Albrecht (2000) also provided observations of shallow overturning circulations in the eastern Pacific (90°-150°W) using the First Global Atmospheric Research Program (GARP) Global Experiment (FGGE) dropsonde sounding data.

Motivated by the observations of Zhang et al. (2004), Nolan et al. (2007) interpreted the shallow overturning circulation in the eastern Pacific as a large-scale sea breeze circulation, driven by anomalously large north-south SST gradients when deep convection is absent in the ITCZ. The ITCZ of the eastern Pacific is an area of relatively low surface pressure and warm SSTs compared to the area near and just south of the equator, leading to a cross-equatorial southerly flow in the boundary layer. The ITCZ region has larger thicknesses between pressure levels since it is warmer, which leads to a reversal in the meridional pressure gradient and an associated shallow northerly return flow just above the boundary layer. Equatorial regions with significant large-scale cold tongues, such as the eastern Pacific, and coastal regions with land-ocean contrasts, such as west Africa, exhibit large enough surface temperature gradients to have this meridional pressure gradient reversal. Zhang et al. (2008) classify shallow overturning circulations into two types: (i) the maritime ITCZ type (e.g., the eastern Pacific) and (ii) the summer monsoon type (e.g., west

Africa). They also note that shallow overturning circulations have a seasonal cycle, can be located on either side of the ITCZ, and have distinct vertical structures.

The purpose of the present chapter is to discuss several other dynamical aspects, which, in addition to surface temperature gradients, appear to play an important role in understanding shallow overturning circulations. The main dynamical aspects discussed here are: (i) diabatic heating in the inviscid interior of the ITCZ; (ii) Ekman pumping out of the boundary layer in the high positive vorticity region of the ITCZ; (iii) low inertial stability in the equatorial region, causing the winter Hadley cell to be stronger than the summer cell in response to both diabatic and frictional forcings.

Such ideas are similar to those considered by Schubert and McNoldy (2010), who studied Ekman pumping at the top of the boundary layer in tropical cyclones. They illustrated the existence of shallow overturning circulations with return flow just above the top of the boundary layer in tropical cyclones of varying strengths using an axisymmetric model on the f -plane. The analogous model in the ITCZ is a zonally symmetric model on the equatorial β -plane, which will be used in this study.

As we will see, the zonally symmetric model equations help explain both shallow overturning circulations and the deep Hadley circulation, therefore they are useful in discussing both circulations in the context of one theory of large-scale flows in the ITCZ. There are two schools of thought in modeling flows in the ITCZ. The first involves an assumption of monthly or longer time scales, as shown by Schneider and Lindzen (1977), Held and Hou (1980), Lindzen and Hou (1988), and Hou and Lindzen (1992). The model used in this study focuses on the second school of thought, in which the zonal velocity and temperature fields are transient, as explored by Hack et al. (1989), Hack and Schubert (1990), Nieto Ferreira and Schubert (1997), and Wang and Magnusdottir (2005). If the zonal flow is balanced in the sense that it is continuously evolving from

one geostrophically balanced state to another, then the meridional circulation is determined by the solution of a second order partial differential equation in the (y, z) -plane (Eliassen 1951). According to this “meridional circulation equation,” the streamfunction for the meridional and vertical motion in the inviscid interior is forced by the meridional derivative of the diabatic heating and the Ekman pumping, and is shaped by the static stability, baroclinicity, and inertial stability. Although solutions of the meridional circulation equation generally yield meridional and vertical velocities that are much weaker than the zonal velocity, the meridional and vertical directions are the directions of large gradients, so the relatively weak meridional circulation is crucial for the temporal evolution of the zonal flow.

The chapter is organized in the following way. In section 2.3, the balanced zonally symmetric model and the associated meridional circulation equation are presented. Section 2.4 introduces a vertical transform that converts the meridional circulation equation into a differential equation for the y -structure of the circulation. In section 2.5, the differential equation in y is solved using the Green’s function. Section 2.6 discusses the deep overturning response associated with diabatic heating in the ITCZ. Section 2.7 discusses the shallow overturning response due to Ekman pumping at the top of boundary layer in the absence of diabatic heating. In section 2.8, solutions describing the asymmetry between the winter and summer Hadley cells are presented. Concluding remarks are made in section 2.9.

2.3. MODEL EQUATIONS

Consider zonally symmetric balanced motions in a stratified and compressible atmosphere on the equatorial β -plane. Only the flow in the inviscid interior (i.e., above the 900 hPa isobaric surface) is explicitly modeled. Frictional effects are represented through the specification of the Ekman pumping at the top of the boundary layer, $z = 0$. This nonzero lower boundary condition

will be discussed later in this section. As the vertical coordinate, $z = H \ln(p_0/p)$ is used, where $p_0 = 900$ hPa, $T_0 = 293$ K, and $H = RT_0/g = 8581$ m. This study considers the case of weak horizontal flow and weak baroclinicity (i.e., the $v(\partial u/\partial y)$ and $w(\partial u/\partial z)$ terms in the zonal momentum equation and the $v(\partial T/\partial y)$ term in the thermodynamic equation are neglected). These simplifications allow us to construct analytical solutions of the problem. As will be seen, these analytical results agree well with the numerical results obtained by Hack et al. (1989), who did not assume weak horizontal flow and weak baroclinicity and whose elliptic equation coefficients for static stability, baroclinicity, and inertial stability do not contain approximations.

Under these assumptions, the governing equations for balanced zonal flow are of the form

$$\frac{\partial u}{\partial t} - \beta y v = 0, \quad (2.1)$$

$$\frac{\partial v}{\partial t} + \beta y u + \frac{\partial \phi}{\partial y} = 0, \quad (2.2)$$

$$\frac{\partial \phi}{\partial z} = \frac{g}{T_0} T, \quad (2.3)$$

$$\frac{\partial v}{\partial y} + \frac{\partial w}{\partial z} - \frac{w}{H} = 0, \quad (2.4)$$

$$\frac{\partial T}{\partial t} + \frac{T_0}{g} N^2 w = \frac{Q}{c_p}, \quad (2.5)$$

where u and v are the zonal and meridional components of velocity, w is the log-pressure vertical velocity, ϕ is the perturbation geopotential, T is the perturbation temperature, $\beta = 2\Omega/a$ is the constant northward gradient of the Coriolis parameter, Ω and a are the Earth's rotation rate and radius, Q is the diabatic heating, and $N^2(z) = (g/T_0)[(d\bar{T}/dz) + (\kappa\bar{T}/H)]$ is the square of the buoyancy frequency, which is computed from the specified mean temperature profile $\bar{T}(z)$. Equations (2.1)–(2.5) constitute a system of five equations in the six unknowns u, v, w, ϕ, T, Q , so an

additional “parameterization” relating Q to the other unknowns is required for closure. In order to simplify the problem, Q will be prescribed.

Equations (2.1)–(2.5) can be combined in such a way as to obtain a single equation for the streamfunction of the meridional overturning circulation. We begin the derivation by multiplying the zonal wind equation (2.1) by βy and the thermodynamic equation (2.5) by (g/T_0) , and we make use of the meridional momentum equation (2.2) and the hydrostatic equation (2.3), thereby obtaining

$$\frac{\partial}{\partial y} \left(\frac{\partial \phi}{\partial t} \right) + \left(\frac{\partial^2}{\partial t^2} + \beta^2 y^2 \right) v = 0, \quad (2.6)$$

$$\frac{\partial}{\partial z} \left(\frac{\partial \phi}{\partial t} \right) + N^2 w = \frac{g}{c_p T_0} Q. \quad (2.7)$$

Eliminating $(\partial \phi / \partial t)$ between (2.6) and (2.7) results in

$$N^2 \frac{\partial w}{\partial y} - \left(\frac{\partial^2}{\partial t^2} + \beta^2 y^2 \right) \frac{\partial v}{\partial z} = \frac{g}{c_p T_0} \frac{\partial Q}{\partial y}. \quad (2.8)$$

Equations (2.4) and (2.8) can now be regarded as a closed system in v and w . One way of proceeding from this system is to make use of (2.4) so that the meridional circulation (v, w) can be expressed in terms of the streamfunction ψ . The formulas that relate (v, w) and ψ are

$$e^{-z/H} v = -\frac{\partial \psi}{\partial z} \quad \text{and} \quad e^{-z/H} w = \frac{\partial \psi}{\partial y}. \quad (2.9)$$

In order to obtain a single equation in $\psi(y, z, t)$, we substitute (2.9) into (2.8). This procedure yields the partial differential equation given below in (2.10). Assuming that $v \rightarrow 0$ as $y \rightarrow \pm\infty$ and that w vanishes at the top boundary ($z = z_T$), the boundary conditions given below in (2.11) and (2.12) are obtained. Since this study is concerned with Ekman pumping effects on the fluid interior, the actual vertical velocity (i.e., the physical height vertical velocity) is specified at the lower

isobaric surface $z = 0$. Even though the lower boundary condition should be applied at a fixed physical height, Haynes and Shepherd (1989) suggest that the errors associated with assuming a value for the physical height vertical velocity on an isobaric lower boundary are minor compared to those associated with assuming a value for the log-pressure (or just pressure) vertical velocity on an isobaric lower boundary. The appropriate linearized version of the lower boundary condition used here is

$$\frac{\partial\phi}{\partial t} + g\frac{\partial\psi}{\partial y} = g\mathcal{W} \text{ at } z = 0,$$

where $\mathcal{W}(y, t)$ is the specified physical height vertical velocity at $z = 0$. Equation (2.6) must be used to eliminate $(\partial\phi/\partial t)$ and thereby express the lower boundary condition in terms of the streamfunction. From (2.6),

$$\frac{\partial}{\partial y} \left(\frac{\partial\phi}{\partial t} \right) - \left(\frac{\partial^2}{\partial t^2} + \beta^2 y^2 \right) \frac{\partial\psi}{\partial z} = 0 \text{ at } z = 0.$$

Eliminating $(\partial\phi/\partial t)$ from these last two relations, we obtain the lower boundary condition given below in (2.13). Concerning the initial conditions, we assume that the meridional circulation and its tendency both vanish at $t = 0$. In summary, the meridional circulation problem is

$$\left(\frac{\partial^2}{\partial t^2} + \beta^2 y^2 \right) \frac{\partial}{\partial z} \left(e^{z/H} \frac{\partial\psi}{\partial z} \right) + N^2 e^{z/H} \frac{\partial^2\psi}{\partial y^2} = \frac{g}{c_p T_0} \frac{\partial Q}{\partial y}, \quad (2.10)$$

with boundary conditions

$$\psi \rightarrow 0 \text{ as } y \rightarrow \pm\infty, \quad (2.11)$$

$$\psi = 0 \text{ at } z = z_T, \quad (2.12)$$

$$\left(\frac{\partial^2}{\partial t^2} + \beta^2 y^2 \right) \frac{\partial\psi}{\partial z} + g \frac{\partial^2\psi}{\partial y^2} = g \frac{\partial\mathcal{W}}{\partial y} \text{ at } z = 0, \quad (2.13)$$

and with the initial conditions

$$\psi = 0 \quad \text{and} \quad \frac{\partial \psi}{\partial t} = 0 \quad \text{at} \quad t = 0. \quad (2.14)$$

Note that the diabatic forcing appears through the right hand side of the interior equation (2.10), while the Ekman pumping appears through the right hand side of the lower boundary condition (2.13). Also, note that N^2 is a measure of the static stability and $\beta^2 y^2$ is a measure of the inertial stability, which both act as shaping parameters. Baroclinicity is also a shaping parameter, but it does not appear because of the simplifications introduced in (2.1)–(2.5). The meridional circulation problem (2.10)–(2.14) can be written in a slightly simpler form by defining $\hat{\psi}(y, z, t)$ and $\hat{Q}(y, z, t)$ as

$$\begin{aligned} \hat{\psi}(y, z, t) &= \psi(y, z, t) e^{z/2H}, \\ \hat{Q}(y, z, t) &= Q(y, z, t) e^{-z/2H}. \end{aligned} \quad (2.15)$$

Using (2.15) in (2.10)–(2.14) the meridional circulation problem is written in the form

$$\left(\frac{\partial^2}{\partial t^2} + \beta^2 y^2 \right) \left(\frac{\partial^2 \hat{\psi}}{\partial z^2} + N^2 \frac{\partial^2 \hat{\psi}}{\partial y^2} - \frac{\hat{\psi}}{4H^2} \right) = \frac{g}{c_p T_0} \frac{\partial \hat{Q}}{\partial y}, \quad (2.16)$$

with boundary conditions

$$\hat{\psi} \rightarrow 0 \quad \text{as} \quad y \rightarrow \pm\infty, \quad (2.17)$$

$$\hat{\psi} = 0 \quad \text{at} \quad z = z_T, \quad (2.18)$$

$$\left(\frac{\partial^2}{\partial t^2} + \beta^2 y^2 \right) \left(\frac{\partial \hat{\psi}}{\partial z} + g \frac{\partial^2 \hat{\psi}}{\partial y^2} - \frac{\hat{\psi}}{2H} \right) = g \frac{\partial \mathcal{W}}{\partial y} \quad \text{at} \quad z = 0, \quad (2.19)$$

and with the initial conditions

$$\hat{\psi} = 0 \quad \text{and} \quad \frac{\partial \hat{\psi}}{\partial t} = 0 \quad \text{at} \quad t = 0. \quad (2.20)$$

Note that (2.16) has a convenient form because of the absence of the $e^{z/H}$ factors. We shall solve (2.16)–(2.20) analytically using transform methods. The first step involves a vertical transform that converts our (y, z, t) partial differential equations to partial differential equations in (y, t) . Horizontal transforms are used after the vertical transform, converting our partial differential equations in (y, t) to a system of ordinary differential equations in time. Then we are able to compute the analytical solution of the original meridional circulation problem.

2.4. VERTICAL TRANSFORM

Solutions of (2.16)–(2.20) are computed via the vertical transform pair

$$\hat{\psi}(y, z, t) = \sum_{m=0}^{\infty} \hat{\psi}_m(y, t) \mathcal{Z}_m(z), \quad (2.21)$$

$$\hat{\psi}_m(y, t) = \frac{1}{g} \int_0^{z_T} \hat{\psi}(y, z, t) \mathcal{Z}_m(z) N^2(z) dz + \hat{\psi}(y, 0, t) \mathcal{Z}_m(0). \quad (2.22)$$

In other words, the streamfunction $\hat{\psi}(y, z, t)$ is represented in terms of a series of vertical structure functions $\mathcal{Z}_m(z)$, with the coefficients $\hat{\psi}_m(y, t)$ given by (2.22), where m refers to the vertical modes. The reason for the last term in (2.22) arises from the lower boundary condition (2.19), as will become apparent shortly. The vertical structure functions $\mathcal{Z}_m(z)$ are solutions of the Sturm-Liouville eigenvalue problem

$$\frac{d^2 \mathcal{Z}_m}{dz^2} - \frac{\mathcal{Z}_m}{4H^2} = -\frac{N^2 \mathcal{Z}_m}{gh_m}, \quad (2.23)$$

$$\mathcal{Z}_m = 0 \quad \text{at} \quad z = z_T, \quad (2.24)$$

$$\frac{d\mathcal{Z}_m}{dz} - \frac{\mathcal{Z}_m}{2H} = -\frac{\mathcal{Z}_m}{h_m} \text{ at } z = 0, \quad (2.25)$$

with eigenvalues (or equivalent depths) denoted by h_m . These equivalent depths correspond to the solution of the Sturm-Liouville eigenvalue problem (2.23)–(2.25), where the eigenfunctions are denoted by $\mathcal{Z}_m(z)$. For $N^2(z) > 0$, the solutions of the Sturm-Liouville problem have the following three properties (Fulton and Schubert 1985): (i) The eigenvalues h_m are real and may be ordered such that $h_0 > h_1 > \dots > h_m > 0$ with $h_m \rightarrow 0$ as $m \rightarrow \infty$; (ii) The eigenfunctions $\mathcal{Z}_m(z)$ are orthogonal and may be chosen to be real; (iii) The eigenfunctions $\mathcal{Z}_m(z)$ form a complete set. A discussion of the transform pair (2.21)–(2.22) is given in Appendix A, along with a proof of properties (i) and (ii). The derivation of the solutions to the eigenvalue problem (2.23)–(2.25) for the special case of constant N as well as a proof of property (iii) are given in Appendix B. The first five vertical structure functions $\mathcal{Z}_m(z)$ for the special case of constant N are plotted in Fig. 2.2.

To take the vertical transform of (2.16), we multiply it by $\mathcal{Z}_m(z)$ and integrate in z from 0 to z_T to yield

$$\begin{aligned} & \frac{\partial^2}{\partial y^2} \int_0^{z_T} \hat{\psi}(y, z, t) \mathcal{Z}_m(z) N^2(z) dz \\ & + \left(\frac{\partial^2}{\partial t^2} + \beta^2 y^2 \right) \left[\mathcal{Z}_m(z) \frac{\partial \hat{\psi}(y, z, t)}{\partial z} - \hat{\psi}(y, z, t) \frac{d\mathcal{Z}_m(z)}{dz} \right]_0^{z_T} \\ & + \left(\frac{\partial^2}{\partial t^2} + \beta^2 y^2 \right) \int_0^{z_T} \hat{\psi}(y, z, t) \left(\frac{d^2 \mathcal{Z}_m(z)}{dz^2} - \frac{\mathcal{Z}_m(z)}{4H^2} \right) dz \\ & = \frac{g}{c_p T_0} \frac{\partial}{\partial y} \int_0^{z_T} \hat{Q}(y, z, t) \mathcal{Z}_m(z) dz. \end{aligned} \quad (2.26)$$

Note that the integral originating from $(\partial \hat{\psi} / \partial z^2)$ in (2.16) is integrated by parts twice. In order to simplify (2.26), we use (2.23) in the third line and then use (2.18) and (2.24) to show that the upper boundary term in the second line vanishes. To evaluate the lower boundary term in the second line,

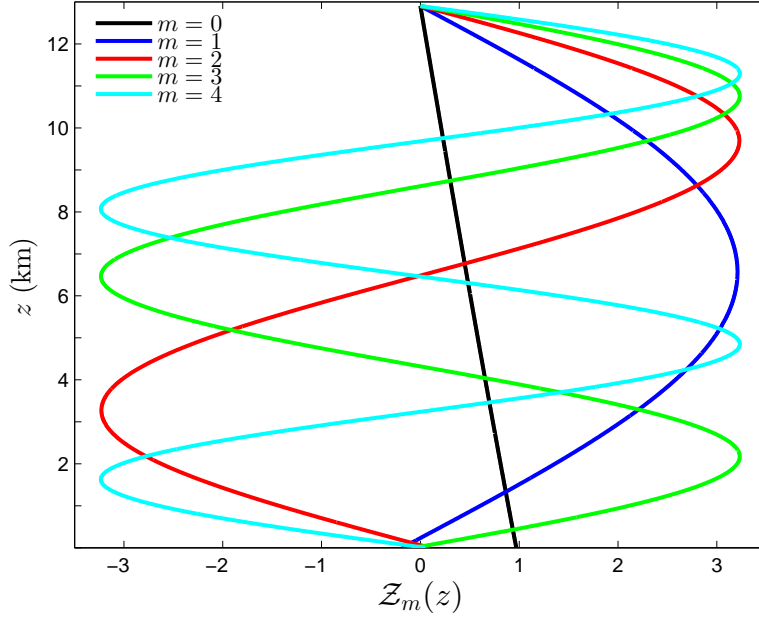


FIG. 2.2. Vertical structure functions $\mathcal{Z}_m(z)$ for the external mode $m = 0$ and the first four internal modes $m = 1, 2, 3, 4$. As discussed in Appendix B, these vertical structure functions are solutions of the Sturm-Liouville problem (2.23)–(2.25) with the constant buoyancy frequency $N = 1.2 \times 10^{-2} \text{ s}^{-1}$ and $z_T = 13 \text{ km}$.

we eliminate $\partial\hat{\psi}/\partial z$ by using (2.19) and then group the resulting $(\partial^2\hat{\psi}/\partial y^2)$ term with the first line of (2.26). Similarly, we use (2.25) to eliminate $d\mathcal{Z}_m/dz$ and then group the resulting \mathcal{Z}_m/h_m term with the third line of (2.26). This procedure simplifies (2.26) to

$$\begin{aligned}
& \frac{\partial^2}{\partial y^2} \left[\frac{1}{g} \int_0^{z_T} \hat{\psi}(y, z, t) \mathcal{Z}_m(z) N^2(z) dz + \hat{\psi}(y, 0, t) \mathcal{Z}_m(0) \right] \\
& - \frac{\beta^2 y^2}{gh_m} \left[\frac{1}{g} \int_0^{z_T} \hat{\psi}(y, z, t) \mathcal{Z}_m(z) N^2(z) dz + \hat{\psi}(y, 0, t) \mathcal{Z}_m(0) \right] \\
& = \frac{\partial}{\partial y} \left[\int_0^{z_T} \frac{\hat{Q}(y, z, t)}{c_p T_0} \mathcal{Z}_m(z) dz + \mathcal{W}(y, t) \mathcal{Z}_m(0) \right].
\end{aligned} \tag{2.27}$$

Making use of (2.22), this procedure then simplifies (2.27) to

$$\frac{\partial^2 \hat{\psi}_m}{\partial t^2} - gh_m \left(\frac{\partial^2}{\partial y^2} - \frac{y^2}{b_m^4} \right) \hat{\psi}_m = -gh_m \frac{\partial F_m}{\partial y}, \tag{2.28}$$

with boundary conditions

$$\hat{\psi}_m(y, t) \rightarrow 0 \text{ as } y \rightarrow \pm\infty, \quad (2.29)$$

and with the initial conditions

$$\hat{\psi}_m = 0 \quad \text{and} \quad \frac{\partial \hat{\psi}_m}{\partial t} = 0 \quad \text{at } t = 0, \quad (2.30)$$

where the forcing term $F_m(y, t)$ on the right hand side of (2.28) is given by

$$F_m(y, t) = \int_0^{z_T} \frac{\hat{Q}(y, z, t)}{c_p T_0} \mathcal{Z}_m(z) dz + \mathcal{W}(y, t) \mathcal{Z}_m(0), \quad (2.31)$$

and where the equatorial Rossby length b_m is given by

$$b_m = \left(\frac{gh_m}{4\beta^2} \right)^{1/4} = \epsilon_m^{-1/4} \frac{a}{\sqrt{2}}. \quad (2.32)$$

Lamb's parameter is defined by $\epsilon_m = 4\Omega^2 a^2 / (gh_m)$. The spectra of equivalent depths h_m , equatorial Rossby lengths b_m , and Lamb's parameters ϵ_m for $m = 0, 1, 2, \dots, 10$ are shown in Table 2.1. Note that the interior diabatic heating $\hat{Q}(y, z, t)$ and the boundary layer pumping $\mathcal{W}(y, t)$, which were separate forcing effects in (2.16) and (2.19), have now merged into the single forcing term $F_m(y, t)$.

2.5. SOLUTION OF THE HORIZONTAL STRUCTURE EQUATION VIA THE GREEN'S FUNCTION

In order to solve (2.28)–(2.30), we first assume that if the diabatic forcing $Q(y, z, t)$ and the boundary layer forcing $\mathcal{W}(y, t)$ vary slowly in time, the $\partial^2/\partial t^2$ terms in the interior equation (2.28) and the boundary condition (2.30) can be neglected. By neglecting these second time derivatives, $\psi(y, z, t)$ has no memory of the past forcing and is diagnostically determined by the current forcing

TABLE 2.1. The spectra of equivalent depths h_m , gravity wave speeds $(gh_m)^{1/2}$ (with approximate values in parentheses), equatorial Rossby lengths $b_m = [gh_m/(4\beta^2)]^{1/4}$, and Lamb's parameters $\epsilon_m = 4\Omega^2 a^2/(gh_m)$ for the eleven values of m listed in the left column. The values have been computed from (B4) and (B10) using $z_T = 13$ km, $g = 9.8$ m s $^{-2}$, $a = 6371$ km, $\Omega = 7.292 \times 10^{-5}$ s $^{-1}$, $N = 1.2 \times 10^{-2}$ s $^{-1}$, and $H = 8581$ m.

m	h_m (m)	$(gh_m)^{1/2}$ (m s $^{-1}$)	b_m (km)	ϵ_m
0	7099	263.8 (—)	2400	12.41
1	229.8	47.46 (48.27)	1018	383.4
2	61.42	24.53 (24.65)	732.0	1434
3	27.66	16.46 (16.50)	599.7	3185
4	15.63	12.38 (12.39)	519.9	5636
5	10.03	9.912 (9.920)	465.3	8787
6	6.970	8.265 (8.270)	424.9	12638
7	5.125	7.087 (7.090)	393.4	17190
8	3.925	6.202 (6.204)	368.1	22442
9	3.103	5.514 (5.515)	347.0	28394
10	2.514	4.963 (4.964)	329.3	35046

only. For the rest of this chapter, we will make use of this assumption. The Green's function $G_m(y, y')$ is introduced, which is the solution of the ordinary differential equation

$$\frac{d^2 G_m}{dy^2} - \frac{y^2}{4b_m^4} G_m = -\frac{1}{b_m^2} \delta\left(\frac{y - y'}{b_m}\right), \quad (2.33)$$

with the boundary conditions

$$G_m(y, y') \rightarrow 0 \text{ as } y \rightarrow \pm\infty, \quad (2.34)$$

where the Dirac delta function vanishes for $y \neq y'$ and satisfies

$$\frac{1}{b_m} \int_{y'_-}^{y'_+} \delta\left(\frac{y - y'}{b_m}\right) dy = 1. \quad (2.35)$$

The Green's function $G_m(y, y')$ is useful in understanding the meridional structure of the Hadley circulation since the left hand side of (2.33) is equivalent to that of (2.28). As will be seen, all of the meridional asymmetry of the Hadley circulation is built into the Green's function.

The Green's function $G_m(y, y')$ is constructed from the parabolic cylinder functions $D_\nu(x)$, which satisfy

$$\frac{d^2 D_\nu}{dx^2} + \left(\nu + \frac{1}{2} - \frac{1}{4}x^2 \right) D_\nu = 0. \quad (2.36)$$

Note that the order $\nu = -1/2$ parabolic cylinder functions $D_{-1/2}(y/b_m)$ and $D_{-1/2}(-y/b_m)$ are solutions of the homogeneous version of (2.33). The functions $D_{-1/2}(x)$ and $D_{-1/2}(-x)$ are plotted in Fig. 2.3.

Only the solution $G_m(y, y') = \alpha_1 D_{-1/2}(-y/b_m)$ is valid for $-\infty \leq y \leq y'$, and only the solution $G_m(y, y') = \alpha_2 D_{-1/2}(y/b_m)$ is valid for $y' \leq y < \infty$ because of the lateral boundary conditions (2.34). Note that α_1 and α_2 depend on y' , and are determined by requiring that $G_m(y, y')$ is continuous at $y = y'$ and that the jump in the first derivative satisfies

$$b_m \left[\frac{dG_m}{dy} \right]_{y'-}^{y'+} = -1, \quad (2.37)$$

which is obtained by integrating (2.33) across a narrow region surrounding $y = y'$, making use of the delta function property (2.35), and noting that the narrow integral of the first term left of the equals sign in (2.33) is zero. The two algebraic equations for α_1 and α_2 can be solved with the aid of the Wronskian

$$D_{-1/2}(x) \frac{dD_{-1/2}(-x)}{dx} - D_{-1/2}(-x) \frac{dD_{-1/2}(x)}{dx} = \sqrt{2}. \quad (2.38)$$

The Wronskian is derived by multiplying (2.36) by $D_\nu(-x)$ and multiplying the version of (2.36) where $x \rightarrow -x$ by $D_\nu(x)$, and combining the two resulting equations. Solving for α_1 and α_2 using

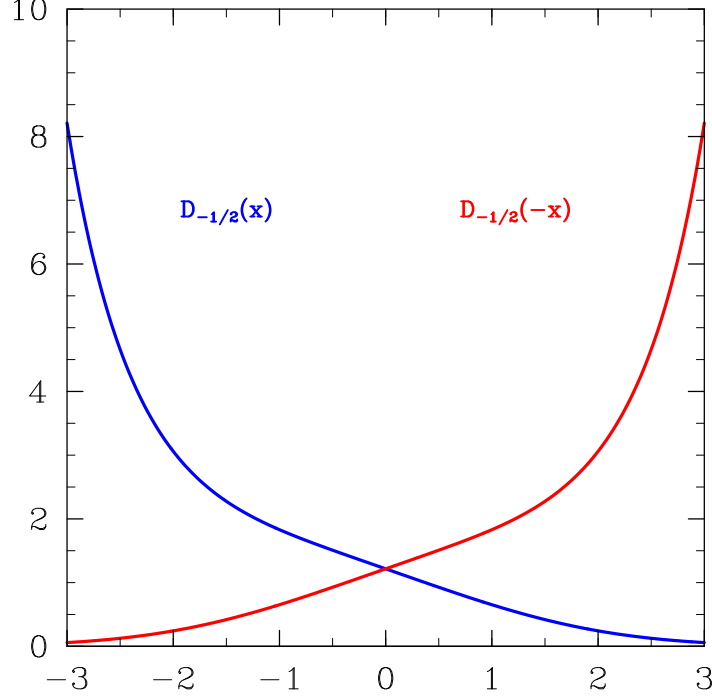


FIG. 2.3. Parabolic cylinder functions $D_{-1/2}(x)$ and $D_{-1/2}(-x)$ for $-3 \leq x \leq 3$. The function $D_{-1/2}(x)$, shown by the blue curve, satisfies the $y \rightarrow \infty$ boundary condition and is used to construct the Green's function $G_m(y, y')$ north of y' . Similarly, the function $D_{-1/2}(-x)$, shown by the red curve, satisfies the $y \rightarrow -\infty$ boundary condition and is used to construct the Green's function $G_m(y, y')$ south of y' . Because these two parabolic cylinder functions are solutions of (2.36) with $\nu = -1/2$, their second derivatives are zero at the equator but become large away from the equator. All the calculations presented here use the Mathematica function `ParabolicCylinderD`[ν, x].

(2.38) results in

$$G_m(y, y') = \frac{1}{\sqrt{2}} \begin{cases} D_{-1/2}(y'/b_m)D_{-1/2}(-y/b_m) & \text{if } -\infty < y \leq y' \\ D_{-1/2}(-y'/b_m)D_{-1/2}(y/b_m) & \text{if } y' \leq y < \infty. \end{cases} \quad (2.39)$$

Plots of $G_m(y, y')$ for $y' = -1500, -750, 0, 750, 1500$ km and $m = 0, 1, 2$ are shown in Fig. 2.4.

Note that, as m increases, the jump in the derivative of $G_m(y, y')$ at $y = y'$ in (2.37) increases since b_m decreases. Therefore, the Green's function becomes more confined to the region near $y = y'$ and we expect the response of the Hadley circulation to become more confined in the meridional

direction. Also, note the meridional asymmetry of the Green's function between either side of y' when y' is placed away from the equator. Therefore, we expect the Hadley cells to reflect this asymmetry when the ITCZ is placed off of the equator.

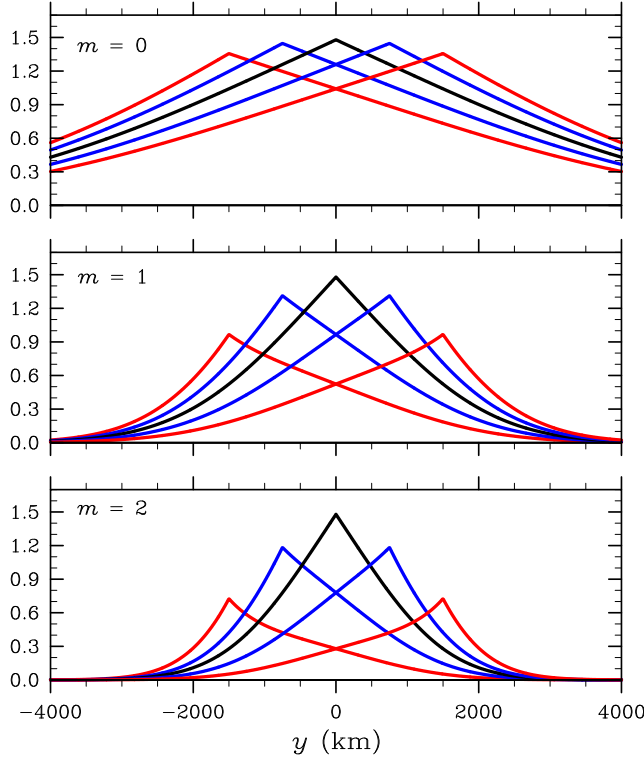


FIG. 2.4. Green's functions $G_m(y, y')$ for $y' = -1500, -750, 0, 750, 1500$ km and for $m = 0$ (top panel), $m = 1$ (middle panel), and $m = 2$ (bottom panel). These curves have been computed from (2.39). Note that, because of the b_m factors in (2.39), the Green's functions become more confined as the vertical mode index m becomes larger.

To express the solution $\hat{\psi}_m(y, t)$ in terms of the Green's function, we multiply (2.28) by $G_m(y, y')$, multiply (2.33) by $\hat{\psi}_m(y, t)$, and then take the difference of the resulting equations to obtain

$$\begin{aligned} & \frac{\partial}{\partial y} \left(G_m(y, y') \frac{\partial \hat{\psi}_m(y, t)}{\partial y} - \hat{\psi}_m(y, t) \frac{dG_m(y, y')}{dy} \right) \\ &= \frac{\partial F_m(y, t)}{\partial y} G_m(y, y') + \hat{\psi}_m(y, t) \frac{1}{b_m} \delta \left(\frac{y - y'}{b_m} \right). \end{aligned} \quad (2.40)$$

We now integrate (2.40) over y , apply the boundary conditions (2.29) and (2.34), use the delta function property (2.35) and the Green's function symmetry property $G_m(y', y) = G_m(y, y')$, resulting in (2.42). In summary, the solution of the meridional circulation problem is

$$\psi(y, z, t) = e^{-z/2H} \sum_{m=0}^{\infty} \hat{\psi}_m(y, t) \mathcal{Z}_m(z), \quad (2.41)$$

where

$$\hat{\psi}_m(y, t) = -b_m \int_{-\infty}^{\infty} \frac{\partial F_m(y', t)}{\partial y'} G_m(y, y') dy'. \quad (2.42)$$

The solution for the streamfunction is obtained by first calculating $F_m(y', t)$ from (2.31), then calculating $\hat{\psi}_m(y, t)$ from (2.42), and finally calculating $\psi(y, z, t)$ from (2.41). Although this procedure generally involves the calculation of two integrals and an infinite sum, there are two special cases where the formulas (2.41)–(2.42) are considerably simplified. One corresponds to prescribed diabatic heating in the ITCZ, and the other corresponds to prescribed Ekman pumping at the top of the boundary layer. Making these prescribed fields step functions in y allows for analytical solutions. These idealized ITCZ forcings are introduced in the next two sections.

2.6. DEEP OVERTURNING CIRCULATIONS

Now consider the response to a constant forcing that projects only onto the first internal mode and is constant in time. We begin by using (2.30), along with the assumption of constant N , to write

$$F_m(y) = \frac{g\hat{Q}_m(y)}{c_p T_0 N^2} + \left(\mathcal{W}(y) - \frac{g\hat{Q}(y, 0)}{c_p T_0 N^2} \right) \mathcal{Z}_m(0), \quad (2.43)$$

where

$$\hat{Q}_m(y) = \frac{N^2}{g} \int_0^{z_T} \hat{Q}(y, z) \mathcal{Z}_m(z) dz + \hat{Q}(y, 0) \mathcal{Z}_m(0). \quad (2.44)$$

We assume that $\hat{Q}(y, z)$ vanishes everywhere except in the latitudinal range $y_1 < y < y_2$, where y_1 and y_2 are constants that specify the south and north boundaries of the ITCZ. Within the ITCZ, the diabatic heating is assumed to be independent of y and to have a vertical profile proportional to $\mathcal{Z}_1(z)$, i.e.,

$$\hat{Q}(y, z) = \begin{cases} \tilde{Q}\mathcal{Z}_1(z) & \text{if } y_1 < y < y_2, \\ 0 & \text{otherwise,} \end{cases} \quad (2.45)$$

where \tilde{Q} will be given later. In addition, we assume that the vertical velocity at the top of the boundary layer is given by

$$\mathcal{W}(y) = \frac{g\hat{Q}(y, 0)}{c_p T_0 N^2}. \quad (2.46)$$

Since we would like to use the vertical structure of only the first internal mode $\mathcal{Z}_1(z)$ as the vertical structure of the prescribed diabatic heating and the vertical structure of the first internal mode is nonzero at the top of the boundary layer (Fig. 2), there has to be a nonzero \mathcal{W} at $z = 0$.

Using these assumptions in (2.43) and (2.44), and then making use of the orthonormality relation (A.2) we obtain

$$F_m(y) = \frac{g\tilde{Q}}{c_p T_0 N^2} \begin{cases} 1 & \text{if } m = 1 \text{ and } y_1 < y < y_2, \\ 0 & \text{otherwise.} \end{cases} \quad (2.47)$$

Many tropical regions have more complicated vertical diabatic heating profiles, such as the eastern Pacific, where heating profiles are more “bottom heavy” than the $\mathcal{Z}_1(z)$ profile, as illustrated in the studies of Wu et al. (2000), Wang and Magnusdottir (2005), Zhang and Hagos (2009), Takayabu et al. (2010), and Ling and Zhang (2013). Due to this, the assumption that the diabatic heating is deep and made up of only the first internal mode is only meant to represent one aspect

of heating in the tropical atmosphere, and it is the simplest case since it can be represented using only one vertical mode.

Use of (2.47) in (2.42) now yields

$$\begin{aligned}
\hat{\psi}_1(y) &= -b_1 \int_{-\infty}^{\infty} \frac{\partial F_1(y')}{\partial y'} G_1(y, y') dy' \\
&= -b_1 G_1(y, y_1) \int_{y_1^-}^{y_1^+} \frac{\partial F_1(y')}{\partial y'} dy' \\
&\quad - b_1 G_1(y, y_2) \int_{y_2^-}^{y_2^+} \frac{\partial F_1(y')}{\partial y'} dy' \\
&= \frac{gb_1 \tilde{Q}}{c_p T_0 N^2} [G_1(y, y_2) - G_1(y, y_1)],
\end{aligned} \tag{2.48}$$

where the final line in (2.48) follows from the fact that the narrow integral across $y = y_1$ is $[g\tilde{Q}/(c_p T_0 N^2)]$, while the narrow integral across $y = y_2$ is $-[g\tilde{Q}/(c_p T_0 N^2)]$. Use of (2.48) in (2.41), yields the final solution

$$\psi(y, z) = \frac{gb_1 \tilde{Q}}{c_p T_0 N^2} e^{-z/2H} \mathcal{Z}_1(z) [G_1(y, y_2) - G_1(y, y_1)], \tag{2.49}$$

where the Green's functions $G_1(y, y_1)$ and $G_1(y, y_2)$ are given in (2.39). Equation (2.49) is quite powerful. It states that only two Green's functions are needed in order to understand the meridional structure of the deep Hadley circulation. $G_1(y, y_2)$ gives the meridional structure of the streamfunction attributed to the jump in the diabatic heating at the north edge of the ITCZ, while $G_1(y, y_1)$ gives the meridional structure of the streamfunction attributed to the jump in the diabatic heating at the south edge of the ITCZ. All of the information about meridional asymmetries between the winter and summer deep Hadley cells is contained in these two Green's functions. The solution

(2.49) can also be written in the form

$$\psi(y, z) = \frac{gb_1\tilde{Q}}{c_p T_0 N^2 \sqrt{2}} e^{-z/2H} \mathcal{Z}_1(z) \times \begin{cases} [D_{-1/2}(y_2/b_1) - D_{-1/2}(y_1/b_1)]D_{-1/2}(-y/b_1) & \text{if } -\infty < y \leq y_1, \\ D_{-1/2}(y_2/b_1)D_{-1/2}(-y/b_1) - D_{-1/2}(-y_1/b_1)D_{-1/2}(y/b_1) & \text{if } y_1 \leq y \leq y_2, \\ [D_{-1/2}(-y_2/b_1) - D_{-1/2}(-y_1/b_1)]D_{-1/2}(y/b_1) & \text{if } y_2 \leq y < \infty. \end{cases} \quad (2.50)$$

With these assumptions, the $(\partial\hat{Q}/\partial y)$ -term on the right hand side of (2.15) vanishes everywhere except along the edges of the ITCZ, where it becomes infinitely large over an infinitesimally thin layer. Thus, the circulation in the (y, z) -plane consists of a counterclockwise overturning cell on the southern edge of the ITCZ and a clockwise overturning cell in the northern edge of the ITCZ looking from east to west. Figure 2.5 shows these circulation cells via isolines of $\psi(y, z)$ computed from (2.50) using the parameters $z_T = 13$ km, $N = 1.2 \times 10^{-2}$ s $^{-1}$, $(y_1, y_2) = (0, 500), (500, 1000), (1000, 1500), (1500, 2000)$ km, and assuming that $\tilde{Q} = (c_p/B_1) 5$ K day $^{-1}$, where B_1 is derived in Appendix B. The cross-equatorial cell, or winter cell, is significantly stronger than the summer cell, which is limited to the summer hemisphere. As the ITCZ is displaced further away from the equator, the meridional asymmetry between the winter and summer cell increases in Fig. 2.5a)–2.5c), and decreases slightly in Fig. 2.5d). The asymmetry between the two cells is attributed to the meridional asymmetry of the inertial stability parameter, $\beta^2 y^2$. The winter cell is located in a region where $\beta^2 y^2$ is either zero or close to zero, minimizing the turning due to the Coriolis force. When the ITCZ is far enough from the equator, the winter cell is mostly located off of the equator and can no longer efficiently extend into the low inertial stability near the

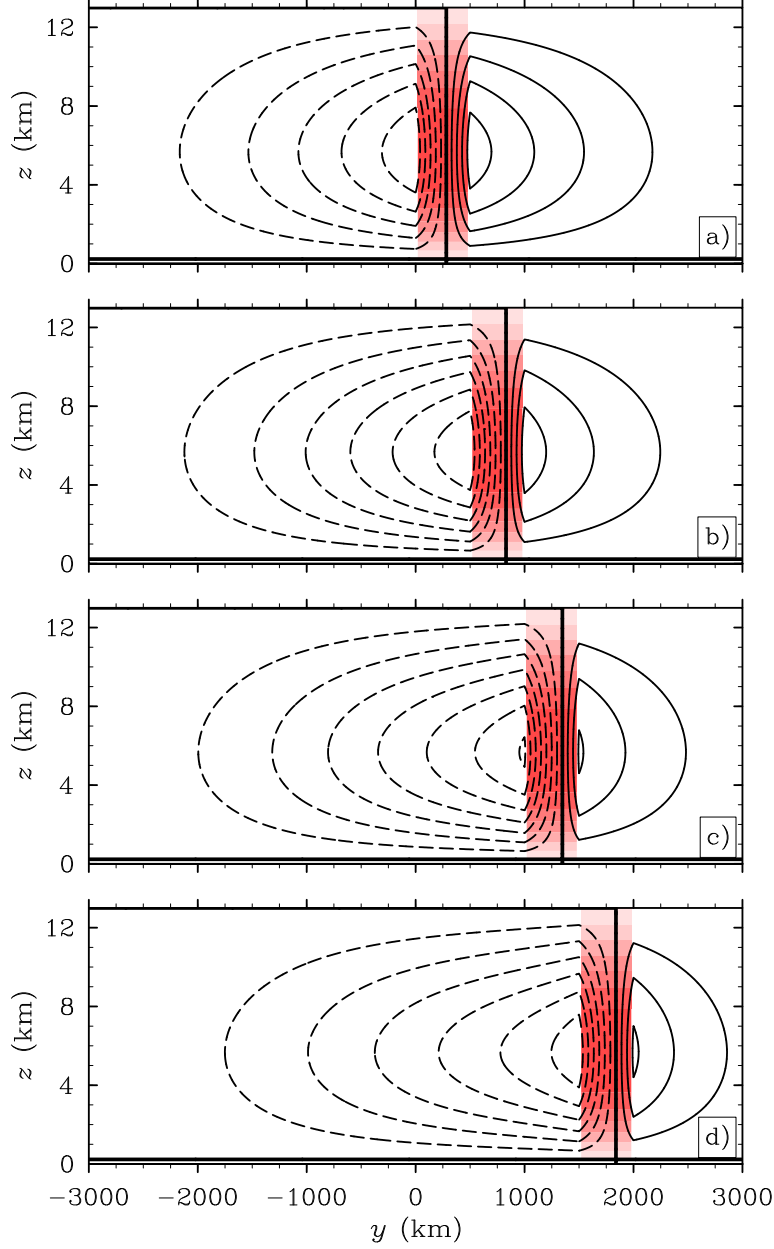


FIG. 2.5. Contoured streamfunction $\psi(y, z)$ and shaded $Q(y, z)e^{-z/H}/c_p$ fields for four deep diabatic heating cases: a) $(y_1, y_2) = (0, 500)$ km, b) $(y_1, y_2) = (500, 1000)$ km, c) $(y_1, y_2) = (1000, 1500)$ km, and d) $(y_1, y_2) = (1500, 2000)$ km. The contour interval for $\psi(y, z)$ is $400 \text{ m}^2 \text{ s}^{-1}$, the maximum (magnitude) of $\psi(y, z)$ is $2852 \text{ m}^2 \text{ s}^{-1}$, and the zero line is of double thickness. The $Q(y, z)e^{-z/H}/c_p$ shade interval is 0.5 K day^{-1} , and the maximum (magnitude) of the diabatic heating is 3.496 K day^{-1} .

equator. Therefore, the mass flux of the winter cell begins to decrease. These results are in general agreement with the numerical model results of Hack et al. (1989).

The meridional asymmetry between the two cells is also apparent in Fig. 2.6, where 0–3 day parcel trajectories are computed from $v(y, z)$ and $w(y, z)$. The parcel trajectories agree well with Schubert et al. (1991). The effects of inertial stability are also apparent in this figure since parcels on the northern edge of the ITCZ travel relatively high in the vertical direction and parcels on the southern edge of the ITCZ travel relatively far in the meridional direction, even though the diabatic heating is constant in the ITCZ. Parcels in the southern part of the ITCZ feel lower inertial stability than parcels on the northern part of the ITCZ.

The approximate time scale it takes a parcel to complete one full cycle in either the winter or summer Hadley cell is two to three months. This time scale is at least an order of magnitude larger than the time it takes for the Hadley cells to equilibrate to the diabatic heating. Note that the zonal velocity is much larger than the meridional velocity, therefore by the time a parcel makes one meridional revolution it will be located at a different longitude, possibly having traveled an entire circle of latitude. Also, calculating such a time scale may be a bit more complicated since combined barotropic and baroclinic instability tends to occur as the zonal winds evolve.

Figure 2.7 shows contours of the $T_t(y, z)$ and $w(y, z)$ fields. It is not surprising that $w(y, z)$ is discontinuous in the meridional direction because the prescribed diabatic heating $\hat{Q}(y, z)$ is discontinuous in the meridional direction. Although, $T_t(y, z)$ is positive and smooth in the meridional direction, even across the edges of the ITCZ. T_t remains positive due to diabatic warming associated with concentrated rising motion in the ITCZ and adiabatic warming associated with broad subsidence outside of the ITCZ. The smooth nature of the temperature tendency field agrees with the idea that temperature gradients are small in the tropics. Also, notice the slight poleward displacement of the peak thermodynamic response in the ITCZ and the asymmetric changes in both

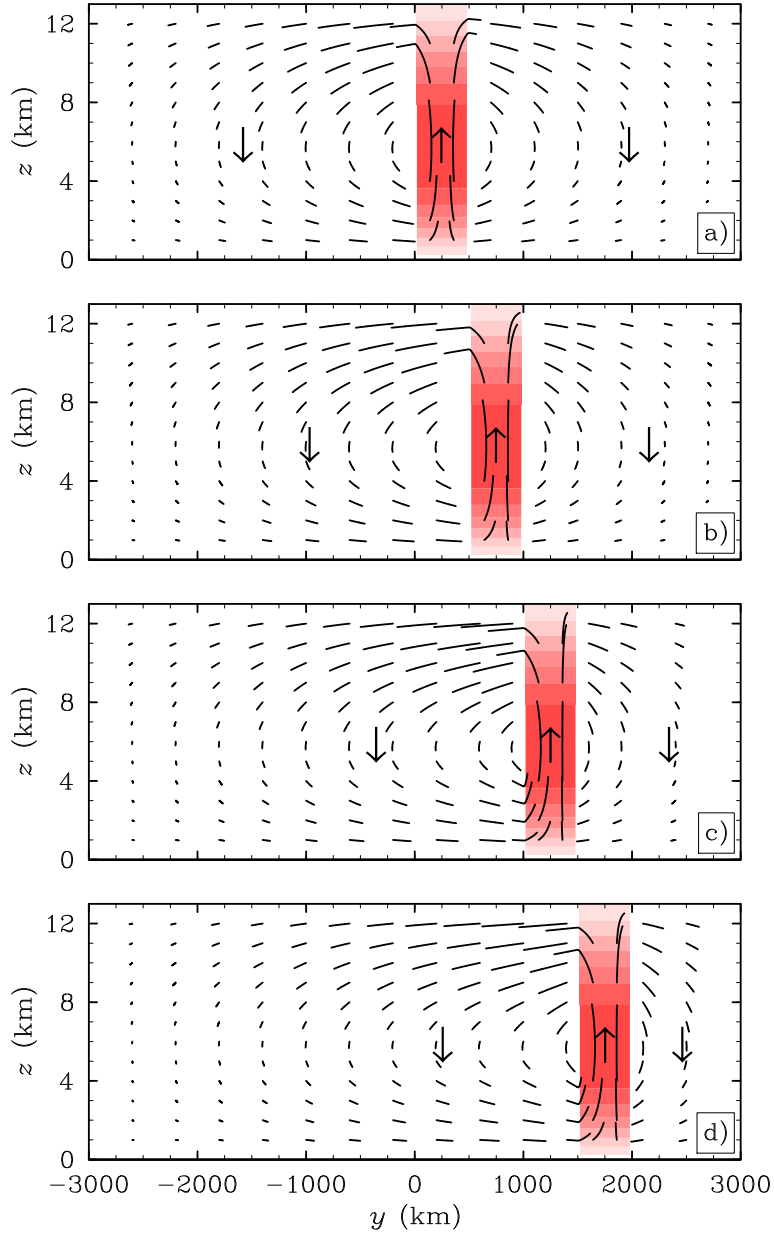


FIG. 2.6. Parcel trajectories and shaded $Q(y, z)e^{-z/H}/c_p$ field (same as Fig. 2.5) during the first three days for the four deep diabatic heating displacements mentioned in Fig. 5. The arrows indicate the direction of the trajectories inside and outside of the ITCZ.

$T_t(y, z)$ and $w(y, z)$ as the ITCZ is moved away from the equator. These results agree well with past studies, such as Hack et al. (1989) and Lindzen and Hou (1988).

Figure 2.8 shows contours of the $v(y, z)$ and $u_t(y, z)$ fields. The $v(y, z)$ field shows low-level convergence and upper-level divergence in and near the ITCZ. Also, the asymmetric response of

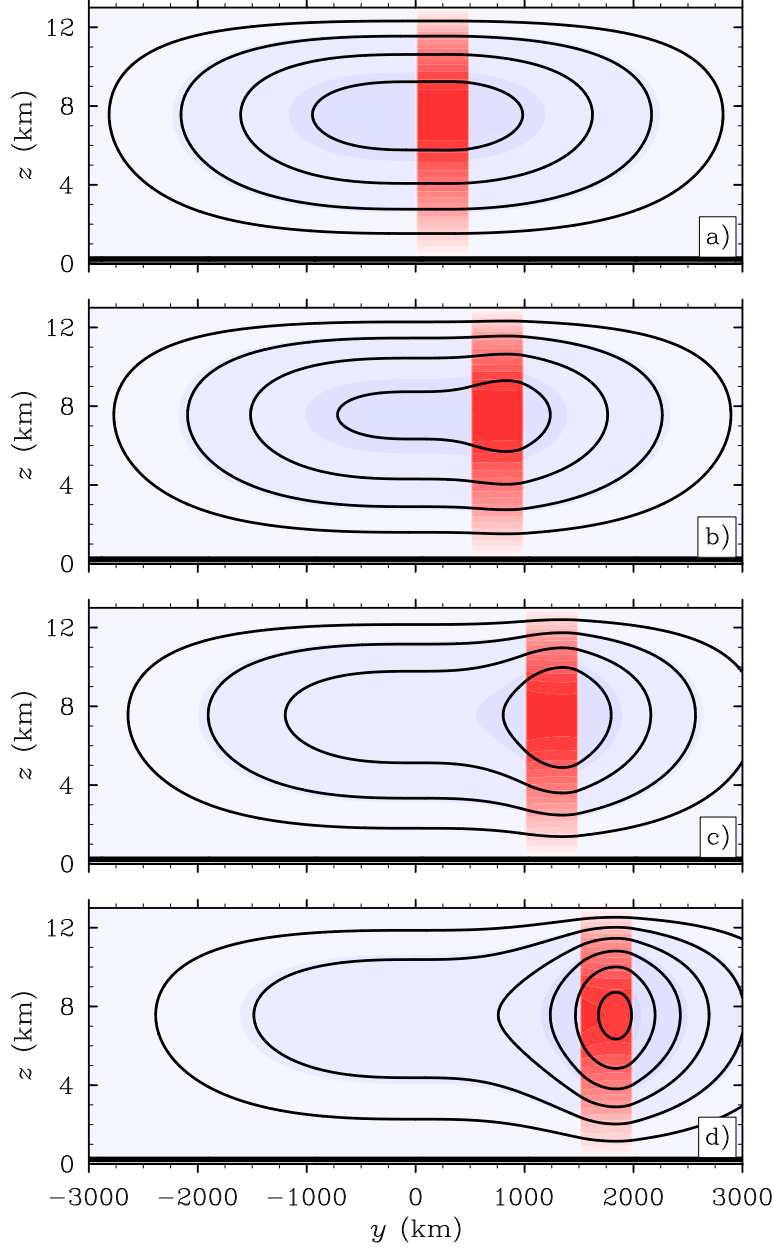


FIG. 2.7. Contoured perturbation temperature tendency $T_t(y, z)$ and shaded log-pressure vertical velocity $w(y, z)$ for the four deep diabatic heating displacements mentioned in Fig. 5. The $T_t(y, z)$ contour interval is 0.2 K day^{-1} , the maximum (magnitude) $T_t(y, z)$ is 1.257 K day^{-1} , and the zero line is of double thickness. The $w(y, z)$ shade interval is 1 mm s^{-1} , and the maximum (magnitude) $w(y, z)$ is 18.01 mm s^{-1} .

$v(y, z)$ increases in Fig. 2.8a)–2.8c) and decreases slightly in Fig. 2.8d), similar to the $\psi(y, z)$ field. The low-level $u_t(y, z)$ field illustrates an increase of westerlies from the equator to slightly poleward of the center of the ITCZ and easterlies poleward of the westerlies. This meridional

structure of the u_t implies a buildup of positive absolute vorticity in the ITCZ that satisfies the necessary condition for combined barotropic and baroclinic instability. At upper levels, the zonal velocity increase at a large rate, especially near the edges of the ITCZ. These upper-level zonal jets can be considered subtropical jets, but are different than jets seen in nature because zonally asymmetric eddies are neglected here.

Another view of combined barotropic and baroclinic instability comes from analyzing the potential vorticity anomaly. The potential vorticity equation is

$$\frac{\partial q}{\partial t} + \beta v = \frac{g\beta y}{c_p T_0 N^2} \left(\frac{\partial}{\partial z} - \frac{1}{H} \right) Q, \quad (2.51)$$

where

$$q = -\frac{\partial u}{\partial y} + \frac{g\beta y}{T_0 N^2} \left(\frac{\partial}{\partial z} - \frac{1}{H} \right) T \quad (2.52)$$

is the potential vorticity anomaly. A reversal of the meridional gradient of the total potential vorticity, $\beta y + q$, occurs on the poleward side of the ITCZ in the lower troposphere and on the equatorward side of the ITCZ in the upper troposphere in Fig. 2.9, agreeing well with Schubert et al. (1991) and Nieto Ferreira and Schubert (1997). Thus, the necessary condition for combined barotropic-baroclinic instability is satisfied (Charney and Stern 1962). As the potential vorticity anomaly increases over time, growth rates of unstable waves are also expected to increase. In this sense, the ITCZ contains the seeds of its own destruction.

2.7. SHALLOW OVERTURNING CIRCULATIONS

While the direct effects of friction are confined to the boundary layer flow in the lowest kilometer, the inviscid interior is indirectly affected through the meridional circulation produced by the upward extension of the Ekman pumping at the top of the boundary layer, as discussed in Holton

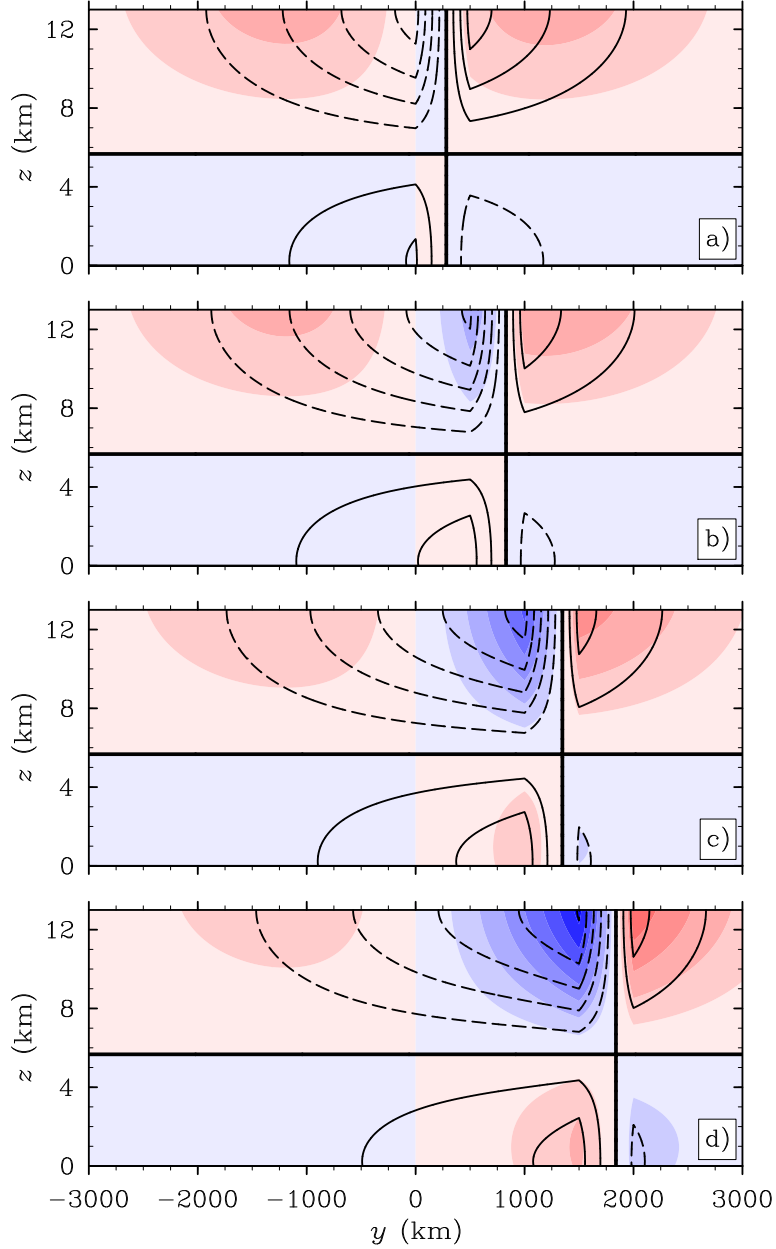


FIG. 2.8. Contoured meridional velocity $v(y, z)$ and shaded zonal velocity tendency $u_t(y, z)$ for the four deep diabatic heating displacements mentioned in Fig. 5. The $v(y, z)$ contour interval is 0.4 m s^{-1} , the maximum (magnitude) $v(y, z)$ is 2.141 m s^{-1} , and the zero line is of double thickness. The $u_t(y, z)$ shade interval is 1 m s^{-1} per day, and the maximum (magnitude) $u_t(y, z)$ is 7.403 m s^{-1} per day.

et al. (1971) and Wang and Rui (1990). An estimate of the Ekman pumping at the top of the boundary layer in the ITCZ can be obtained by considering an idealized equatorial β -plane slab model linearized about a resting basic state of the region between 900 hPa and 1013 hPa, a region which

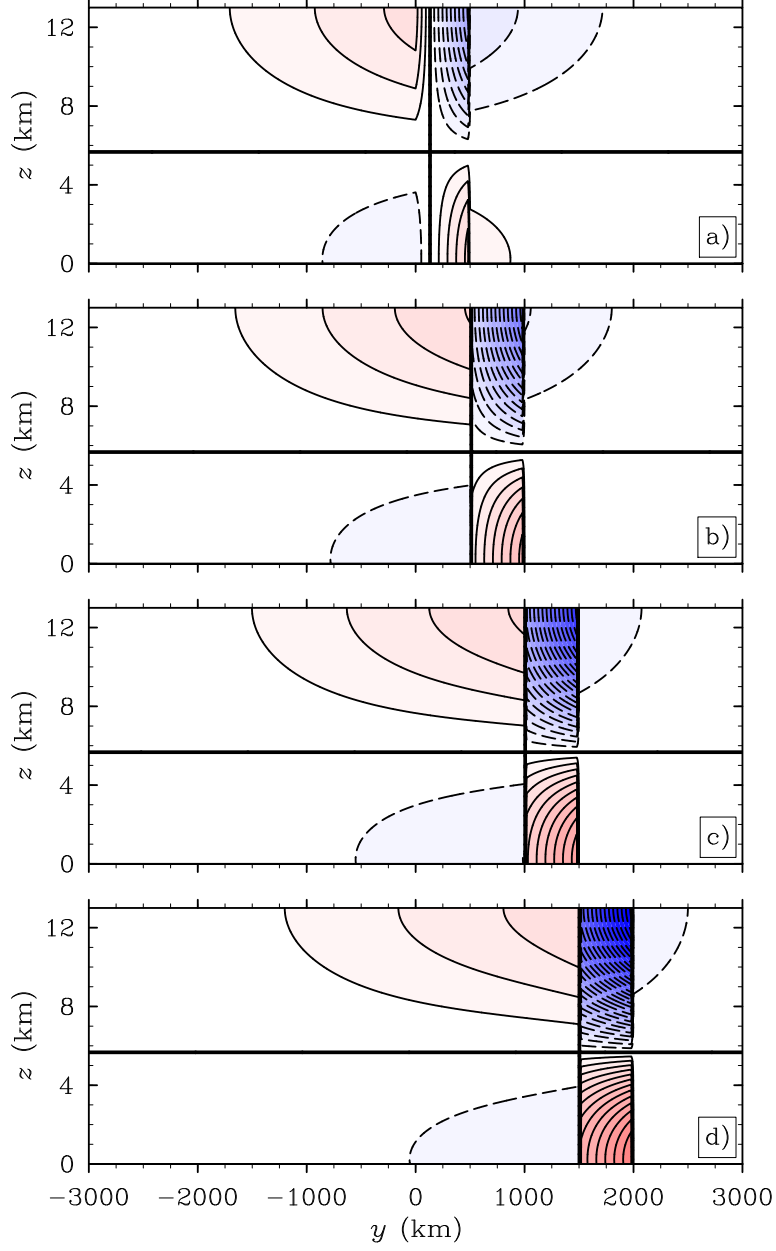


FIG. 2.9. Potential vorticity anomaly tendency $q_t(y, z)$ for the four deep diabatic heating displacements mentioned in Fig. 5. The $q_t(y, z)$ contour interval is 1×10^{-6} s^{-1} per day, the maximum (magnitude) is 2.927×10^{-5} s^{-1} per day, and the zero line is of double thickness.

has the log-pressure depth $h_E = H \ln(1013/900) \approx 1015$ m. In this Ekman layer the dynamics are governed by

$$\frac{\partial u_b}{\partial t} - \beta y v_b = -k u_b, \quad (2.53)$$

$$\frac{\partial v_b}{\partial t} + \beta y u_b = -k v_b + \beta y u_g, \quad (2.54)$$

$$-h_E \frac{\partial v_b}{\partial y} = w(y, 0, t) - w(y, -h_E, t) = \mathcal{W}(y, t), \quad (2.55)$$

where $u_b(y)$ and $v_b(y)$ are the height independent slab boundary layer velocity components, k is the proportionality constant for the surface stress, \mathcal{W} is the Ekman pumping at the top of the boundary layer ($z = 0$), and $u_g(y)$ is the height independent geostrophic zonal velocity, which is defined in terms of the imposed pressure gradient force, $\partial\phi(y)/\partial y$, by

$$\beta y u_g = -\frac{\partial\phi}{\partial y}. \quad (2.56)$$

The first equality in equation (2.55) results from vertical integration of the Boussinesq form of the continuity equation (2.4). The second equality in equation (2.55) is obtained by first noting $w(y, 0, t) = -(1/g)[\partial\phi(y, 0, t)/\partial t] + \mathcal{W}(y, t)$ at the top of the boundary layer and $w(y, -h_E, t) = -(1/g)[T_0/\bar{T}(-h_E)][\partial\phi(y, -h_E)/\partial t]$ at the surface, since the physical height vertical velocity is assumed to vanish at $z = -h_E$. Also, note that $z < 0$ is in the boundary layer and $z = 0$ is the top of the boundary layer. The difference between these last two relations, with the assumption that $T_0/\bar{T}(-h_E) \approx 1$, yields the second equality in equation (2.55), since we assume the geopotential tendency is the same at all heights in the boundary layer.

For slowly evolving flows the time derivative terms in (2.53) and (2.54) can be neglected, and then the resulting two algebraic equations can be solved to obtain

$$u_b(y) = \left(\frac{\beta^2 y^2}{k^2 + \beta^2 y^2} \right) u_g(y), \quad (2.57)$$

$$v_b(y) = \left(\frac{k\beta y}{k^2 + \beta^2 y^2} \right) u_g(y). \quad (2.58)$$

As a typical example, $y_1 = 750$ km, $y_2 = 1250$ km, $u_g(y_1) = 3.0$ m s⁻¹, $u_g(y_2) = -3.0$ m s⁻¹, and $k = 8.3 \times 10^{-6}$ s⁻¹, so that equations (2.57) and (2.58) yield

$$\begin{aligned} u_b(y_2) &= -2.78 \text{ m s}^{-1}, & v_b(y_2) &= -0.78 \text{ m s}^{-1}, \\ u_b(y_1) &= 2.46 \text{ m s}^{-1}, & v_b(y_1) &= 1.15 \text{ m s}^{-1}. \end{aligned} \tag{2.59}$$

Using the values of $v_b(y_1)$ and $v_b(y_2)$ given in equation (2.59) and equation (2.55), we obtain the estimate

$$\mathcal{W}_{\text{ave}} \approx 1015 \text{ m} \left(\frac{1.93 \text{ m s}^{-1}}{500 \text{ km}} \right) \approx 4 \text{ mm s}^{-1} \tag{2.60}$$

for the average Ekman pumping in the ITCZ. Note that it is also possible to calculate a value of vertical velocity at the top of the boundary layer due to other processes. For example, the vertical velocity associated with boundary layer convergence due to SST gradients can be computed in a similar manner as done in Stevens et al. (2002) and Back and Bretherton (2009a).

Based on the above estimate of Ekman pumping, and in order to isolate the effects of the upward penetration of Ekman pumping in (2.28), consider (2.30) for the case in which $\hat{Q}(y, z) = 0$ and

$$\mathcal{W}(y) = \begin{cases} \mathcal{W}_{\text{ave}} & \text{if } y_1 < y < y_2, \\ 0 & \text{otherwise.} \end{cases} \tag{2.61}$$

Use of (2.61) in (2.42) now yields

$$\begin{aligned}
\hat{\psi}_m(y) &= -b_m \mathcal{Z}_m(0) \int_{-\infty}^{\infty} \frac{d\mathcal{W}(y')}{dy'} G_m(y, y') dy' \\
&= -b_m \mathcal{Z}_m(0) G_m(y, y_1) \int_{y_1^-}^{y_1^+} \frac{\partial \mathcal{W}(y')}{\partial y'} dy' \\
&\quad - b_m \mathcal{Z}_m(0) G_m(y, y_2) \int_{y_2^-}^{y_2^+} \frac{\partial \mathcal{W}(y')}{\partial y'} dy' \\
&= b_m \mathcal{Z}_m(0) \mathcal{W}_{\text{ave}} [G_m(y, y_2) - G_m(y, y_1)],
\end{aligned} \tag{2.62}$$

where the final line in (2.62) follows from the fact that the narrow integral across $y = y_1$ is \mathcal{W}_{ave} , while the narrow integral across $y = y_2$ is $-\mathcal{W}_{\text{ave}}$. Use of (2.62) in (2.21), along with (2.14), yields the final solution

$$\psi(y, z) = \mathcal{W}_{\text{ave}} e^{-z/2H} \sum_{m=0}^{\infty} b_m \mathcal{Z}_m(0) \mathcal{Z}_m(z) [G_m(y, y_2) - G_m(y, y_1)]. \tag{2.63}$$

This equation is a bit more complicated than the formula (2.49) for the deep Hadley circulation, but still quite insightful. Equation (2.63) states that a combination of Green's functions, Rossby lengths, and eigenfunctions are needed in order to understand the meridional structure of the shallow Hadley circulation.

The solution (2.63) can also be written in the form

$$\begin{aligned}
\psi(y, z) &= \mathcal{W}_{\text{ave}} e^{-z/2H} \sum_{m=0}^{\infty} b_m \mathcal{Z}_m(0) \mathcal{Z}_m(z) \\
&\times \begin{cases} [D_{-1/2}(y_2/b_m) - D_{-1/2}(y_1/b_m)] D_{-1/2}(-y/b_m) & \text{if } -\infty < y \leq y_1, \\ D_{-1/2}(y_2/b_m) D_{-1/2}(-y/b_m) - D_{-1/2}(-y_1/b_m) D_{-1/2}(y/b_m) & \text{if } y_1 \leq y \leq y_2, \\ [D_{-1/2}(-y_2/b_m) - D_{-1/2}(-y_1/b_m)] D_{-1/2}(y/b_m) & \text{if } y_2 \leq y < \infty. \end{cases}
\end{aligned} \tag{2.64}$$

Using the prescribed Ekman pumping at the top of the boundary layer, the $(\partial\mathcal{W}/\partial y)$ -term on the right hand side of (2.18) vanishes everywhere except along the edges of the ITCZ, analogous to the deep diabatic heating case. Taking the assumed Ekman convergence in the boundary layer into consideration, the circulation in the (y, z) -plane consists of a counterclockwise overturning cell on the southern edge of the ITCZ and a clockwise overturning cell on the northern edge of the ITCZ looking from east to west. Figure 2.10 shows the top half of the circulation cells via isolines of $\psi(y, z)$ computed from (2.59) using the same parameters as for the deep diabatic heating case, $\mathcal{W}_{\text{ave}} = 4 \text{ mm s}^{-1}$, and $(y_1, y_2) = (0, 500), (500, 1000), (1000, 1500), (1500, 2000)$ km. The solutions have been computed using a maximum vertical wavenumber of $m = 500$, and only the region up to $z = 3$ km is displayed since the solution is negligible above $z = 3$ km. The meridional overturning circulation is strongly trapped just above the boundary layer because the resistance of parcels to horizontal motion (i.e., inertial stability) is significantly smaller than their resistance to vertical motion (i.e., static stability). The mass flux of the winter cell is significantly stronger than that of the summer cell, just like the deep Hadley circulation. As the ITCZ is displaced further away from the equator, the meridional asymmetry between the winter and summer cells increases for all of the displacements due once again to the anisotropy of the inertial stability.

In order to see the asymmetric nature of the shallow Hadley circulation in more detail, 0–3 day parcel trajectories calculated from $v(y, z)$ and $w(y, z)$ are illustrated in Fig. 2.11 for the three off-equatorial ITCZ positions: $(y_1, y_2) = (500, 1000), (1000, 1500), (1500, 2000)$ km. For cases in which the ITCZ touches or straddles the equator (not shown), the numerical convergence of the $v(y, z)$ and $w(y, z)$ fields is slow because the shallow return circulation is so strongly trapped just above the top of the boundary layer. The approximate time scale it takes a parcel near the top of

the boundary layer in the ITCZ to cross the equator depends greatly on the displacement of the ITCZ, but is on the order of seven days in a) to two months in c).

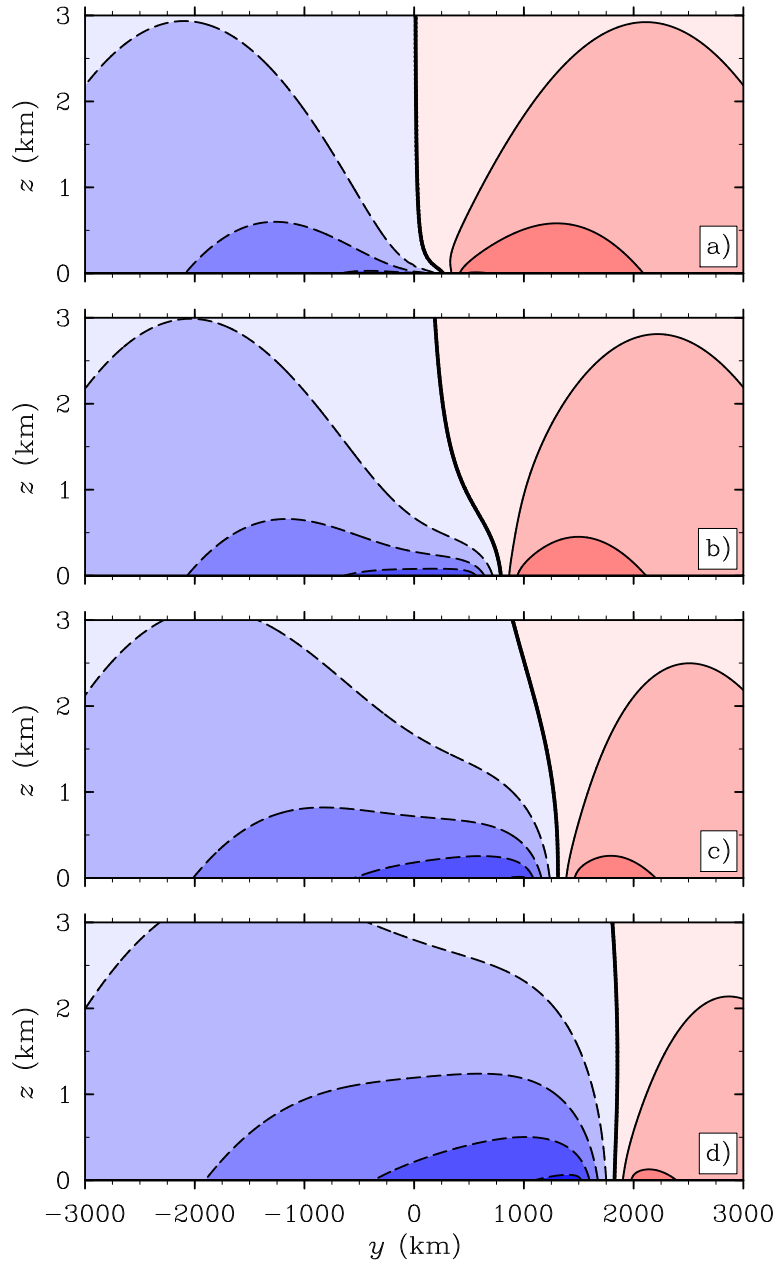


FIG. 2.10. Contoured streamfunction $\psi(y, z)$ for the four displacements mentioned in Fig. 5. The contour interval is $400 \text{ m}^2 \text{ s}^{-1}$, the maximum (magnitude) $\psi(y, z)$ is $1723 \text{ m}^2 \text{ s}^{-1}$, and the zero line is of double thickness. Note: the domain is $0 \leq z \leq 3$, where $z = 0$ is the top of the boundary layer.

Figure 2.12 illustrates contours of $v(y, z)$ for the ITCZ positions: $(y_1, y_2) = (500, 1000)$, $(1000, 1500)$, $(1500, 2000)$ km. There is meridional divergence at the top of the boundary layer

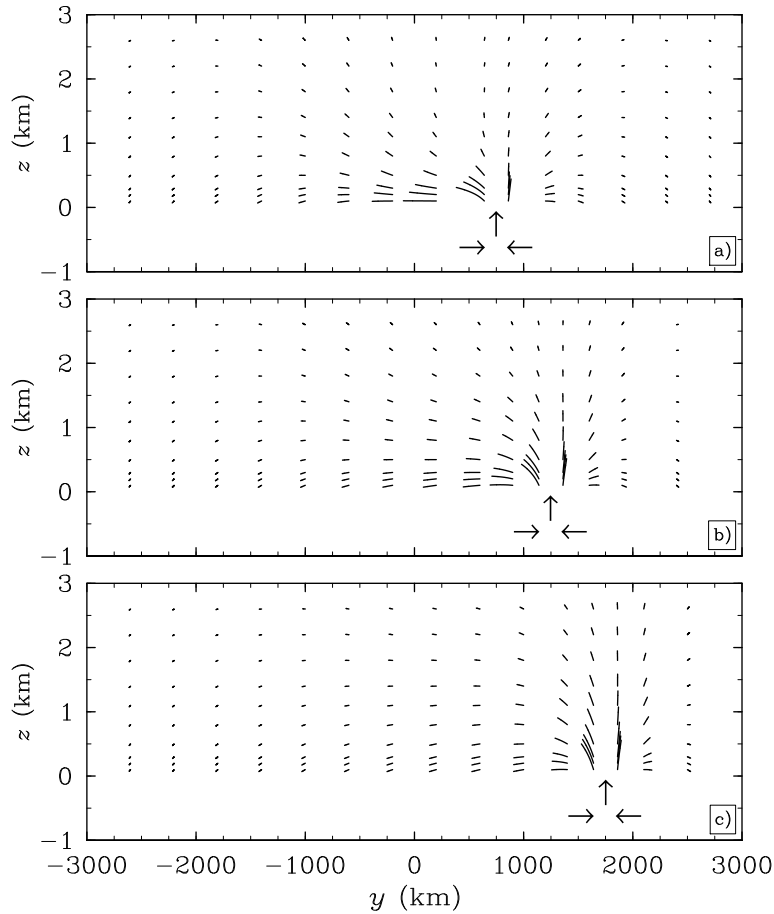


FIG. 2.11. Parcel trajectories during the first three days for three Ekman pumping displacements: a) $(y_1, y_2) = (500, 1000)$ km, b) $(y_1, y_2) = (1000, 1500)$ km, and c) $(y_1, y_2) = (1500, 2000)$ km. Note: the domain is $-1 \leq z \leq 3$, where $z = 0$ is the top of the boundary layer. The arrows indicate the direction of the boundary layer inflow and associated Ekman pumping.

with maximum meridional winds of $3\text{--}7 \text{ m s}^{-1}$, which generally agree with Zhang et al. (2004). Despite these relatively large values of $v(y, z)$, the response of $v(y, z)$ to the Ekman pumping is relatively weak in the southern hemisphere compared to the deep Hadley circulation, except for Fig. 2.12a).

The cross-equatorial meridional winds at the top of the boundary layer may have implications for moisture transport across the equator, as mentioned in both Zhang et al. (2004) and Nolan et al. (2007). As the ITCZ migrates closer to the equator during December–February in the eastern Pacific, the cross-equatorial winds at the top of the boundary layer increase in the winter cell of

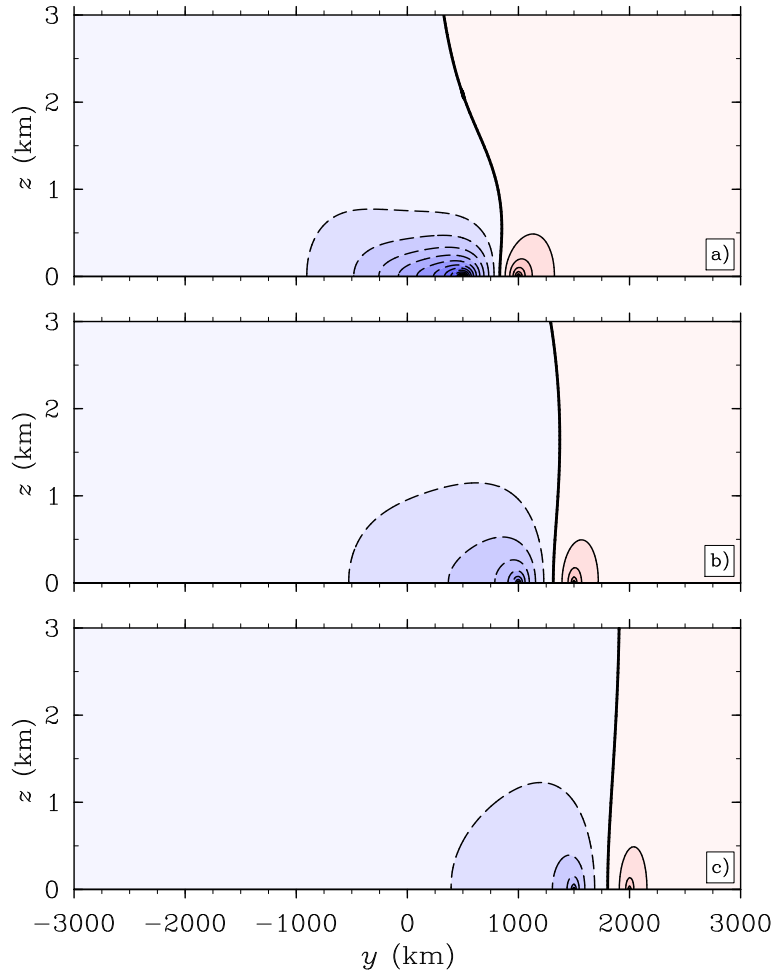


FIG. 2.12. Contoured meridional velocity $v(y, z)$ for the three Ekman pumping displacements mentioned in Fig. 11. The $v(y, z)$ contour interval is 0.4 m s^{-1} , the maximum (magnitude) $v(y, z)$ is 7.922 m s^{-1} , and the zero line is of double thickness. Note: the domain is $0 \leq z \leq 3$, where $z = 0$ is the top of the boundary layer.

the shallow Hadley circulation. These cross-equatorial winds advect moisture across the equator, and along with warmer SSTs south of the equator, may help in setting up favorable conditions for an ITCZ south of the equator. Therefore, a double ITCZ is more likely to be seen during the months after the ITCZ is close but strictly north of the equator. As the ITCZ north of the equator begins to migrate poleward again, the cross-equatorial winds at the top of the boundary layer and SSTs south of the equator decrease, leading to less favorable conditions for an ITCZ south of the equator.

In Fig. 2.13, the vertical log-pressure velocity $w(y, z)$ is contoured for the three ITCZ positions: $(y_1, y_2) = (500, 1000), (1000, 1500), (1500, 2000)$ km. There is rising motion in and near the ITCZ up to $z \approx 2$ km, and weak sinking motion away from the ITCZ. As the ITCZ is displaced farther away from the equator, parcels are pumped to higher levels due to the increase in inertial stability going toward the pole. Also, note that the $T_t(y, z)$ field has the same structure as $w(y, z)$, but with opposite signs (not shown). There is adiabatic cooling where $w(y, z) > 0$ and adiabatic warming where $w(y, z) < 0$, with a maximum perturbation temperature tendency at the top of the ITCZ boundary layer. This result agrees with the theory from Nolan et al. (2007) that shallow overturning circulations are associated with a reversal of the temperature gradient between the ITCZ and away from the ITCZ at the top of the boundary layer.

Observations (Zhang et al. 2004) and numerical modeling studies (Nolan et al. 2007, 2010) tend to show that there are distinct multi-level flows in the ITCZ associated with deep and shallow circulations. Therefore we decided to show the $\psi(y, z)$ solution when both forcings are present (Fig. 2.14). Both the deep and shallow Hadley circulations are present, especially when the ITCZ is close to equator. Taking the assumed boundary layer convergence into consideration, the divergence just above the top of the boundary layer along with convergence until about the middle troposphere and divergence at upper-levels is in general agreement with the studies mentioned above.

2.8. ASYMMETRICAL NATURE OF THE HADLEY CIRCULATION

The meridional asymmetry of the winter and summer cells in both Hadley circulations so far has only been discussed when the ITCZ is 500 km wide. A compact formula can be derived of the fractional asymmetry between the two cells for ITCZs of any width. The maximum mass flux of the winter cell occurs at $y = y_1$ and the maximum mass flux of the summer cell occurs at $y = y_2$

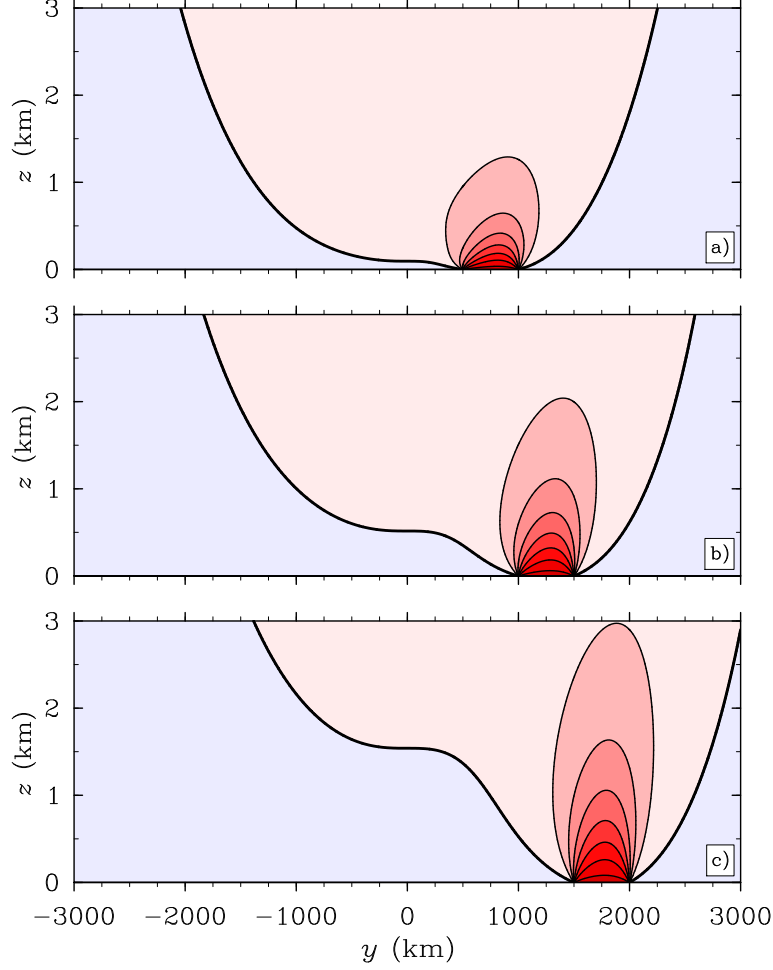


FIG. 2.13. Contoured vertical log-pressure velocity $w(y, z)$ for the three Ekman pumping displacements mentioned in Fig. 11. The $w(y, z)$ contour interval is 0.5 mm s^{-1} , the maximum (magnitude) $w(y, z)$ is 3.774 mm s^{-1} , and the zero line is of double thickness. Note: there is a discontinuity in $\mathcal{W}(z = 0)$ at $y = y_1$ and $y = y_2$, and the domain is $0 \leq z \leq 3$, where $z = 0$ is the top of the boundary layer.

when the ITCZ is north of the equator. Therefore, the fractional mass flux in the summer Hadley cell as a function of vertical wavenumber m is

$$\frac{\hat{\psi}_m(y_2)}{\hat{\psi}_m(y_2) - \hat{\psi}_m(y_1)} = \left\{ 1 - \frac{D_{-1/2}(y_2/b_m)}{D_{-1/2}(-y_1/b_m)} \left[\frac{D_{-1/2}(-y_2/b_m) - D_{-1/2}(-y_1/b_m)}{D_{-1/2}(y_2/b_m) - D_{-1/2}(y_1/b_m)} \right] \right\}^{-1}, \quad (2.65)$$

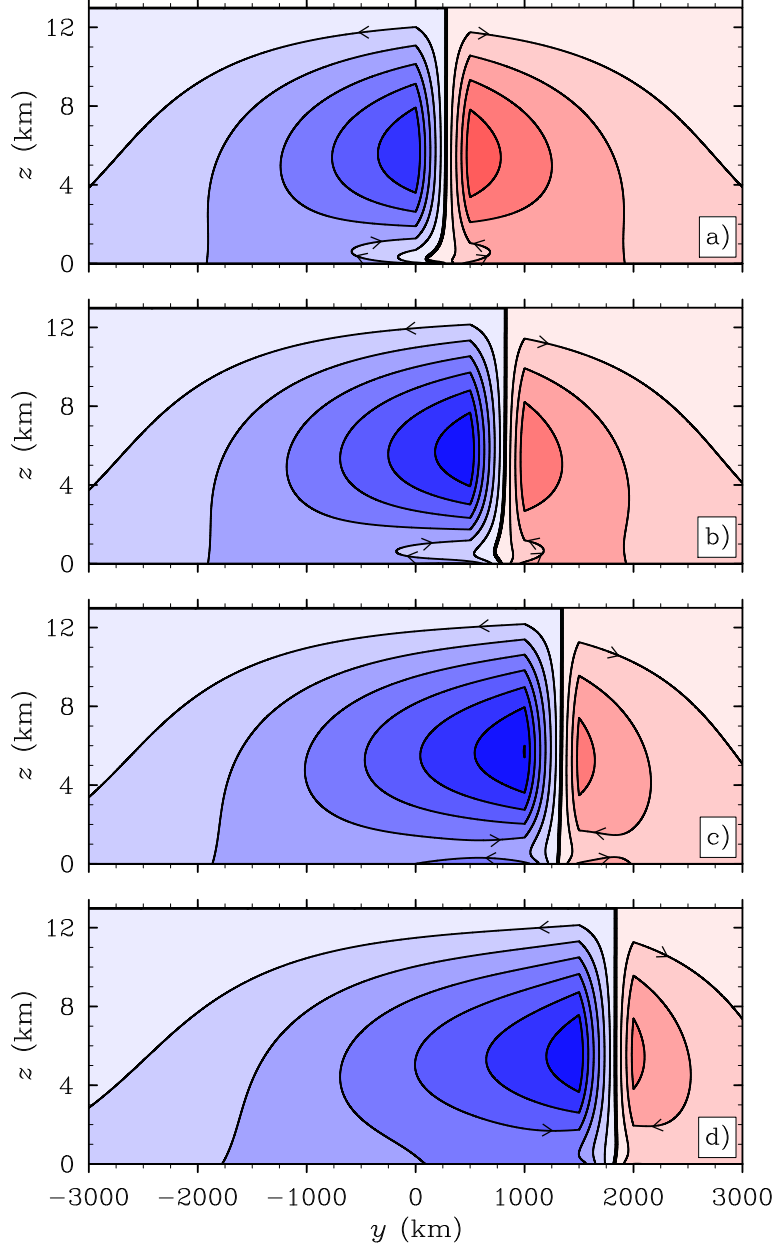


FIG. 2.14. Contoured streamfunction $\psi(y, z)$ of both Ekman pumping and deep diabatic heating for the four displacements mentioned in Fig. 5. The contour interval of $\psi(y, z)$ is $400 \text{ m}^2 \text{ s}^{-1}$, the maximum (magnitude) $\psi(y, z)$ is $2808 \text{ m}^2 \text{ s}^{-1}$, and the zero line is of double thickness. The arrow heads indicate the general direction of the flow field.

and the fractional mass flux in the winter Hadley cell as a function of vertical wavenumber m is

$$\frac{-\hat{\psi}_m(y_1)}{\psi_m(y_2) - \hat{\psi}_m(y_1)} = \left\{ 1 - \frac{D_{-1/2}(-y_1/b_m)}{D_{-1/2}(y_2/b_m)} \left[\frac{D_{-1/2}(y_2/b_m) - D_{-1/2}(y_1/b_m)}{D_{-1/2}(-y_2/b_m) - D_{-1/2}(-y_1/b_m)} \right] \right\}^{-1}. \quad (2.66)$$

Now consider the limiting case where $(y_2 - y_1) \rightarrow 0$, but $\tilde{Q} \rightarrow \infty$ in such a way that $\tilde{Q}(y_2 - y_1) = \text{constant}$. Equation (2.50) reduces to

$$\psi(y, z) = \frac{g\tilde{Q}(y_2 - y_1)}{c_p T_0 N^2 \sqrt{2}} e^{-z/2H} \mathcal{Z}_1(z) \begin{cases} D'_{-1/2}(y_1/b_1) D_{-1/2}(-y/b_1) & \text{if } -\infty < y < y_1 \\ D'_{-1/2}(-y_1/b_1) D_{-1/2}(y/b_1) & \text{if } y_1 < y < \infty, \end{cases} \quad (2.67)$$

where $D'_{-1/2}(x) = dD_{-1/2}(x)/dx$ and $D'_{-1/2}(-x) = dD_{-1/2}(-x)/dx$. Note that $\psi(y, z)$ is discontinuous at $y = y_1$. With the aid of (2.38), the fractional mass flux in the summer hemisphere cell as a function of vertical wavenumber m for an infinitesimally thin ITCZ is

$$\left(\text{Summer Cell} \right)_m = \frac{\hat{\psi}_m(y_1^+)}{\hat{\psi}_m(y_1^+) - \hat{\psi}_m(y_1^-)} = \frac{1}{\sqrt{2}} D'_{-1/2}(-y_1/b_m) D_{-1/2}(y_1/b_m), \quad (2.68)$$

and the fractional mass flux in the winter hemisphere cell as a function of vertical wavenumber m for an infinitesimally thin ITCZ is

$$\left(\text{Winter Cell} \right)_m = \frac{-\hat{\psi}_m(y_1^-)}{\hat{\psi}_m(y_1^+) - \hat{\psi}_m(y_1^-)} = -\frac{1}{\sqrt{2}} D'_{-1/2}(y_1/b_m) D_{-1/2}(-y_1/b_m). \quad (2.69)$$

Plots of (2.65), (2.66), (2.68), and (2.69) are shown in Fig. 2.15 for $m = 0, 1, 2$ and for the four ITCZ widths: $(y_2 - y_1) \rightarrow 0$, $(y_2 - y_1) = 500, 1000, 2000$ km. For example, when $m = 1$, the winter cell carries approximately 2–4 times the mass flux of the summer cell, increasing as the width of the ITCZ increases. This result is in close agreement with the numerical calculations of Hack et al. (1989) and Hack and Schubert (1990). As m increases, the asymmetry between the winter and summer cells also increases. Complicated heating structures force higher vertical modes, therefore we expect there to be larger asymmetries between the winter and summer cells compared to the typical $m = 1$ mode. Both the width and vertical structure of diabatic heating in

the ITCZ help explain the large observed asymmetries between the zonally and monthly averaged Hadley cells.

Now consider the fractional mass flux for Ekman pumping in the ITCZ in the absence of diabatic heating. The fractional mass flux in the shallow summer Hadley cell for an infinitesimally thin ITCZ is

$$\text{Summer Cell} = \frac{\psi(y_1^+, z)}{\psi(y_1^+, z) - \psi(y_1^-, z)} = \frac{\sum_{m=0}^{\infty} b_m \mathcal{Z}_m(0) \mathcal{Z}_m(z) D'_{-1/2}(-y_1/b_m) D_{-1/2}(y_1/b_m)}{\sum_{m=0}^{\infty} b_m \mathcal{Z}_m(0) \mathcal{Z}_m(z)}, \quad (2.70)$$

and the fractional mass flux in the shallow winter Hadley cell for an infinitesimally thin ITCZ is

$$\text{Winter Cell} = \frac{-\psi(y_1^-, z)}{\psi(y_1^+, z) - \psi(y_1^-, z)} = -\frac{\sum_{m=0}^{\infty} b_m \mathcal{Z}_m(0) \mathcal{Z}_m(z) D'_{-1/2}(y_1/b_m) D_{-1/2}(-y_1/b_m)}{\sum_{m=0}^{\infty} b_m \mathcal{Z}_m(0) \mathcal{Z}_m(z)}. \quad (2.71)$$

Plots of (2.70) and (2.71) at $z = 0$ are shown in Fig. 2.16. The maximum asymmetry between the winter and summer shallow Hadley cells occurs relatively far from the equator (2800-2900 km). This result is surprising since the shallow Hadley circulation was expected to be made up of many high vertical wavenumbers, which decrease in equatorial Rossby length as m increases. Below the total solution in Fig. 2.16, the contributions by the $m = 0, 1, 2$ modes are illustrated, and they show that the majority of the solution is comprised of the external $m = 0$ mode solution (more than 95% of the total solution). The external mode tends to play a large role in solutions at the lower boundary, as discussed in Fulton (1980).

It is also interesting to note that as z increases, the contributions from higher m modes increases, therefore the maximum asymmetry between the winter and summer cells changes in magnitude and location as a function of z . The location of maximum asymmetry between the winter and summer cells seems to depend highly on the dominant vertical normal modes in the ITCZ so

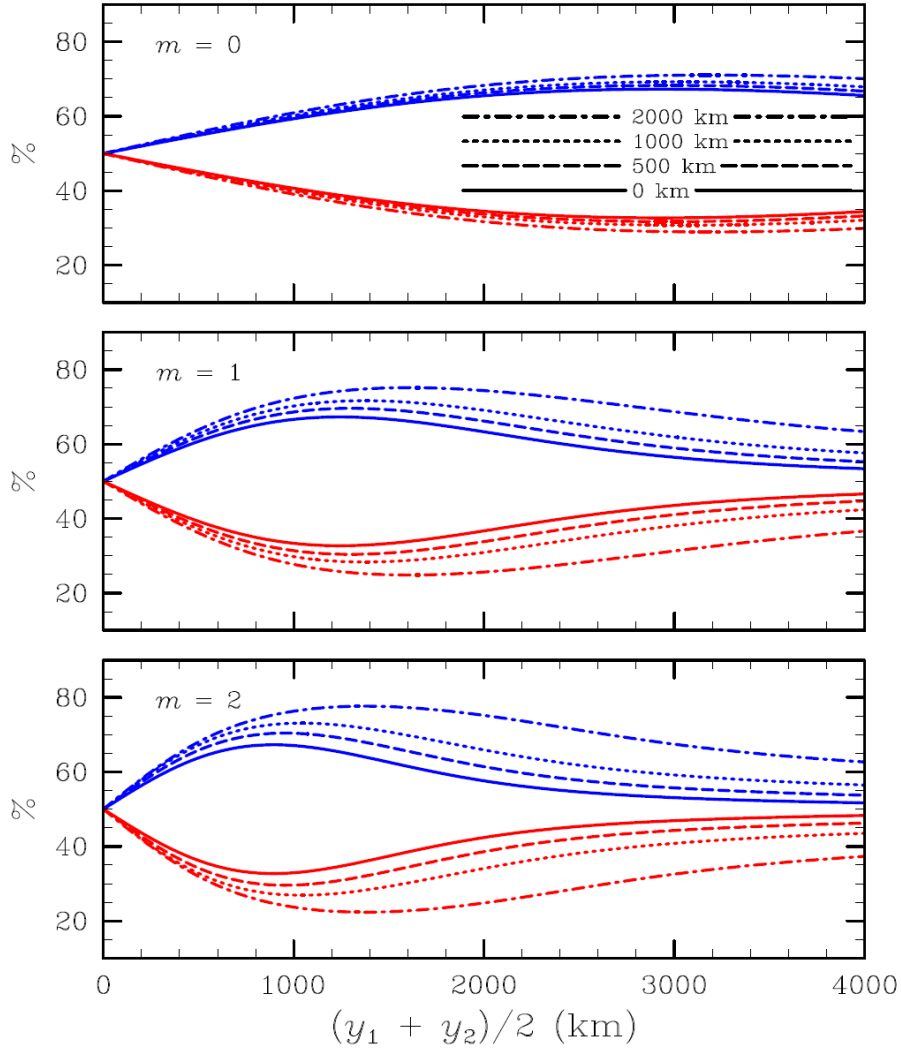


FIG. 2.15. Percentage of the total mass flux carried by the summer hemisphere Hadley cell (red curves) and the winter hemisphere Hadley cell (blue curves) forced by diabatic heating for four ITCZ widths: infinitesimally thin $(y_2 - y_1) \rightarrow 0$, $(y_2 - y_1) = 500, 1000, 2000$ km. Three vertical modes are shown, $m = 0, 1, 2$.

that as vertical wavenumber increases, the solutions become more confined in the meridional direction (refer to the Green's function). The change in asymmetry between the winter and summer shallow Hadley cells as the ITCZ widens is not shown since the results are consistent with the results for the diabatic heating. In fact, the ideas of asymmetry are quite similar for both the deep and shallow Hadley circulations. The main difference lies in their spectrum of equatorial Rossby lengths.

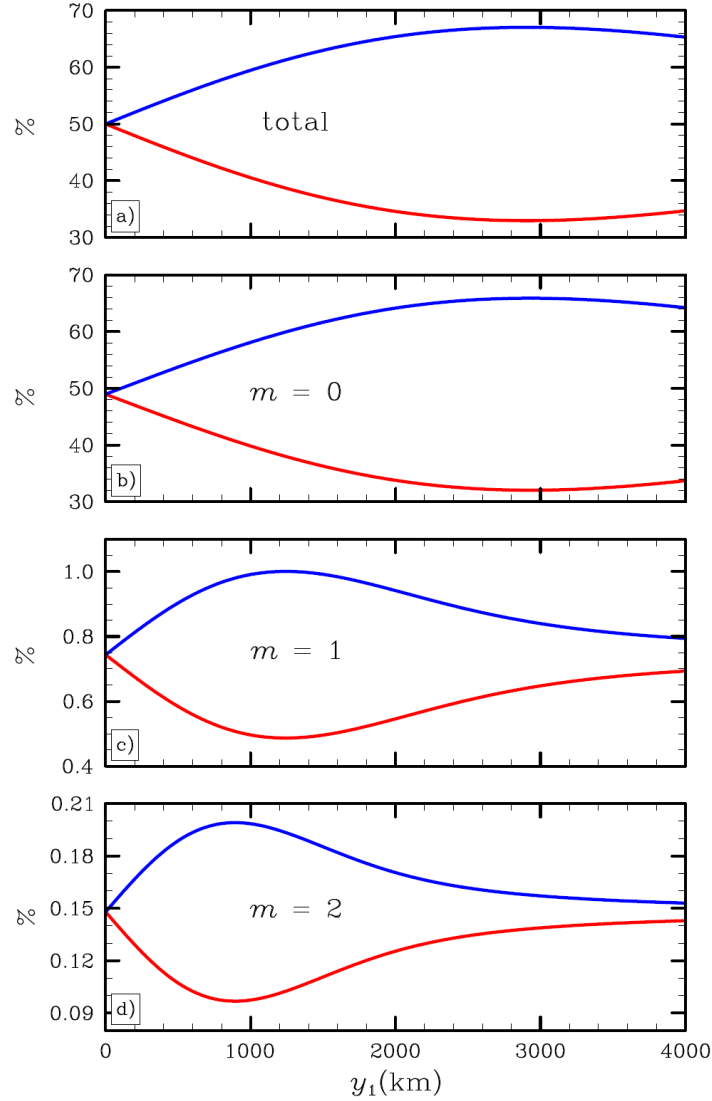


FIG. 2.16. Percentage of the total mass flux carried by the summer hemisphere Hadley cell (red curves) and the winter hemisphere Hadley cell (blue curves) forced by Ekman pumping at the top of the boundary layer for an infinitesimally thin ITCZ. The four panels signify: a) total solution, b) contribution from the $m = 0$ mode, c) contribution from the $m = 1$ mode, and d) contribution from the $m = 2$ mode.

2.9. CONCLUDING REMARKS

In this study, the effects of diabatic heating and Ekman pumping in the ITCZ were explored using an idealized model on the equatorial β -plane. The analysis used a linear zonally symmetric model of the inviscid interior of the tropical atmosphere forced by two prescribed forcings in the ITCZ: i) deep diabatic heating and ii) Ekman pumping at the top of the boundary layer. The results

demonstrate that deep diabatic heating in the ITCZ forces a deep overturning circulation in the absence of Ekman pumping, which we call the deep Hadley circulation. When Ekman pumping at the top of the boundary layer is present, there is a shallow overturning circulation, with divergence at the top of the boundary layer up to about 2 km above the top of the boundary layer, which we refer to as the shallow Hadley circulation. Both forcings illustrate an increase in asymmetry between the winter and summer Hadley cells until the ITCZ is displaced at a particular distance away from the equator. This distance depends on the dominant vertical normal modes in the ITCZ so that as vertical wavenumber increases, the solutions become more confined in the meridional direction.

The solution method described in section 3 begins with a vertical transform that involves solving the Sturm-Liouville problem, with a nonzero lower boundary condition, and then solves the horizontal structure equation (2.28) using Green's function since it obeys an equation similar to the ψ field. The fields that force the response in the ITCZ using the idealized equatorial β -plane model are the meridional structure of the diabatic heating and the Ekman pumping at the top of the boundary layer, while the inertial stability and static stability are shaping parameters. Since the static stability is constant in the solutions presented here, the spatial variability of the inertial stability $\beta^2 y^2$ plays the most important role in the asymmetry between the winter and summer Hadley cells. A physical interpretation is that fluid parcels forced near the equator by diabatic and frictional processes tend to move much more easily in the horizontal direction because the resistance to horizontal motion (i.e., inertial stability) is significantly smaller than the resistance to vertical motion (i.e., static stability). The asymmetries inherent in both the deep and shallow Hadley circulations were also explored for different ITCZ widths. The results indicate that as the ITCZ becomes wider, the asymmetry increases, agreeing well with Hack and Schubert (1990). A

new finding is that as the vertical structure of the forcing becomes more complicated (as vertical wavenumber increases), the asymmetry increases as well. The asymmetries between the winter and summer shallow Hadley cells at $z = 0$ that this model produces have somewhat of a different structure than expected since the majority of the solution is comprised of the external $m = 0$ vertical mode solution. In a model where the boundary layer is explicitly simulated, the shallow Hadley solution may look slightly different because it may have a larger percentage of contributions from higher internal vertical modes.

Future research on the topic of deep and shallow overturning circulations should explore a model that is able to produce solutions of both the boundary layer and the inviscid interior and should explore the role of higher internal modes. Such a model should also explore the role of combined barotropic and baroclinic instability as well as the effect of the basic state fields on the shallow Hadley circulation. The idealized model used in this study suffers from not being able to explore such aspects. The understanding of the ITCZ in the eastern Pacific involves ITCZ breakdown and diabatic heating dominates the monthly average solution, leading to deep overturning circulations. The time period between ITCZ breakdown and reformation is influenced by boundary layer processes, and most likely, shallow overturning circulations. It is still unclear whether shallow overturning circulations are due mostly to shallow diabatic heating or boundary layer effects such as Ekman pumping or vertical motion due to SST gradients. Therefore, the prevalence of shallow precipitating profiles and their contribution to shallow overturning circulations should also be explored.

CHAPTER 3

Deep and Shallow Vertical Motions in the Tropical Eastern Pacific in the YOTC reanalysis

3.1. SYNOPSIS

This chapter analyzes the vertical structure of the vertical pressure velocity field, ω , in the tropical eastern Pacific Ocean (80°W–150°W) using the Year of Tropical Convection (YOTC) reanalysis. YOTC provides a great opportunity to investigate tropical features at high spatial resolutions because of increased satellite coverage, especially over the tropical oceans, where the transient dynamics are not well understood. Also, both modest La Niña (October 2008–April 2009) and El Niño (May 2009–April 2010) conditions were observed in YOTC. My analyses focus on seasonal changes in ω while retaining the 6 hourly temporal variability of the YOTC fields. The most striking feature was the zonally-oriented narrow line of shallow vertical motions in the Intertropical Convergence Zone (ITCZ), especially in the 115°W–150°W region. However, this region did experience some deepening during the summer El Niño months of May–October 2009. Vertical motions in the 80°W–115°W eastern Pacific were generally dominated by deep vertical motions, especially in May–October in both 2008 and 2009. During these summer months, deeper rising motions seem to correspond with warmer sea surface temperatures, in line with past studies. The months of November–January of both years highlight the narrow, shallow vertical motions associated with the ITCZ and activity to the north and south, where it is believed that Tropical Upper Tropospheric Troughs (TUTTs) and the South Pacific Convergence Zone (SPCZ) provide deeper vertical motions north of the ITCZ and in the southern hemisphere, respectively. Finally, the months of February–April exhibit significant differences near the equator, where February–April

2009 illustrated a double shallow ITCZ structure while February–April 2010 had a single ITCZ just north of the equator with both shallow and deep rising motions.

3.2. INTRODUCTION

Tropical diabatic heating profiles and their associated large-scale circulations have been investigated by many studies, such as the pioneering work of Yanai et al. (1973). It was assumed for some time that deep convective diabatic heating profiles of the first baroclinic mode dominated the tropical atmosphere. As observations of diabatic heating profiles in different tropical regions have increased it has become apparent that other precipitating diabatic heating profiles, such as shallow convective and stratiform profiles are also prevalent. A few relevant studies that investigate the variability of circulations associated with shallow, deep, and stratiform diabatic heating are Schumacher et al. (2004), Zhang and Hagos (2009), Hagos et al. (2010), Takayabu et al. (2010), Ling and Zhang (2013), and Yokoyama et al. (2014). It is likely that tropical regions where sea surface temperatures (SSTs) are relatively cool may be less favorable for deep convective diabatic heating profiles since convection relies on the contrast of lower tropospheric temperatures with upper tropospheric temperatures to first order through ideas of moist static energy (Neelin and Held 1987). There has also been evidence that regions with large SST gradients tend to have relatively shallow vertical motions because of larger boundary layer convergence (Back and Bretherton 2006, 2009a,b; Nolan et al. 2007). Gonzalez and Mora Rojas (2014) illustrated that shallow vertical motions can be attributed to Ekman pumping at the top of boundary layer not being able to penetrate deep into the free troposphere of the Intertropical Convergence Zone (ITCZ).

The goal of this chapter is to further look into the spatial variability of vertical motions in the eastern Pacific region using the Year of Tropical Convection (YOTC) reanalysis since it has both high horizontal and vertical resolution. Previous studies tend to take monthly or seasonal

averages while we will retain the full temporal variability of the YOTC fields. Also, McNoldy et al. (2004) suggest that the European Centre for Medium-Range Weather Forecasts (ECMWF) reanalysis products are superior in the eastern Pacific.

This chapter is organized in the following way. Section 3.3 describes the YOTC reanalysis fields to be analyzed while section 3.4 shows seasonal plots of the vertical motion, SSTs, and diabatic heating. Concluding remarks are made in section 3.5.

3.3. DATA

YOTC is a global reanalysis product spanning the time period of May 2008–April 2010 that uses four-dimensional variational data assimilation at a horizontal resolution of 0.25 degrees (T799), with 91 hybrid vertical levels. It is similar to the ECMWF Re-Analysis (ERA-Interim) with a number of additional observations using satellite data, in-situ data, and a new high resolution modeling framework. Just like ERA-Interim, the fields are produced every six hours, at 0Z, 6Z, 12Z, and 18Z. In this chapter, we analyze the vertical pressure velocity field ω , SSTs, and diabatic heating Q_1/c_p fields at a horizontal resolution of 0.125 degrees. The ω field was interpolated from all hybrid vertical levels at or below 100 hPa to pressure levels using the NCAR Command Language function `vinth2p` while the diabatic heating was only available at 15 pressure levels below 100 hPa. Since YOTC does not explicitly provide the diabatic heating field, it was computed using the individual terms that make up the diabatic heating using the equation $Q_1 = Q_{\text{conv}} + Q_{\text{cloud}} + Q_{\text{rad}} + Q_{\text{turb}}$, where Q_{conv} is the temperature tendency from deep and shallow convection, Q_{cloud} is the temperature tendency from the cloud scheme, Q_{rad} is the temperature tendency from radiation, and Q_{turb} is the temperature tendency from turbulent diffusion and sub-grid orography.

3.4. RESULTS

In order to better understand the variability of vertical motions in the tropical eastern (80°W–150°W) Pacific, vertical profiles of ω were divided into shallow and deep rising motions ($\omega < 0$). This was done by defining the lower troposphere as the layer below 650 hPa and the upper troposphere as the layer including 650 hPa until 100 hPa. We also used 600 and 700 hPa as the level separating the upper and lower troposphere and did not see qualitatively different results. The absolute maximum of the lower troposphere was taken as the dominant shallow ω profile and the absolute maximum of the upper troposphere was taken as the dominant deep ω profile. If the vertical profile of ω had maxima in both the lower and upper troposphere, the regime with the stronger vertical motion was selected. Also, the absolute maximum in rising motion in each layer was required to be above a threshold of 2 hPa hr⁻¹, which helps eliminate weak cases.

Figure 3.1 shows a map of the percentage of the time the vertical profile of ω was dominated by either shallow or deep vertical motions along with SSTs for the entire YOTC period, May 2008–April 2010. It is interesting to note that shallow vertical motions are relatively latitudinally narrow and do not extend far away from the equator (top panel). Also, there is a relative minimum near the equator in the shallow ω regime, which is related to the equatorial cold tongue. Deep vertical motions, shown in the bottom panel of Fig. 3.1, are most prevalent north of shallow vertical motions and are much broader in latitudinal extent. The reasons for these features will be explored in more detail below, where we analyze individual seasons.

Note that there were modest La Nina and El Niño conditions during the YOTC period, which may account for many of the features shown in the analyses of particular seasons. Figure 3.2 shows the Niño 1+2 (80°W–90°W, 0–10°S) and Niño 3 region (90°W–150°W, 5°S–5°N) indices using version 3 of the Extended Reconstructed Sea Surface Temperature (ERSST) dataset (Smith

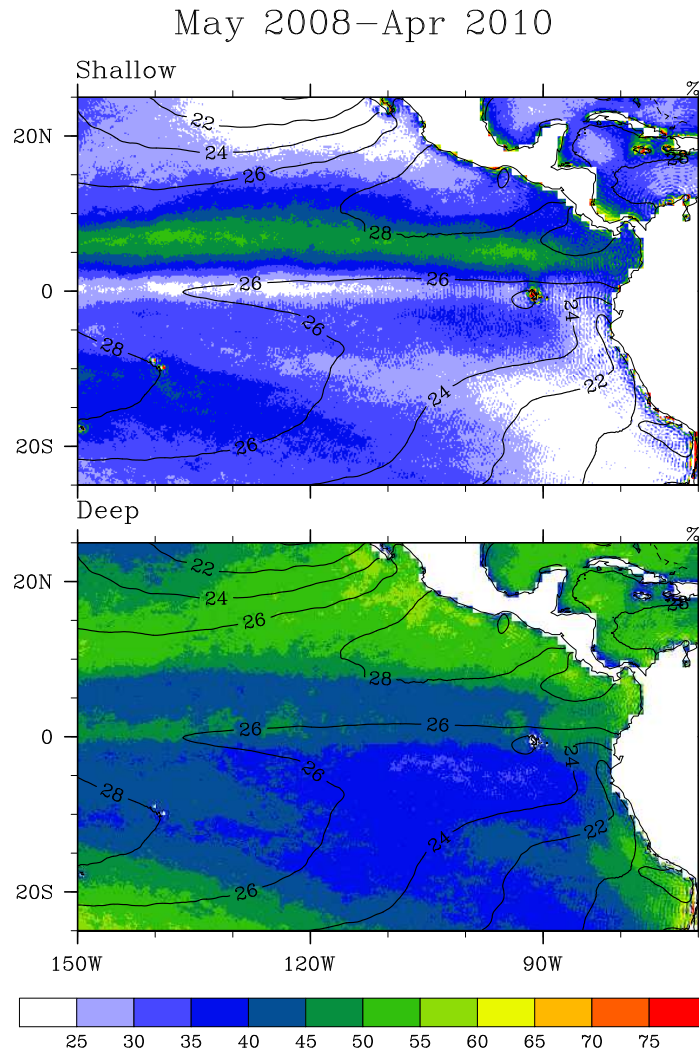


FIG. 3.1. Percentage (%) of the output times during the entire YOTC period (May 2008–April 2010) that were dominated by either shallow or deep rising motions above a threshold of 2 hPa hr^{-1} in the shading and SST field ($^{\circ}\text{C}$) in the contours. The SST contour interval is 2°C .

et al. 2008) and SSTs from the YOTC reanalysis. The base period used to compute anomalies is 1981–2010, where SSTs from ERSST are used as the ERSST base period and ERA-Interim SSTs are used as the base period of the YOTC anomalies. The YOTC reanalysis seems to replicate the conditions seen in ERSST quite well, with some discrepancies (more La Nina-like in YOTC) during May and June 2008 in the ER Niño 3 region, and February–April 2010 in the ER Niño 1+2 region.

El Niño regions during YOTC

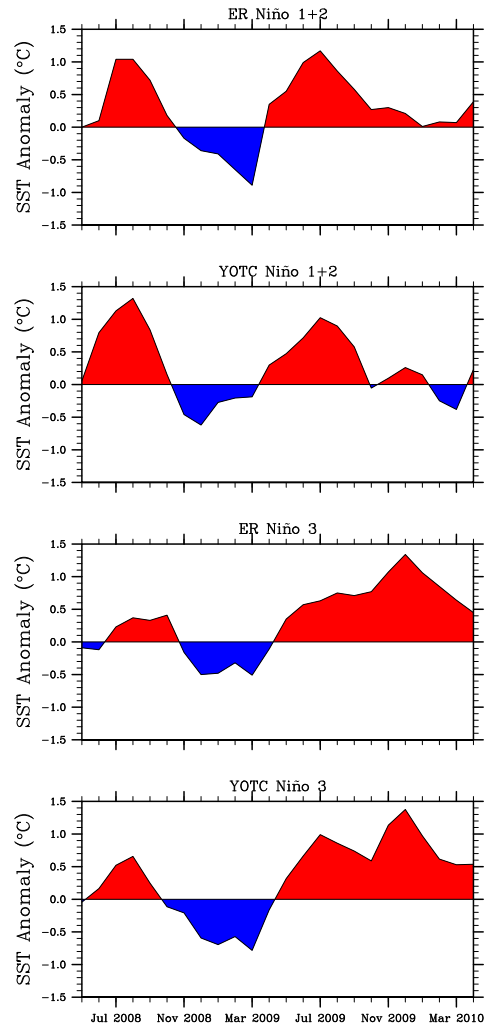


FIG. 3.2. SST anomalies ($^{\circ}\text{C}$) from the Extended Reconstructed Sea Surface Temperature (ERSST) dataset version 3 (Smith et al. 2008), and YOTC during May 2008–April 2010 for the Niño 1+2 (80°W – 90°W , 0 – 10°S) and Niño 3 region (90°W – 150°W , 5°S – 5°N). The base period used to compute anomalies from is 1981–2010, where SSTs from ERSST are used for the ERSST base period and ERA-Interim SSTs are used as the base period of YOTC anomalies.

Figures 3.3 and 3.4 illustrate the percentage of the time the vertical profile of ω was dominated by either shallow or deep rising motions along with isolines of the SST field during May–July 2008 and August–October 2008, respectively. The 80°W – 115°W region was dominated by deep vertical motions covering a broad area while the 115°W – 150°W region was dominated by shallow

and latitudinally concentrated vertical motions which seem to resemble a thin ITCZ. It is not surprising that vertical motions in the eastern Pacific are typically deeper since the SSTs are warmer, as discussed by Neelin and Held (1987). Also, there is typically more tropical cyclone activity in this part of the eastern Pacific and 2008 had the most active North American monsoon since 1941 (Waliser and Coauthors 2012). The North American monsoon typically occurs during June–September and impacts not only the American west coasts but also the eastern Pacific through westward propagating disturbances (Higgins and Coauthors 2006; Mapes et al. 2003).

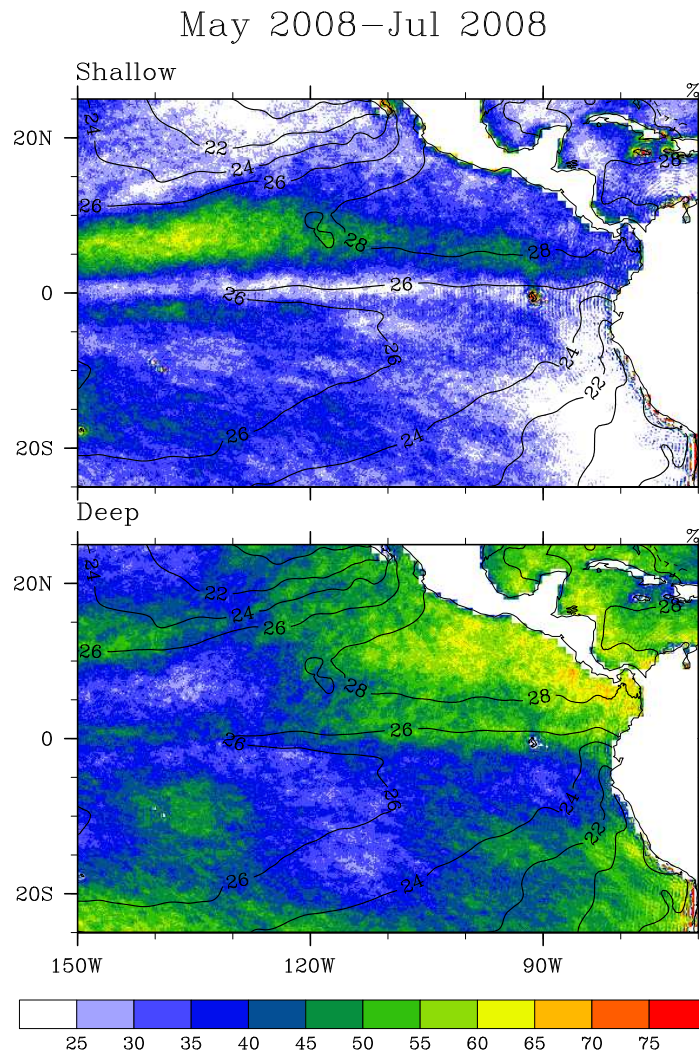


FIG. 3.3. Percentage (%) of the output times during May–July 2008 that were dominated by either shallow or deep rising motions above a threshold of 2 hPa hr^{-1} in the shading and SST field ($^{\circ}\text{C}$) in the contours. The SST contour interval is 2°C .

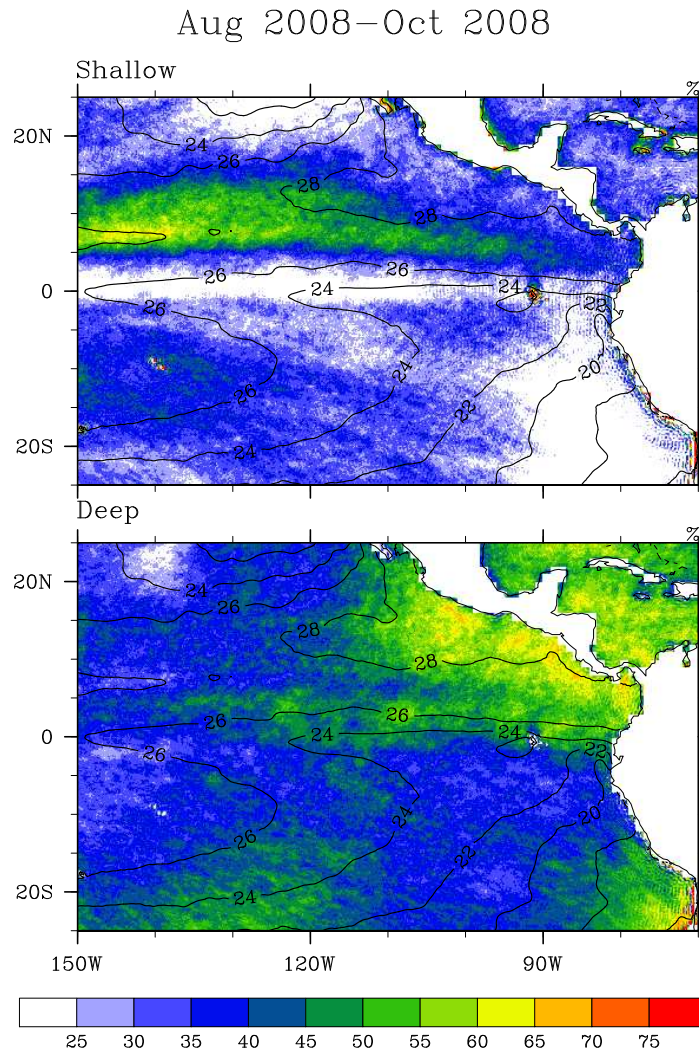


FIG. 3.4. Percentage (%) of the output times during August–October 2008 that were dominated by either shallow or deep rising motions above a threshold of 2 hPa hr^{-1} in the shading and SST field ($^{\circ}\text{C}$) in the contours. The SST contour interval is 2°C .

During May–October of 2009, there were deeper vertical motions, especially in the 115°W – 150°W region, as shown in Figures 3.5 for August–October 2009. This increase in coverage of deep rising motions is most likely due to the strong El Niño conditions in both the Niño 1+2 and 3 regions, as shown in Figure 3.2.

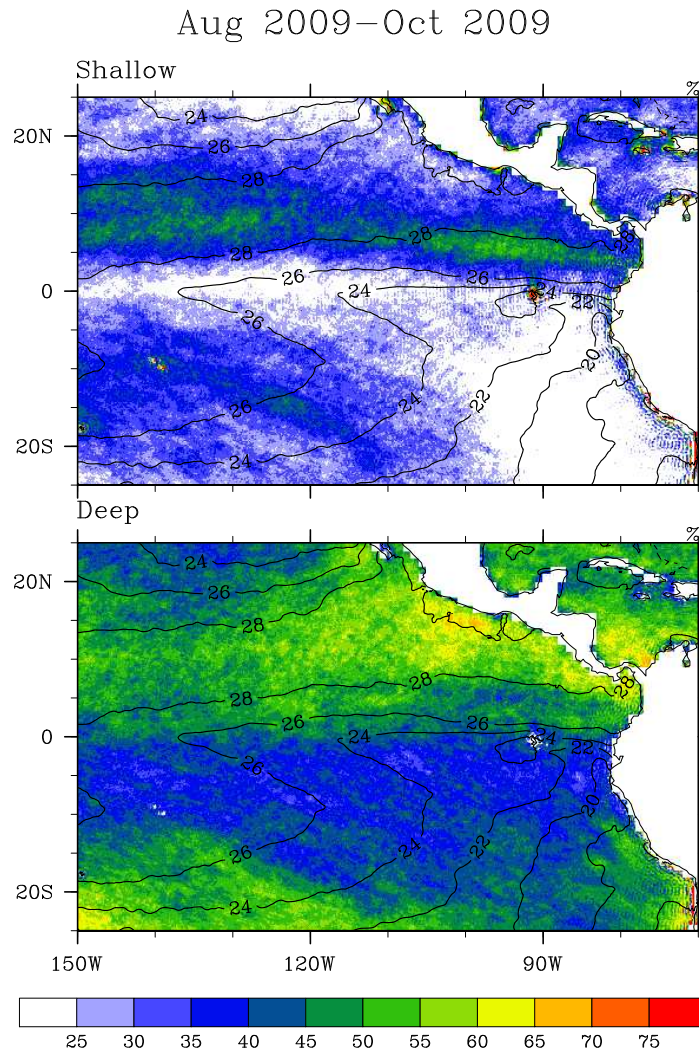


FIG. 3.5. Same as Fig. 3.4, but for August–October 2009.

Figure 3.6 shows a map of the percentage of the time the vertical profile of ω was dominated by either shallow or deep vertical motions along with contour lines of the SST field during November 2008–January 2009. There are three regions of interest: the ITCZ region just north of the equator, the tropical to subtropical transition region north of the ITCZ, and the South Pacific Convergence Zone (SPCZ). The ITCZ region was once again a well-defined, thin band of shallow vertical motion. In fact, shallow rising motions occur about 3/4 of the YOTC output times in the 90°W–110°W region during November 2008–January 2009. To try and understand why there is

such prevalent and latitudinally confined shallow motion in this region during these months, we take a look at the diabatic heating field.

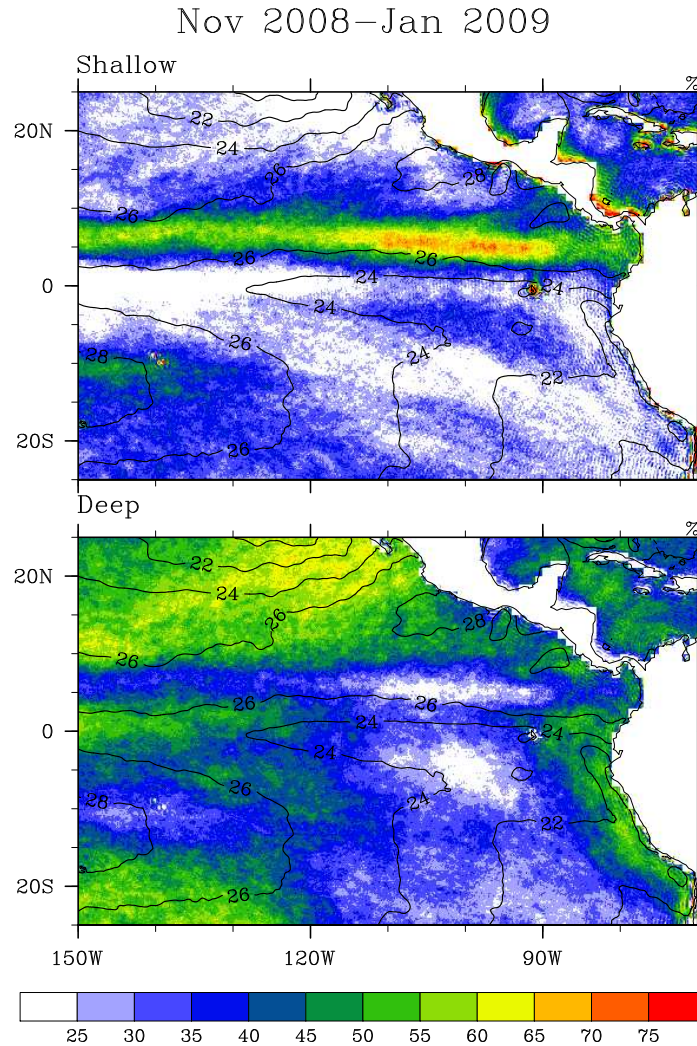


FIG. 3.6. Percentage (%) of the output times during November 2008–January 2009 that were dominated by either shallow or deep rising motions above a threshold of 2 hPa hr^{-1} in the shading and SST field ($^{\circ}\text{C}$) in the contours. The SST contour interval is 2°C .

Figure 3.7 shows the area-averaged ω and diabatic heating Q_1/c_p over the ocean in two regions: 0° – 10°N , 80°W – 115° (left panels), and 0° – 10°N , 115°W – 150° (right panels) during January 2009. A daily running mean filter was applied to both fields to remove the diurnal cycle. The vertical profile of ω and Q_1/c_p are typically shallow in both regions and are often weak in magnitude (e.g.,

$Q_1/c_p \leq 2 \text{ K day}^{-1}$). There seems to be a good correlation between the two fields below 650 hPa, suggesting that shallow vertical motions in YOTC are possibly due to shallow diabatic heating. However, since the diabatic heating is often weak, it is also quite possible that other adiabatic processes might be important as well. For example, vertical motion at the top of the boundary layer associated with Ekman convergence and meridional SST gradients may help describe why vertical motions are shallow, as discussed in Gonzalez and Mora Rojas (2014) and Back and Bretherton (2009b).

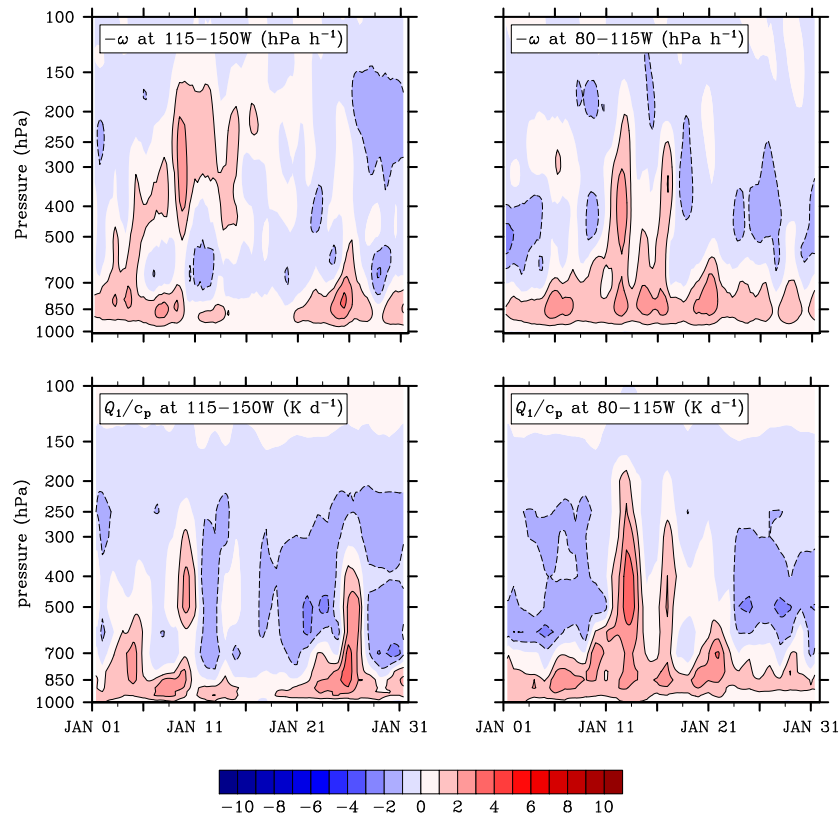


FIG. 3.7. January 2009 area averaged vertical motion ($-\omega$, hPa h^{-1}) in the top panels and diabatic heating field (Q_1/c_p , K d^{-1}) in the bottom panels. All plots were averaged over 0° - 10°N and only over the ocean, and the left panels were also averaged over 115°W - 150°W while the right panels were averaged over 80°W - 115°W . Note: The contour intervals are 1 hPa h^{-1} and 1 K d^{-1} .

Returning to Figure 3.6, the region north of the ITCZ (110°W - 150°W) experiences deep vertical motions that are likely associated with Tropical Upper Tropospheric Troughs (TUTTs) during

November 2008–January 2009. These events occur during boreal fall–spring and typically last a few days to a week and involve significant interaction between the tropics and subtropics (Webster and Holton 1982). In fact, Masarik and Schubert (2013) used the YOTC reanalysis to document a moderate TUTT during January 2009 (their Fig. 2). The SPCZ was also a prominent feature during November 2008–January 2009 in the 120°W–150°W region. Many global models tend to overproduce a double ITCZ in the eastern Pacific as a zonally elongated SPCZ (Mechoso and Coauthors 1995), but the YOTC reanalysis does not seem to do this.

The resulting deep vs. shallow ω plot for November–January 2010 is not shown since these months agree well with those of 2009, except with a slight increase in deep vertical motions. Once again, it is likely that the modest El Niño conditions played a role during these months.

During February–April 2009 and 2010 vertical profiles of ω and SST differed significantly over the eastern Pacific attributed to the effects of the 2009 La Niña and 2010 El Niño, as shown in Figures 3.8 and 3.9. February–April 2009 had a double ITCZ structure dominated mainly by shallow vertical motions while 2010 was dominated by an array of shallow and deep vertical motions in the form of a single, near-equatorial ITCZ. These results agree with Lietzke et al. (2001), who suggested that the double ITCZ in the eastern Pacific is most prominent during La Niña years since the equatorial cold tongue is present, whereas neutral and El Niño years exhibit a single ITCZ slightly on or north of the equator. The region north of the ITCZ once again exhibited deep vertical motions in February–April of both years most likely associated with TUTT activity. Also, the region southwest of the ITCZ was dominated by an array of shallow and deep vertical motions during both February–April of 2009 and 2010, likely associated with activity in the SPCZ.

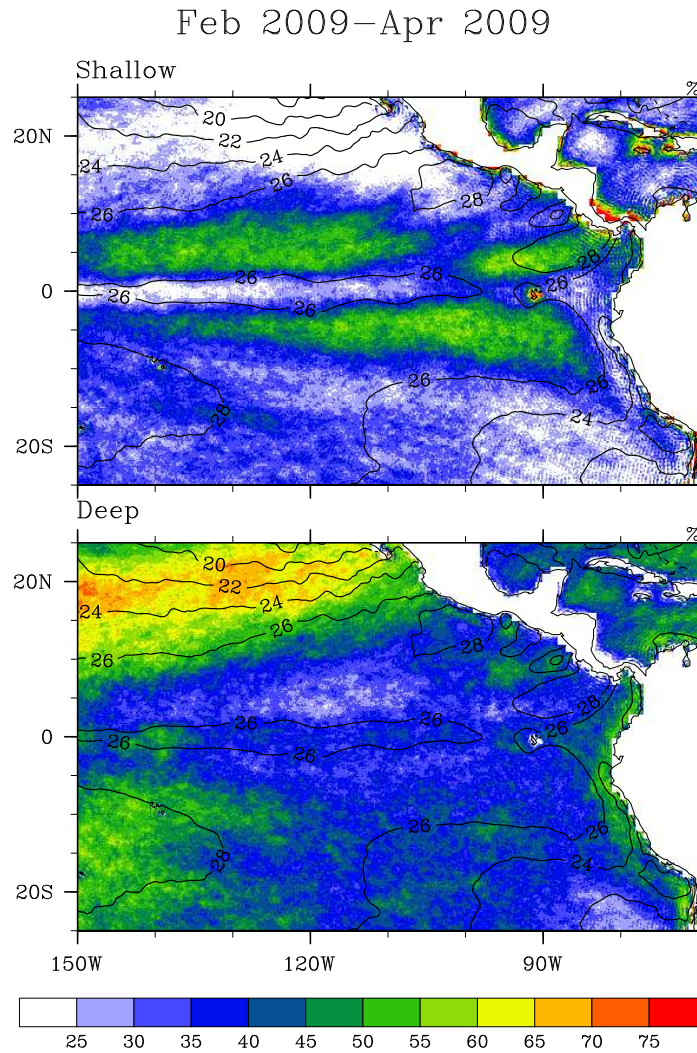


FIG. 3.8. Percentage (%) of the output times during February–April 2009 that were dominated by either shallow or deep rising motions above a threshold of 2 hPa hr^{-1} in the shading and SST field ($^{\circ}\text{C}$) in the contours. The SST contour interval is 2°C .

3.5. CONCLUDING REMARKS

We analyzed vertical profiles of the vertical pressure velocity, ω , during the YOTC reanalysis of May 2008–April 2010 in the tropical eastern Pacific (80°W – 150°W). We defined the vertical motions as being dominated by a shallow (up to 650 hPa) or deep peak (650 hPa to 100 hPa). During May–October of 2008, the 80°W – 115°W region of the eastern Pacific was dominated by deep ω profiles covering a broad area while the 115°W – 150°W region was dominated by shallower,

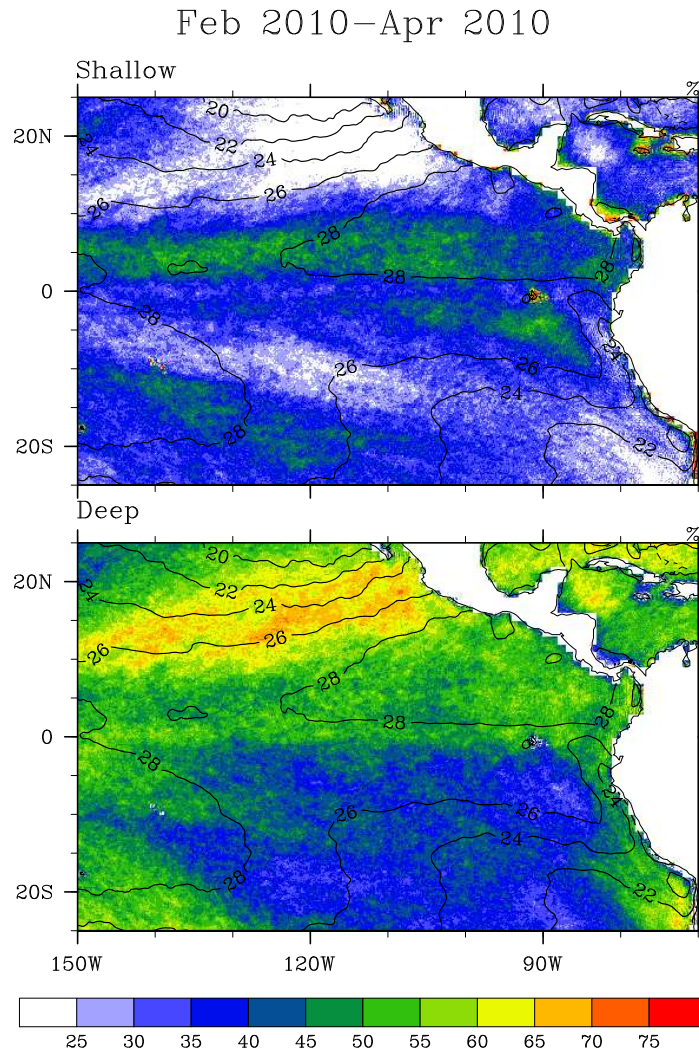


FIG. 3.9. Same as Fig. 3.8, but for February–April 2010.

more latitudinally confined ITCZ-like vertical motions. Vertical motions deepened the next year during these months, especially in the 115°W–150°W region. However, deep rising motion is still more prevalent in the 80°W–115°W region. A possible explanation for this is that 80°W–115°W tends to be affected more by convection propagating westward from the North American monsoon and tropical cyclones.

From October–January of both years of YOTC, the eastern Pacific ITCZ is strongly dominated by shallow ω profiles. We analyzed the diabatic heating field during these months and find that

diabatic heating was shallower and relatively weak in magnitude, which agrees with the cooler SSTs. It seems that the diabatic heating field qualitatively agrees with the shallow vertical motions. Also, with the lack of significant diabatic heating, adiabatic processes might be important for understanding the vertical motion field. It is possible that Ekman pumping at the top of the boundary layer cannot penetrate very deep into the free troposphere in the absence of significant diabatic heating. Also, these months may also show the effects of activity in the form of TUTTs and the SPCZ. TUTTs typically account for deep vertical motions while the SPCZ can be deep or shallow.

During February–April 2009 shallow profiles dominated in the ITCZ region, while there were an array of shallow and deep ω profiles during February–April 2010 in the ITCZ. Rising motion was usually north of the equator, except during La Niña conditions in 2009 when a double ITCZ structure was prominent. Once again, TUTTs account for deep vertical motions northwest of the ITCZ while the SPCZ account for an array of vertical motions south of the equator.

We believe that the YOTC reanalysis has provided an opportunity to analyze fields such as ω at a high resolution for two contrasting years in a region where convection and circulations are sensitive to the background conditions. Future work should concentrate on variability of large-scale convection and circulations on smaller scales to continue improving our understanding of transient convection and circulations in the tropics.

CHAPTER 4

Transient Hadley Circulations

4.1. SYNOPSIS

This chapter examines the transient dynamics of large-scale, zonally symmetric overturning circulations in the tropical troposphere. The dynamics are discussed in the context of idealized analytical solutions of the meridional circulation equation arising in an equatorial β -plane model of the Hadley circulation. This partial differential equation for the meridional circulation can be solved by first performing a vertical transform to obtain a set of horizontal structure equations, and then performing a horizontal Hermite transform to obtain a set of second order ordinary differential equations in time. The solutions of these ordinary differential equations contain terms for the slow, quasi-balanced part of the response and terms for the transient, zonally symmetric, inertia-gravity wave part of the response. When the ITCZ is located off the equator, both parts of the response reveal a basic asymmetry between the winter and summer hemispheres, with the winter hemisphere side containing most of the quasi-balanced compensating subsidence and most of the transient inertia-gravity wave activity. Also, the inertia-gravity waves travel in packets, causing the Hadley cells to pulsate on timescales of about 1, 2, and 3 days for diabatic heating of the external, first internal, and second internal modes. These basic dynamical aspects of the Hadley circulation are revealed in the upper tropospheric water vapor patterns observed by the $6.7 \mu\text{m}$ water vapor channels on the GOES satellites over the Atlantic and eastern Pacific.

4.2. INTRODUCTION

Figure 4.1 shows a typical, boreal summer $6.7 \mu\text{m}$ water vapor image of the eastern Pacific from the GOES West satellite. Under clear sky conditions, the $6.7 \mu\text{m}$ channel is sensitive to the vertically averaged humidity in the 200–500 hPa layer, so the dark blue areas on either side of the ITCZ indicate regions of low humidity in the upper troposphere, and hence regions of enhanced subsidence in the downward branches of the summer hemisphere and winter hemisphere Hadley cells. The complete explanation of atmospheric water vapor distributions can be quite complicated and involve several different physical processes, such as the stretching and folding processes associated with the Rossby wave pattern just east of Hawaii in Figure 4.1. For detailed discussions of tropical moisture distributions, including trajectory analysis and the concept of “time since last condensation,” see Sun and Lindzen (1993), Soden and Fu (1995), Salathé and Hartmann (1997), Pierrehumbert (1998), Pierrehumbert and Roca (1998), Galewsky et al. (2005), Sherwood et al. (2006), Cau et al. (2007), and Schreck et al. (2013). In spite of the intricacies involved in comprehensive explanations of tropical water vapor distributions, it appears that, during much of the year, the explanation of the water vapor distribution in the eastern Pacific is simpler than in many other areas. An important part of the explanation lies in the dynamics of the Hadley cells, with the winter hemisphere Hadley cell having a large meridional extent and a large overturning mass flux. These are the aspects on which the present chapter shall focus.

In the theory presented here, only the flow in the inviscid interior (i.e., above the 900 hPa isobaric surface) is explicitly considered. The effects of the frictional boundary layer appear as the lower boundary condition on the inviscid interior. The problem consists of a partial differential equation in (y, z, t) , with appropriate boundary and initial conditions. This problem can be solved by a variety of methods. The methods used here are analytical and provide important insights into

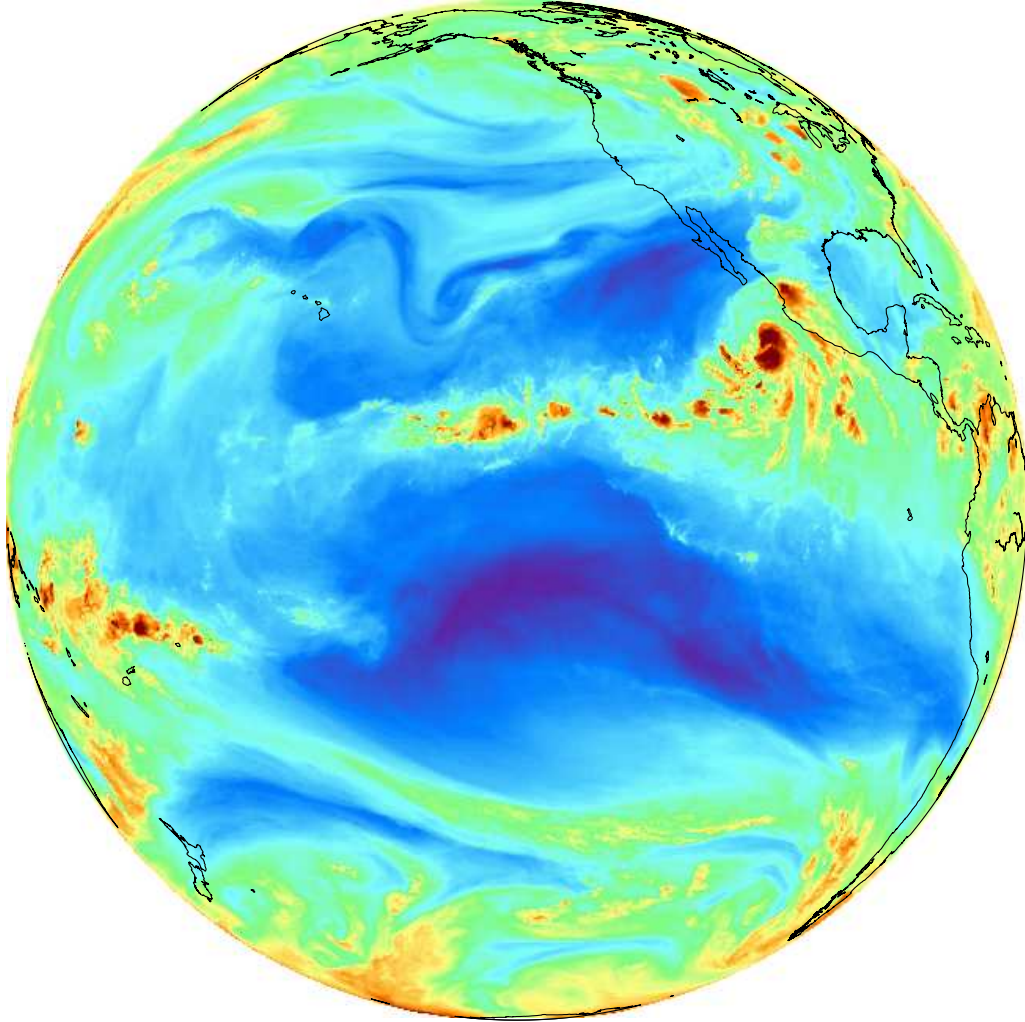


FIG. 4.1. The 06 UTC 25 June 2013 water vapor image ($6.7 \mu\text{m}$) from the GOES West satellite. This image is typical of the eastern Pacific during the boreal summer when the ITCZ is located near $10\text{--}15\text{N}$. The dark blue areas on either side of the ITCZ indicate regions of low humidity in the upper troposphere, and hence regions of enhanced subsidence in the downward branches of the summer hemisphere and winter hemisphere Hadley cells. For a detailed discussion of $6.7 \mu\text{m}$ radiance-to-humidity transformation formulas, see Soden and Bretherton (1993, 1996) and Jackson and Bates (2001).

the dynamics. As described in section 2.4, the first step involves application of a vertical transform that converts the original partial differential equation in (y, z, t) into a system of partial differential equations in (y, t) . In a previous paper (Gonzalez and Mora Rojas 2014), the Green's function approach (evanescent basis functions) was used to solve the slowly forced version of this problem. This approach yields the most physical insight into the quasi-balanced meridional flow and the

fundamental asymmetry between the summer hemisphere and winter hemisphere Hadley cells. As discussed in section 4.5, the present chapter uses the Hermite transform approach (oscillatory basis functions) to solve this problem for forcing on any time scale. This approach yields the most physical insight into the transient aspects of the flow and, in particular, how zonally symmetric inertia-gravity waves can be emitted due to transient convection in the ITCZ.

The importance of equatorially-trapped inertia-gravity waves in large-scale dynamics has long been debated. Traditionally, inertia-gravity waves are filtered out in idealized models, such as those used in Gill (1980) and Chao (1987). This is due to the fact that it is difficult to observe these waves because of their small time and space scales. However, papers such as Takayabu (1994) and Haertel and Kiladis (2004) show that inertia-gravity waves are important for tropical dynamics, and often are coupled to convection. As we will see, this chapter illustrates that equatorially-trapped inertia-gravity waves are the fundamental result of the transient zonally symmetric Hadley circulation. There has been evidence of equatorially-trapped oceanic inertia-gravity waves in sea level and surface meridional wind data over the Pacific Ocean, as shown in Figure 4.2 (Wunsch and Gill 1976). It is possible that the tropical atmosphere may contain a considerable amount of inertia-gravity wave activity which our present observational systems are not capable of detecting. Therefore, it is important to try to understand theoretical aspects of the problem in an idealized model setting.

In order to gain insight into the dynamics of the deep Hadley circulations, this chapter considers zonally symmetric motions in a stratified, compressible atmosphere on the equatorial β -plane. The limitation to zonally symmetric motions is a strong one, because it precludes simulation of Walker-type circulations. However, as we shall see, the zonally symmetric model can yield insight into situations such as the one depicted in Figure 4.1.

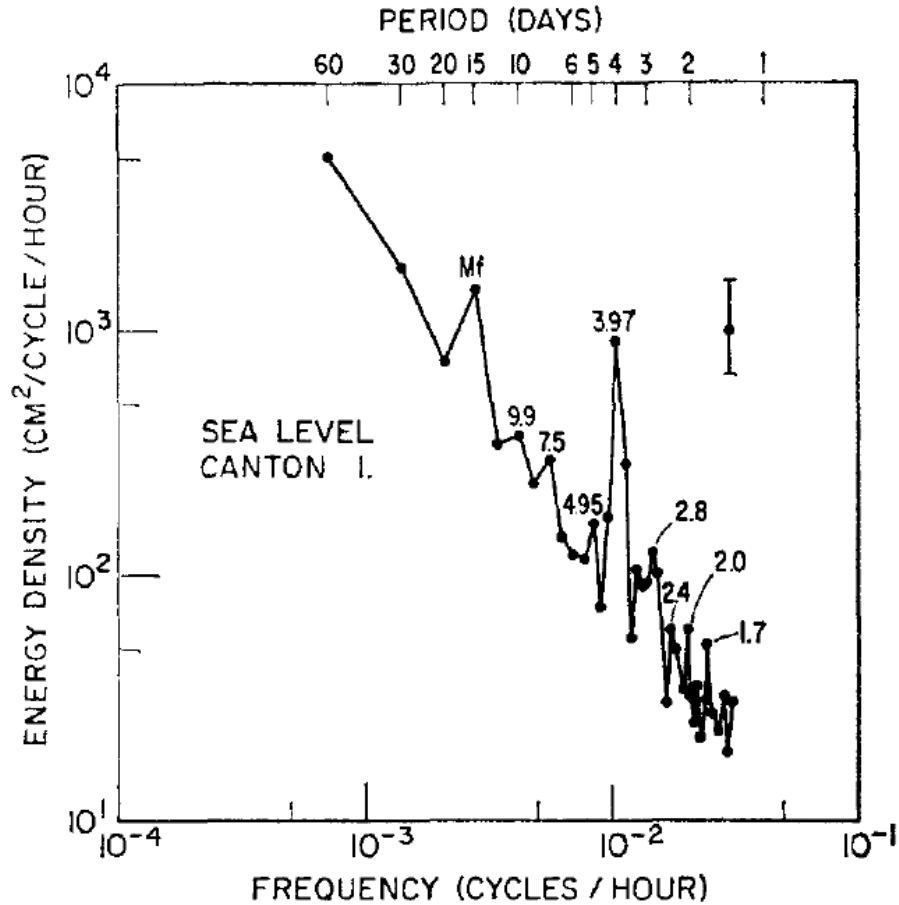


FIG. 4.2. Sea level as a function of frequency and energy density from January 1954–August 4, 1957 at Canton Island (2°S , 171°W). The top axis shows the period (days), and the selected peaks are also denoted in days. Note the 4 day peak has an error bar next to it and Mf is the fortnightly tide. From Wunsch and Gill (1976).

This chapter follows up on work from Gonzalez and Mora Rojas (2014), where they examined some aspects of the dynamics of the deep and shallow Hadley circulations of the tropical troposphere. Their results are based on analytical solutions of the meridional circulation equation derived from the zonally symmetric equations of equatorial β -plane theory. The forcing terms for the meridional circulation equation involve diabatic heating and boundary layer pumping. When these forcing effects are slowly varying in time, the meridional circulation equation simplifies to a second order partial differential equation of elliptic type, so transient inertia-gravity waves are filtered and the meridional circulation has no memory of past forcing, but is simply diagnostically

determined from the present forcing. In the following discussion we shall relax the assumption that forcing effects are slowly varying in time, which means that the meridional circulation equation has an additional term involving two time derivatives, so that it changes from an elliptic partial differential equation to a hyperbolic partial differential equation.

The chapter is organized in the following way. In section 4.3, the primitive equation model is presented and the associated meridional circulation equation is derived. Section 4.4 introduces a Hermite transform in y that converts the set of equations in (y, t) into a set of ordinary differential equations in t . In sections 4.5 and 4.6, we discuss the deep overturning response associated with diabatic forcing in the ITCZ. Derivations of inertia-gravity wave packet properties are shown in section 4.7. Some concluding remarks are presented in section 4.8.

4.3. MODEL EQUATIONS

In order to gain insight into the transient aspects of the Hadley circulation, we consider zonally symmetric motions in a stratified, compressible atmosphere on the equatorial β -plane. The problem consists of a partial differential equation in the independent variables (y, z, t) , with appropriate boundary and initial conditions. This problem can be solved by a variety of methods. The methods used here are analytical and provide important insights into the dynamics. As described in Chapter 2, we first apply a vertical transform that converts the original partial differential equation in (y, z, t) into a system of partial differential equations in (y, t) for the horizontal structure of each vertical mode. As we will discuss in section 4.4, these partial differential equations are then solved analytically via a horizontal transform method.

As the vertical coordinate we use $z = H \ln(p_0/p)$, where $p_0 = 900$ hPa, $T_0 = 293$ K, and $H = RT_0/g = 8581$ m. We consider the case of weak horizontal flow and weak baroclinicity, so that the $v(\partial u/\partial y)$ and $w(\partial u/\partial z)$ terms in the zonal momentum equation, the $v(\partial v/\partial y)$ and

$w(\partial v/\partial z)$ terms in the meridional momentum equation, and the $v(\partial T/\partial y)$ term in the thermodynamic equation can be neglected. Under these assumptions, the governing equations are

$$\frac{\partial u}{\partial t} - \beta y v = 0, \quad (4.1)$$

$$\frac{\partial v}{\partial t} + \beta y u + \frac{\partial \Phi}{\partial y} = 0, \quad (4.2)$$

$$\frac{\partial \Phi}{\partial z} = \frac{g}{T_0} T, \quad (4.3)$$

$$\frac{\partial v}{\partial y} + \frac{\partial w}{\partial z} - \frac{w}{H} = 0, \quad (4.4)$$

$$\frac{\partial T}{\partial t} + \frac{T_0}{g} N^2 w = \frac{Q}{c_p}, \quad (4.5)$$

where u and v are the zonal and meridional components of velocity, w is the log-pressure vertical velocity, Φ is the perturbation geopotential, T is the perturbation temperature, N^2 is the square of the buoyancy frequency (considered for simplicity to be a constant), Q is the diabatic heating, and βy is the Coriolis parameter, with $\beta = 2\Omega/a$ denoting the constant northward gradient of the Coriolis parameter and with Ω and a denoting the Earth's rotation rate and radius. We have already formally derived the second order partial differential equation in (y, t) for the streamfunction $\psi_m(y, t)$ in Chapter 2, therefore we will begin from (2.28)–(2.32), which are restated below in a slightly different form as

$$\frac{\partial^2 \hat{\psi}_m}{\partial t^2} - gh_m \left(\frac{\partial^2}{\partial y^2} - \frac{y^2}{b_m^4} \right) \hat{\psi}_m = -gh_m \frac{\partial F_m}{\partial y}, \quad (4.6)$$

with boundary conditions

$$\hat{\psi}_m(y, t) \rightarrow 0 \text{ as } y \rightarrow \pm\infty, \quad (4.7)$$

and with the initial conditions

$$\hat{\psi}_m = 0 \quad \text{and} \quad \frac{\partial \hat{\psi}_m}{\partial t} = 0 \quad \text{at} \quad t = 0, \quad (4.8)$$

where the equatorial Rossby length is defined by $\bar{b}_m = (c_m/\beta)^{1/2}$ and $c_m = gh_m$ are the gravity wave speeds. The spectra of equivalent depths h_m , equatorial Rossby lengths \bar{b}_m , and gravity wave speeds c_m for $m = 0, 1, 2, 3, 4$ are shown in Table 4.1. Note that this \bar{b}_m definition of Rossby length is convenient when working with Hermite polynomials $H_n(x)$ (or the meridional structure functions $\mathcal{H}_n^m(x)$), while the $b_m = \bar{b}_m/\sqrt{2}$ definition of Rossby length is convenient when working with parabolic cylinder functions $D_n(x)$, as in Gonzalez and Mora Rojas (2014). This situation ruppert@atmos.colostate.edu Show details

arises because the two functions are related by $D_n(x\sqrt{2}) = 2^{-n/2}e^{-x^2/2}H_n(x)$. The forcing term $F_m(y, t)$ on the right hand side of equation (4.6) is given by

$$F_m(y, t) = \frac{g\hat{Q}_m(y, t)}{c_p T_0 N^2} + \left(\mathcal{W}(y, t) - \frac{g\hat{Q}(y, 0, t)}{c_p T_0 N^2} \right) \mathcal{Z}_m(0), \quad (4.9)$$

where

$$\hat{Q}_m(y, t) = \frac{N^2}{g} \int_0^{z_T} \hat{Q}(y, z, t) \mathcal{Z}_m(z) dz + \hat{Q}(y, 0, t) \mathcal{Z}_m(0). \quad (4.10)$$

TABLE 4.1. The spectra of equivalent depths h_m , gravity wave speeds $c_m = (gh_m)^{1/2}$, and Rossby lengths $b_m = (c_m/\beta)^{1/2}$ for the five values of m listed in the left column. The values have been computed from using $z_T = 13$ km, $g = 9.8$ m s⁻², $N = 1.2 \times 10^{-2}$ s⁻¹, and $H = 8581$ m.

m	h_m (m)	c_m (m s ⁻¹)	b_m (km)
0	7099	263.8	3394
1	229.8	47.46	1440
2	61.42	24.53	1035
3	27.66	16.46	848.1
4	15.63	12.38	735.2

4.4. SOLUTION VIA HERMITE TRANSFORMS

The solution of equations (4.6)–(4.8) is now constructed by using Hermite transform methods.

The Hermite transform pair for the streamfunction is

$$\hat{\psi}_m(y, t) = \sum_{n=0}^{\infty} \hat{\psi}_{mn}(t) \mathcal{H}_n^m(y), \quad (4.11)$$

$$\hat{\psi}_{mn}(t) = \frac{1}{\bar{b}_m} \int_{-\infty}^{\infty} \hat{\psi}_m(y, t) \mathcal{H}_n^m(y) dy, \quad (4.12)$$

where the meridional structure functions $\mathcal{H}_n^m(y)$ are related to the Hermite polynomials $H_n(y/\bar{b}_m)$

by

$$\mathcal{H}_n^m(y) = \left(\pi^{\frac{1}{2}} 2^n n! \right)^{-\frac{1}{2}} H_n(y/\bar{b}_m) e^{-\frac{1}{2}(y/\bar{b}_m)^2}. \quad (4.13)$$

Since the Hermite polynomials satisfy the recurrence relation $H_{n+1}(x) = 2xH_n(x) - 2nH_{n-1}(x)$,

it is easily shown that the meridional structure functions $\mathcal{H}_n^m(y)$ satisfy the recurrence relation

$$\mathcal{H}_{n+1}^m(y) = \left(\frac{2}{n+1} \right)^{\frac{1}{2}} \left(\frac{y}{\bar{b}_m} \right) \mathcal{H}_n^m(y) - \left(\frac{n}{n+1} \right)^{\frac{1}{2}} \mathcal{H}_{n-1}^m(y). \quad (4.14)$$

Since the first Hermite polynomial is $H_0(x) = 1$, the first meridional structure function is $\mathcal{H}_0^m(y) = \pi^{-\frac{1}{4}} e^{-\frac{1}{2}(y/\bar{b}_m)^2}$, from which all succeeding structure functions can be computed using the recur-

rence relation (4.14), with the understanding that the last term in (4.14) vanishes when $n = 0$.

Computing $\mathcal{H}_n^m(y)$ via its recurrence relation is much preferable to computing $H_n(y/\bar{b}_m)$ via its recurrence relation and then computing $\mathcal{H}_n^m(y)$ by evaluation of the right hand side of equation

(4.13), because the former method avoids explicit calculation of the factor $2^n n!$ for large n . Plots of $\mathcal{H}_n^m(y)$ for $m = 0, 1, 2$ and $n = 0, 1, 2, 3, 4$ are shown below in the three panels of Figure 4.3.

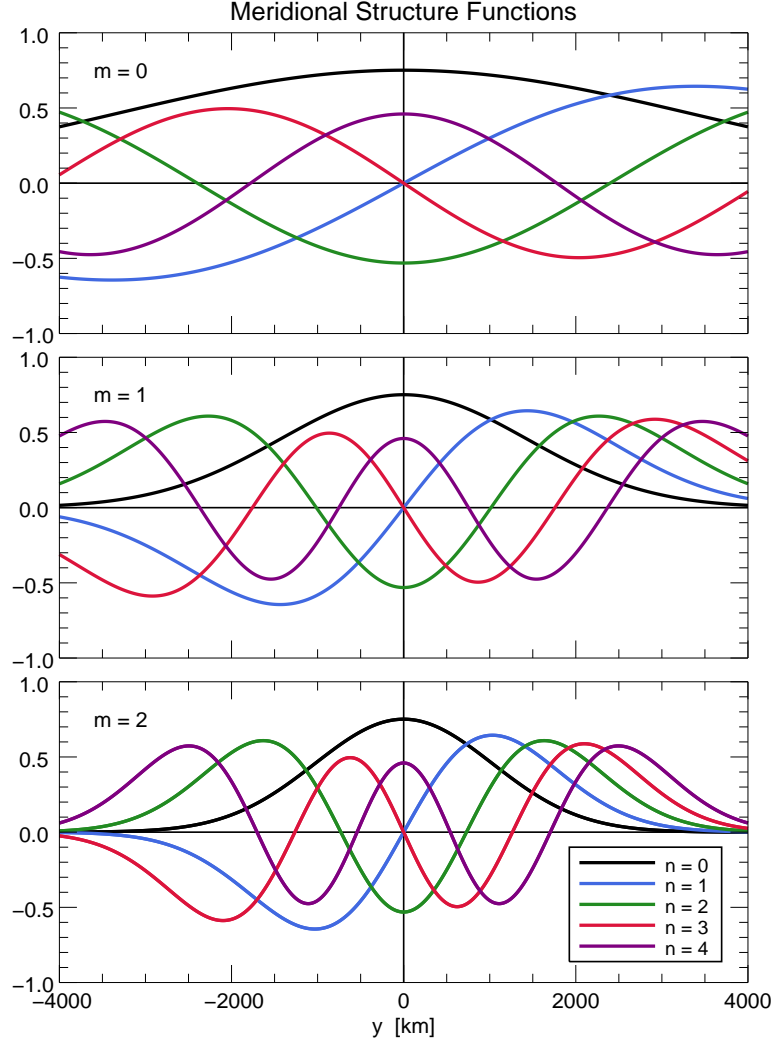


FIG. 4.3. Plots of $\mathcal{H}_n(y/\bar{b}_m)$ for $m = 0, 1, 2$ and $n = 0, 1, 2, 3, 4$. Note that, as n increases (for given m), the width of the oscillatory region of $\mathcal{H}_n(y/\bar{b}_m)$ increases as $n^{1/2}$, so the magnitude of $\mathcal{H}_n(y/\bar{b}_m)$ in the oscillatory region decreases as $n^{-1/4}$ in order to satisfy the normalization imposed by (4.16).

The meridional structure functions satisfy the second order equation

$$\left(\frac{d^2}{dy^2} - \frac{y^2}{\bar{b}_m^4} \right) \mathcal{H}_n^m(y) = - \left(\frac{2n+1}{\bar{b}_m^2} \right) \mathcal{H}_n^m(y), \quad (4.15)$$

so that $\mathcal{H}_n^m(y)$ is an eigenfunction of the operator that appears in parentheses on the left hand side of equation (4.6). This eigenfunction property makes the transform pair (4.11) and (4.12) convenient for the solution of (4.6). Note that solutions of (4.15) transition from oscillatory to evanescent

when $\tilde{y}_{mn} = \pm \bar{b}_m(2n + 1)^{1/2}$, which we denote as the turning (or critical) latitudes (Wunsch and Gill 1976). These will become important when we analyze the solutions for the streamfunction later. Another convenient property of the meridional structure functions $\mathcal{H}_n^m(y)$ is that they satisfy the orthonormality relation

$$\int_{-\infty}^{\infty} \mathcal{H}_n^m(y) \mathcal{H}_{n'}^m(y) dy = \begin{cases} \bar{b}_m & n' = n, \\ 0 & n' \neq n. \end{cases} \quad (4.16)$$

Note that equation (4.12) can be obtained through multiplication of equation (4.11) by $\mathcal{H}_{n'}^m(y)$, followed by integration over y and use of equation (4.16).

To take the meridional transform of equation (4.6), first multiply it by $\mathcal{H}_n^m(y)$ and integrate over y . The integral originating from the second order y -derivative term in equation (4.6) is then integrated by parts twice, making use of the boundary conditions (4.8), to yield

$$\begin{aligned} & \frac{\partial^2}{\partial t^2} \int_{-\infty}^{\infty} \hat{\psi}_m(y, t) \mathcal{H}_n^m(y) dy \\ & - gh_m \int_{-\infty}^{\infty} \hat{\psi}_m(y, t) \left(\frac{d^2}{dy^2} - \frac{y^2}{\bar{b}_m^4} \right) \mathcal{H}_n^m(y) dy \\ & = -gh_m \int_{-\infty}^{\infty} \frac{\partial F_m(y, t)}{\partial y} \mathcal{H}_n^m(y) dy. \end{aligned} \quad (4.17)$$

To simplify equation (4.17) we first use equation (4.15) in the integrand on the second line. We then make use of equation (4.12) to simplify equation (4.17) to the second order ordinary differential equation

$$\frac{d^2 \hat{\psi}_{mn}}{dt^2} + \nu_{mn}^2 \hat{\psi}_{mn} = -gh_m F'_{mn}, \quad (4.18)$$

with the initial conditions

$$\hat{\psi}_{mn} = 0 \text{ and } \frac{d\hat{\psi}_{mn}}{dt} = 0 \text{ at } t = 0, \quad (4.19)$$

where the inertia-gravity wave frequency ν_{mn} is given by

$$\nu_{mn} = \frac{1}{\bar{b}_m} [gh_m (2n + 1)]^{1/2}, \quad (4.20)$$

and the forcing by

$$F'_{mn}(t) = \frac{1}{\bar{b}_m} \int_{-\infty}^{\infty} \frac{\partial F_m(y, t)}{\partial y} \mathcal{H}_n^m(y) dy. \quad (4.21)$$

The inertia-gravity wave frequencies for the first 5 vertical wavenumbers ($m = 0, 1, 2, 3, 4$) are shown as a function of meridional mode n in Figure 4.4 below. Values of the switch-on function $\mathcal{T}(t)$, which will be formally introduced in the next section, are plotted in the four horizontal dotted lines, $\gamma^{-1} = 3, 6, 12, 24$ hours. Notice how $\gamma^{-1} = 24$ h does not intersect with any of the $m = 0, 1, 2, 3, 4$ inertia-gravity wave frequencies. As will be seen later, when diabatic heating is switched on at this rate, inertia-gravity wave activity is minimal, and the transient solutions are approximately equal to the balanced solutions derived in Chapter 2. In the next section we solve (4.18) and (4.19) for a particular forcing.

4.5. TRANSIENT HADLEY CIRCULATIONS FORCED BY A SWITCH-ON OF ITCZ CONVECTION

For illustration purposes, we now consider the response to a forcing for which the Ekman pumping and the diabatic heating at $z = 0$ are related by

$$\mathcal{W}(y, t) = \frac{g\hat{Q}(y, 0, t)}{c_p T_0 N^2}, \quad (4.22)$$

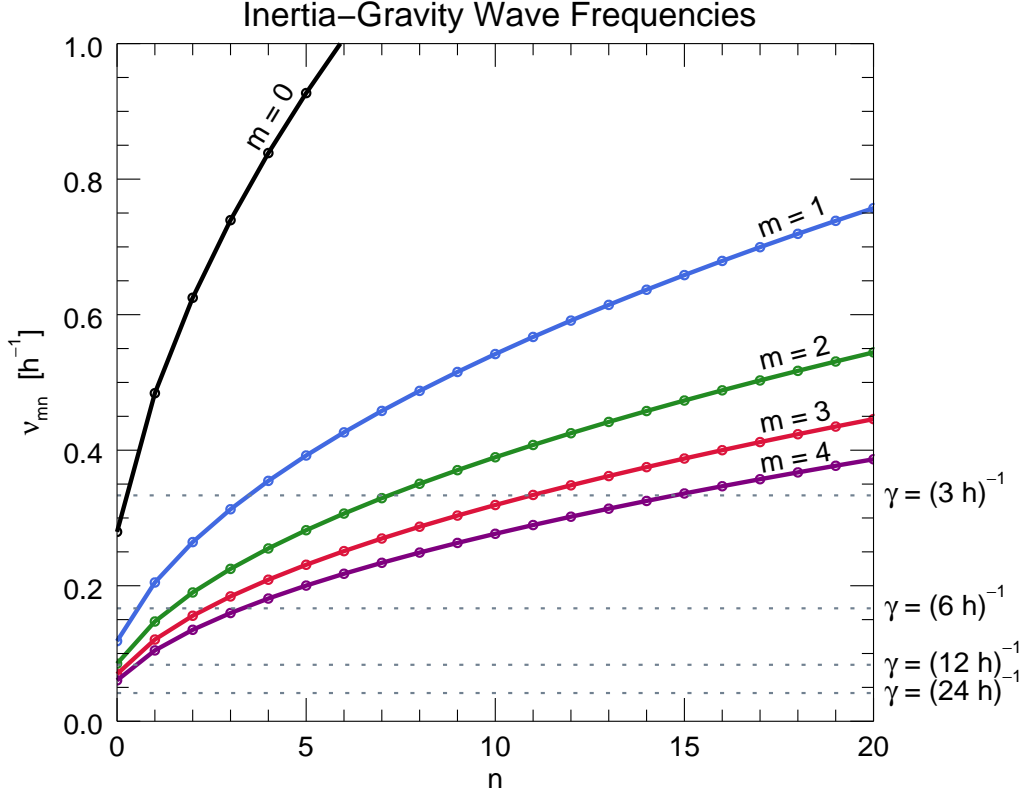


FIG. 4.4. Plots of ν_{mn} , computed from equation (4.20), for $m = 0, 1, 2, 3, 4$ and $n = 0, 1, \dots, 20$. The four horizontal dotted lines indicate the values of γ corresponding to the four switch-on functions $\mathcal{T}(t)$ plotted in Figure 4.5.

so that (4.9) simplifies to

$$F_m(y, t) = \frac{g\hat{Q}_m(y, t)}{c_p T_0 N^2}. \quad (4.23)$$

Assume that $\hat{Q}(y, z, t)$ vanishes everywhere except in the latitudinal range $y_1 < y < y_2$, where y_1 and y_2 are constants that specify the south and north boundaries of the ITCZ. Within this ITCZ region the diabatic heating is assumed to be independent of y and to be smoothly switched on to a steady state value, i.e.,

$$\hat{Q}(y, z, t) = \mathcal{T}(t) \begin{cases} \sum_{m=0}^{\infty} \tilde{Q}_m \mathcal{Z}_m(z) & \text{if } y_1 < y < y_2, \\ 0 & \text{otherwise,} \end{cases} \quad (4.24)$$

where the constants \tilde{Q}_m specify the projection of the vertical structure of $\hat{Q}(y, z, t)$ onto the vertical modes, and where the time dependence is given by

$$\mathcal{T}(t) = 1 - (1 + \gamma t)e^{-\gamma t}, \quad (4.25)$$

with the constant γ specifying the sharpness of the switch-on function $\mathcal{T}(t)$. Figure 4.5 displays four $\mathcal{T}(t)$ curves for the particular values $\gamma^{-1} = 3, 6, 12, 24$ hours.

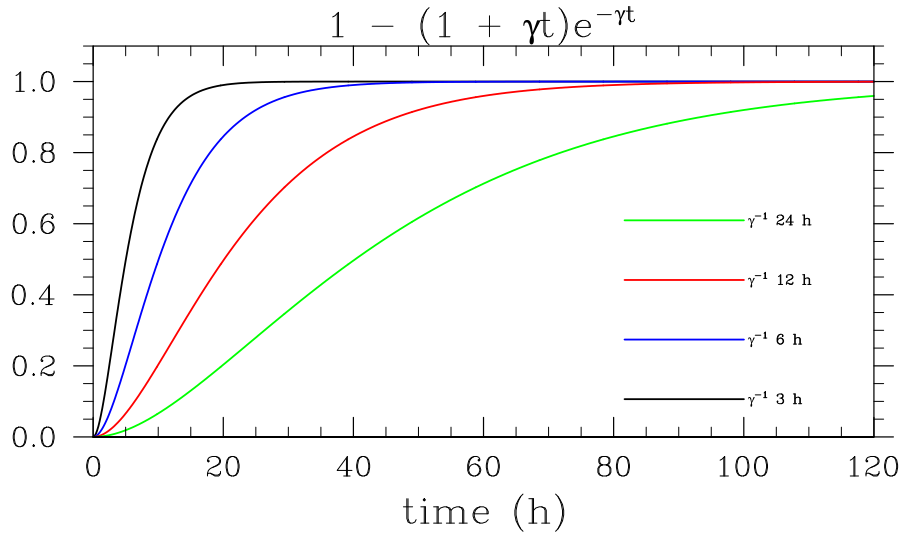


FIG. 4.5. Plots of the switch-on function $\mathcal{T}(t)$ for the four choices $\gamma^{-1} = 3, 6, 12, 24$ hours. The “filtered solutions” discussed below are valid for the “slow switch-on” cases, i.e., for large values of γ^{-1} .

Substituting (4.24) into (4.9), and then using the orthonormality relation (A.2), we obtain

$$\hat{Q}_m(y, t) = \mathcal{T}(t) \begin{cases} \tilde{Q}_m & \text{if } y_1 < y < y_2, \\ 0 & \text{otherwise.} \end{cases} \quad (4.26)$$

Use of (4.23) and (4.26) in (4.21) now yields

$$F'_{mn}(t) = \frac{g\mathcal{H}_n^m(y_1)}{c_p T_0 N^2 \bar{b}_m} \int_{y_1^-}^{y_1^+} \frac{\partial \hat{Q}_m(y, t)}{\partial y} dy + \frac{g\mathcal{H}_n^m(y_2)}{c_p T_0 N^2 \bar{b}_m} \int_{y_2^-}^{y_2^+} \frac{\partial \hat{Q}_m(y, t)}{\partial y} dy = \mathcal{T}(t) \mathcal{F}_{mn}, \quad (4.27)$$

where

$$\mathcal{F}_{mn} = \frac{g\tilde{Q}_m}{c_p T_0 N^2 \bar{b}_m} [\mathcal{H}_n^m(y_1) - \mathcal{H}_n^m(y_2)], \quad (4.28)$$

and where we have made use of the fact that the narrow integral of $(\partial\hat{Q}_m/\partial y)$ across y_1 is $\tilde{Q}_m\mathcal{T}(t)$, while the narrow integral across y_2 is $-\tilde{Q}_m\mathcal{T}(t)$.

The final equality in (4.27) can now be used in the right hand side of equation (4.18), and the complete solution can be written as the sum of the homogeneous solution and a particular solution. As is easily checked by direct substitution into equation (4.18), the solution satisfying the initial conditions (4.19) is

$$\begin{aligned} \hat{\psi}_{mn}(t) = & -\frac{gh_m\mathcal{F}_{mn}}{\nu_{mn}^2} \left\{ \left(\frac{(\nu_{mn}^2 - \gamma^2)\gamma^2}{(\nu_{mn}^2 + \gamma^2)^2} \right) \cos(\nu_{mn}t) - \left(\frac{2\gamma^3\nu_{mn}}{(\nu_{mn}^2 + \gamma^2)^2} \right) \sin(\nu_{mn}t) \right. \\ & \left. + 1 - \left(\frac{\nu_{mn}^2 + 3\gamma^2}{\nu_{mn}^2 + \gamma^2} + \gamma t \right) \left(\frac{\nu_{mn}^2 e^{-\gamma t}}{\nu_{mn}^2 + \gamma^2} \right) \right\}. \end{aligned} \quad (4.29)$$

In summary, the solution of the original meridional circulation problem (2.10)–(2.14) is obtained by combining equations (2.15), (2.21), and (4.11) into

$$\psi(y, z, t) = e^{-z/2H} \sum_{m=0}^{\infty} \sum_{n=0}^{\infty} \hat{\psi}_{mn}(t) \mathcal{H}_n^m(y) \mathcal{Z}_m(z), \quad (4.30)$$

where $\hat{\psi}_{mn}(t)$ is given by equation (4.29). Plots of the streamfunction can be constructed by first calculating \mathcal{F}_{mn} from equation (4.28), then calculating $\hat{\psi}_{mn}(t)$ from equation (4.29), and finally calculating $\psi(y, z, t)$ from equation (4.30).

Note that when $\gamma \ll \nu_{mn}$, the solution (4.29) simplifies considerably since the coefficients of the $\cos(\nu_{mn}t)$ and $\sin(\nu_{mn}t)$ terms become much smaller than unity, while the third line in equation

(4.29) approaches $\mathcal{T}(t)$. Then, the spectral space solution (4.29) simplifies to

$$\hat{\psi}_{mn}^{(b)}(t) = -\frac{gh_m \mathcal{F}_{mn} \mathcal{T}(t)}{\nu_{mn}^2}, \quad (4.31)$$

so that the physical space solution (4.30) becomes

$$\psi^{(b)}(y, z, t) = e^{-z/2H} \sum_{m=0}^{\infty} \sum_{n=0}^{\infty} \hat{\psi}_{mn}^{(b)}(t) \mathcal{H}_n^m(y) \mathcal{Z}_m(z), \quad (4.32)$$

where the superscript (b) indicates the balanced (or filtered) solution. Since the time dependence on the right hand side of (4.31) is $\mathcal{T}(t)$, the $\psi^{(b)}(y, z, t)$ field develops in lockstep with the forcing, i.e., there is no time delay between the forcing and the response, no matter how far one is from the forcing. Since this represents “action at a distance,” it should be regarded as a filtered approximation of the actual dynamics, valid only in the case of a “slowly varying forcing.” To better understand how slow the forcing needs to be, Fig. 4.4 includes horizontal dotted lines for the four values of γ used in Fig. 4.5. As an example, for $m = 1$ and $\gamma = (24 \text{ h})^{-1}$ the condition $\gamma \ll \nu_{mn}$ holds for essentially all n , while for $m = 1$ and $\gamma = (1 \text{ h})^{-1}$ the condition does not hold for the smaller values of n . Thus, for $m = 1$ and the slow $\gamma = (24 \text{ h})^{-1}$ forcing, inertia-gravity wave activity should be weak and the balanced (or filtered) solution (4.32) should be accurate. This argument will be confirmed by the examples shown in section 4.6.

4.6. EXAMPLES USING $m = 0, 1, 2$ DIABATIC HEATING

For simplicity, we assume

$$\frac{\tilde{Q}_m}{c_p} = \begin{cases} (5 \text{ K day}^{-1}) \left(\frac{500 \text{ km}}{y_2 - y_1} \right) & \text{if } m = 1, \\ 0 & \text{if } m \neq 1, \end{cases} \quad (4.33)$$

i.e., the diabatic heating projects only onto the first internal mode and has been normalized in such a way that the horizontally integrated forcing $(y_2 - y_1)\tilde{Q}_m$ is fixed.

Thus, for the external mode and the first two internal modes, the $\gamma^{-1} = 24$ h curve in Figure 4.4 yields a forcing that is probably slow enough for the filtered approximation to be reasonably accurate, but the $\gamma^{-1} = 3$ h curve yields a forcing that excites a non-negligible inertia-gravity wave response, especially for the higher internal modes, as we will see in the next few figures.

Figure 4.6 shows isolines of $\psi(y, z, t)$ and contour shading of $Q(y, z)e^{-z/H}/c_p$ at $t = 32$ h, 56 h, 80 h, and 104 h computed from equation (4.30) using the parameters $z_T = 13$ km, $N = 1.2 \times 10^{-2} \text{ s}^{-1}$, $(y_1, y_2) = (1000, 1500)$ km, and $\gamma^{-1} = 3$ h. Note that the largest asymmetries between the winter hemisphere Hadley cell and the summer hemisphere Hadley cell occur for this ITCZ displacement due to the anisotropy of the inertial stability, as discussed in Chapter 2. Also note that the forcing has been sufficiently switched on by $t = 32$ h according to Fig. 4.5. The summer cell is almost nonexistent at $t = 32$ h, then there are very small asymmetries between the winter and summer cells at $t = 56$ h, and then about a 9:1 asymmetry at $t = 80$ h, and once again almost no asymmetry at $t = 104$ h. Also note the expansion and contraction of both winter and summer cells at $t = 32$ h and $t = 56$ h, respectively. These features, suggest that there is significant transient activity due to inertia-gravity waves in both the Hadley cells. Another way to view the transient activity in both the winter and summer Hadley cells is illustrated in Figure 4.7. We compute the normalized total streamfunction ψ and fractional streamfunction ψ as a function of time and the power spectrum as a function of frequency using the parameters $z_T = 13$ km, $N = 1.2 \times 10^{-2} \text{ s}^{-1}$, $(y_1, y_2) = (1000, 1500)$ km, and $\gamma^{-1} = 3$ h, shown in the three panels in Figure 4.7. The total ψ is the sum of the maximum values of ψ at the northern and southern edges of the ITCZ. It is then normalized using the maximum total ψ for all times. The fractional ψ is the the

ITCZ = (1000,1500) km, $\gamma^{-1} = 3$ h

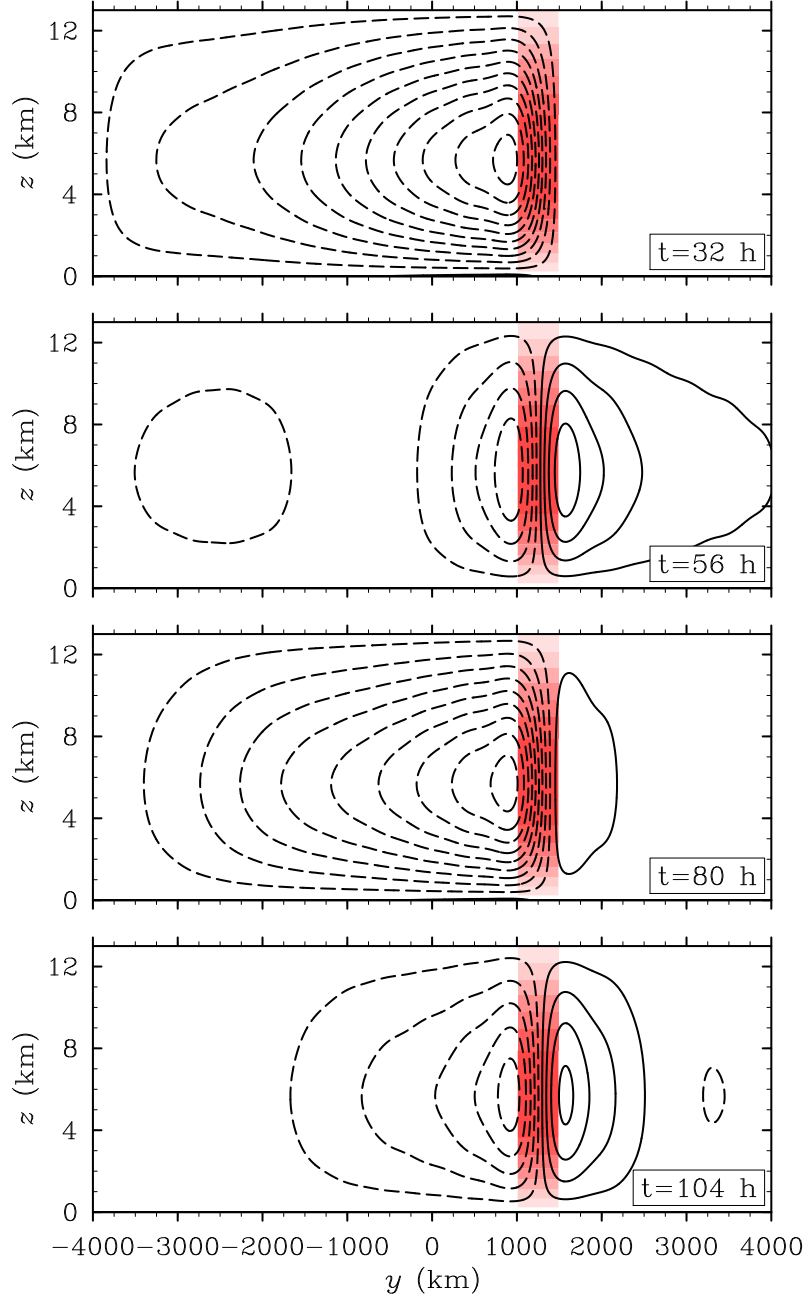


FIG. 4.6. Contoured streamfunction $\psi(y, z)$ and shaded $Q(y, z)e^{-z/H}/c_p$ fields for $(y_1, y_2) = (1000, 1500)$ km and $\gamma^{-1} = 3$ h at $t = 32$ h, 56 h, 80 h, and 104 h. The contour interval for $\psi(y, z)$ is $400 \text{ m}^2 \text{ s}^{-1}$, the maximum (magnitude) of $\psi(y, z)$ is $4149 \text{ m}^2 \text{ s}^{-1}$, and the zero line is omitted. The $Q(y, z)e^{-z/H}/c_p$ shade interval is 0.5 K day^{-1} , and the maximum (magnitude) of the diabatic heating is 3.496 K day^{-1} .

fraction of the winter (blue) or summer (red) cell ψ divided by the total ψ . The power spectrum is computed in both the winter (blue) and summer (red) cell using the solutions of ψ from $t = 0$ –360 h using the NCL function `specx_anal`, using 10 % tapering and no smoothing. We also normalize the energy density by dividing by the maximum energy density in either the winter or summer cell.

The temporal evolution of the normalized total streamfunction ψ , shown in the top panel of Fig. 4.7, shows the highly variable nature of the how much mass is being fluxed away from the ITCZ and into the extratropics. When air rises to the tropopause in the ITCZ, it has the option of turning toward or away from the equator (into the winter or summer cell, respectively). In Chapter 2, we found out that it is easier for the air to turn toward the equator due to the smaller inertial stability near the equator. When the ITCZ is in a balanced state, as illustrated in the solutions in Chapter 2, this rising ITCZ air turns toward the equator about twice as often than it turns away from the equator. The fractional streamfunction ψ in the middle panel of Fig. 4.7 illustrates that when the ITCZ is time dependent, the behavior of the rising air in the ITCZ is more complicated. The asymmetry between the winter and summer cells fluctuates so much so that the winter cell at times is weaker than the summer cell, e.g., $t \approx 60$ h, and at other times, e.g., $t \approx 195$ h, the summer cell is almost nonexistent. However, the average winter to summer cell asymmetry over time is about 2:1, shown in the dashed lines in Fig. 4.7, and is similar to the balanced results shown in Figure 2.15. The period of the pulsations is a bit irregular, but in general is on the order of two days (51.5 h), as shown in the power spectrum in the bottom panel of Figure 4.7. Also note that the winter cell has a larger normalized energy density than the summer cell, suggesting that there is more inertia-gravity wave activity in the winter cell.

We have also produced plots using the same parameters as those used to produce Fig. 4.7 except $\gamma^{-1} = 6, 12, \text{ and } 24$ h. The inertia-gravity activity decreases as γ^{-1} increases, but the most

ITCZ = (1000,1500) km, $m = 1$, $\gamma^{-1} = 3$ h

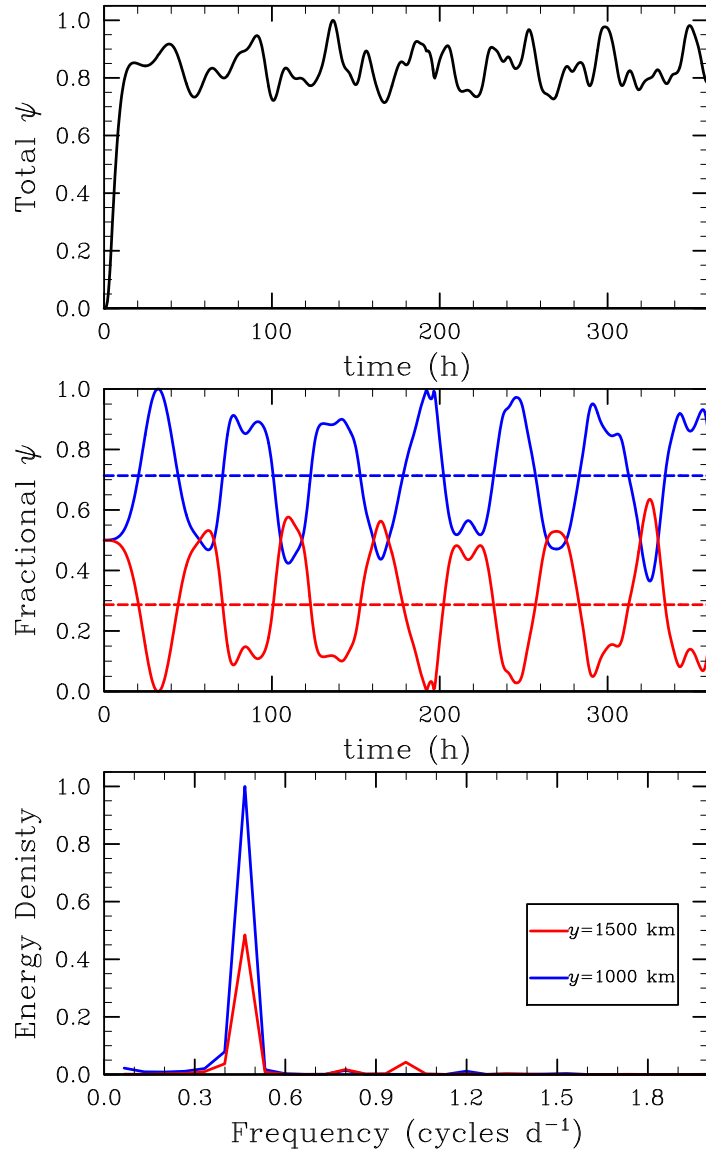


FIG. 4.7. The top panel illustrates the total streamfunction ψ as a function of time computed by summing ψ for the winter and summer Hadley cells and normalizing it by the maximum total ψ . The middle panel shows the fractional ψ of the winter (summer) Hadley cell in blue (red) as a function of time in the solid lines, and their time average fractional ψ in the dashed lines. The normalized energy density as a function of frequency is shown in the bottom panel for the winter (blue) and summer (red) Hadley cell. The $m = 1$ diabatic heating is located between 1000 and 1500 km and $\gamma^{-1} = 3$ h.

prominent spectral peak in both Hadley cells is still at the two-day timescale (51.5 h) for $\gamma^{-1} = 6$ and 12 h. Therefore, we choose not to show the plots corresponding to the $\gamma^{-1} = 6$ and 12 h

cases. Figure 4.8 illustrates the normalized total streamfunction ψ and fractional streamfunction ψ as a function of time and the power spectrum as a function of frequency using the parameters as those used to produce Fig. 4.7 except $\gamma^{-1} = 24$ h. Note from the top panel of Fig. 4.8 that as γ^{-1} increases, the fluctuations in the total mass flux and the fractional mass flux in the winter and summer Hadley cells decrease. As can be seen in the power spectrum in the bottom panel of Fig. 4.8, the energy density associated with two day oscillations is much smaller than that of the lowest frequencies, and the winter cell is significantly stronger than the summer cell. The asymmetry between the winter and summer cells oscillates between 2:1 to 3:1, illustrating the sensitivity of the Hadley cells to how fast convection in the ITCZ is turned on. There are still inertia-gravity waves, but $\gamma \ll \nu_{mn}$, and the solution (4.29) approaches the balanced solution (4.32). Once again, the average winter to summer cell asymmetry over time is about 2:1 (dashed lines of middle panel), similar to the $m = 1$ balanced results shown in Figure 2.15.

The spectral space solution (4.29) can be considered to be the sum of two parts, with the first part consisting of the oscillatory terms $\cos(\nu_{mn}t)$ and $\sin(\nu_{mn}t)$ and the second part consisting of the decaying term with the $e^{-\gamma t}$ factor. There is a third term which is outside of the brackets, which is the steady state term, $-gh_m F'_{mn}/\nu_{mn}^2$. For large times (i.e., $\gamma t \gg 1$), the second part is negligible and the oscillatory terms represent inertia-gravity waves that have propagated far from any confined region of forcing (Salby and Garcia 1987; Garcia et al. 1987).

Figure 4.9 shows the total ψ solution at $z \approx 6$ km, the oscillatory (or inertia-gravity) part of ψ (igw), and the decaying (or balanced) part of ψ (bal) using the parameters $z_T = 13$ km, $N = 1.2 \times 10^{-2} \text{ s}^{-1}$, $(y_1, y_2) = (1000, 1500)$ km, and $\gamma^{-1} = 3$ h. Now we see that the balanced ψ solutions (bottom panel) change very little after about 10 hours while the inertia-gravity wave ψ solutions (middle panel) continue to be active long after the forcing has been sufficiently switched

ITCZ = (1000,1500) km, $m = 1$, $\gamma^{-1} = 24$ h

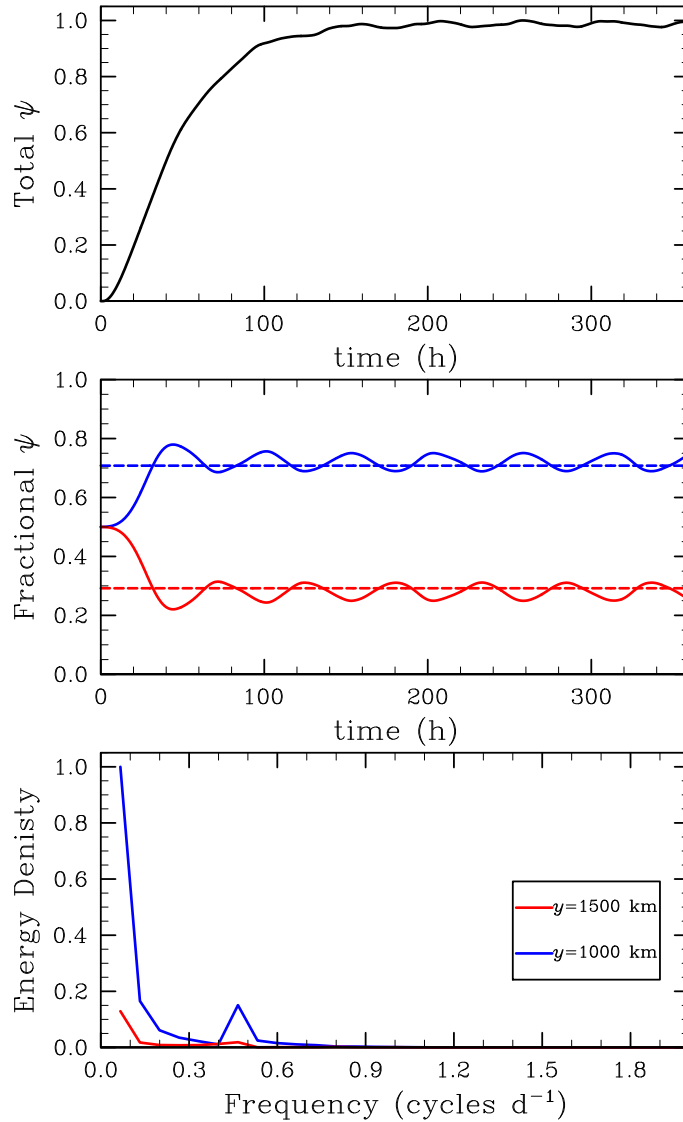


FIG. 4.8. The same as Fig. 4.7, but for $\gamma^{-1} = 24$ h.

on. This signifies the presence of equatorially-trapped inertia-gravity wave packets and the idea that the tropical atmosphere has memory of the initial forcing. It is interesting to note that the inertia-gravity wave activity is maximum just south of the ITCZ, in the winter cell. This result is in line with the fact that there is an inherent asymmetry between the winter and summer cells due to the anisotropy of the inertial stability. Also, the irregular behavior of the pulsating in the winter and summer cells is likely due to the idea that the waves are equatorially trapped and bounce off

the turning latitudes $\tilde{y}_{mn} = \pm \bar{b}_m(2n + 1)^{1/2}$, where the solutions of ψ transition from oscillatory to evanescent. The inertia-gravity waves initially travel away from the ITCZ in the north/south direction, and when the ITCZ is north of the equator, the waves that initially travel north reach their turning latitudes before those that initially travel south. This behavior likely causes the pulsations of the Hadley cells to be irregular. In Table 4.2, we display the turning latitudes for $m = 0, 1, 2, 3, 4$ and $n = 0, 1, 2, 3, 4$.

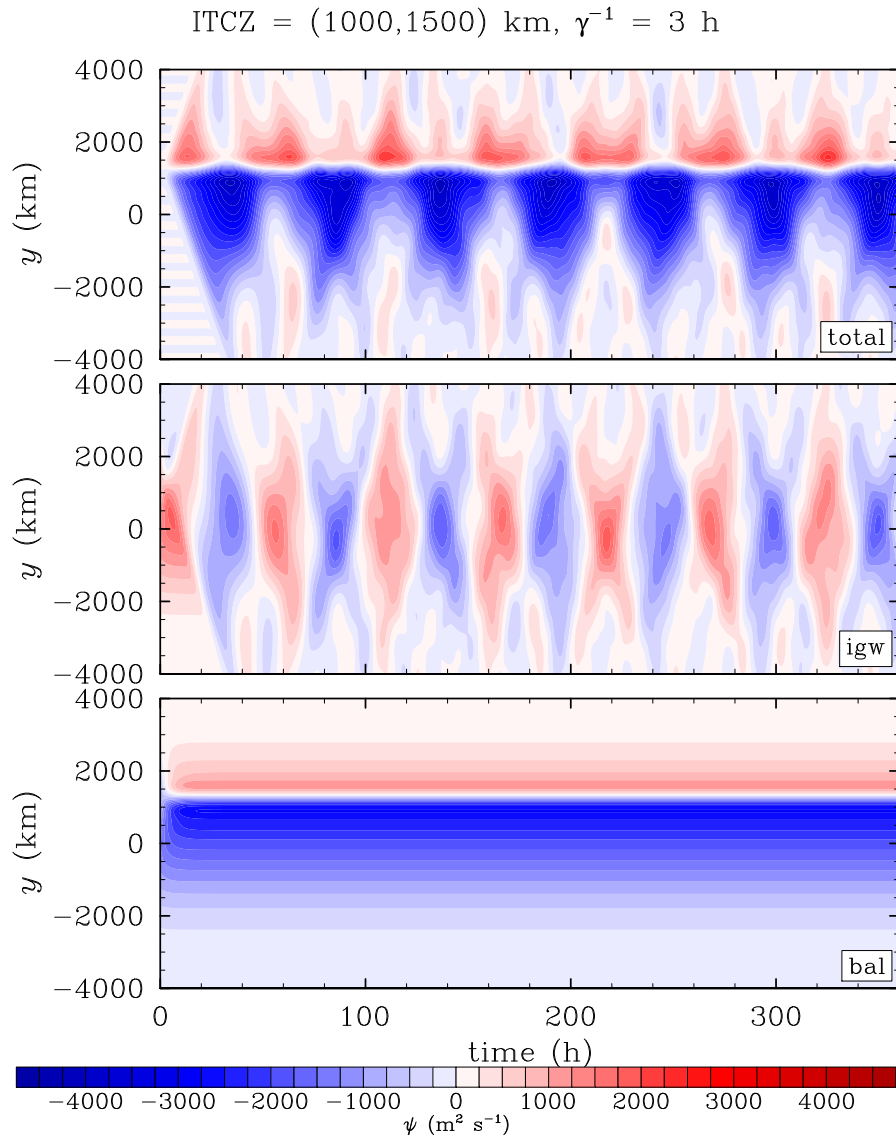


FIG. 4.9. Solutions of $\psi(y, t)$ in $\text{m}^2 \text{s}^{-1}$ at $z \approx 6$ km: the total ψ solution (total), the inertia-gravity part of ψ (igw), and the balanced part of ψ (bal) using the parameters $z_T = 13$ km, $N = 1.2 \times 10^{-2} \text{ s}^{-1}$, $(y_1, y_2) = (1000, 1500)$ km, and $\gamma^{-1} = 3$ h.

TABLE 4.2. The turning latitudes in units of km for $m = 0, 1, 2, 3, 4$ and $n = 0, 1, 2, 3, 4$ using the formula $\tilde{y}_{mn} = \pm \bar{b}_m (2n + 1)^{1/2}$. Note how the turning latitude increases as the meridional mode n increases and m decreases.

Turning Latitudes \tilde{y}_{mn} (km)					
m	$n = 0$	$n = 1$	$n = 2$	$n = 3$	$n = 4$
0	3395	5880	7590	8981	10184
1	1440	2494	3230	3809	4319
2	1035	1793	2315	2739	3106
3	848.1	1469	1896	2244	2544
4	735.3	1274	1644	1945	2206

Figure 4.10 shows the total ψ solution at $z \approx 6$ km, the oscillatory (or inertia-gravity) part of ψ (igw), and the decaying (or balanced) part of ψ (bal) using the parameters $z_T = 13$ km, $N = 1.2 \times 10^{-2} \text{ s}^{-1}$, $(y_1, y_2) = (1000, 1500)$ km, and $\gamma^{-1} = 24$ h. This figure helps confirm that inertia-gravity wave activity (middle panel) is limited and the total solutions (top panel) are approximately equal to the balanced solutions (bottom panel).

Thus far we have shown solutions for the streamfunction ψ , but we can easily illustrate the solutions for meridional v and log-pressure vertical velocity w using (2.9). We have chosen not to show v and w because the results are qualitatively the same as the results of ψ shown. However, an interesting feature of the w field is that the rising motion does not change as much in the ITCZ compared to the subsidence regions north and south of the ITCZ. This is due to the fact that the diabatic heating is invariant in the y direction in the ITCZ. We now performed experiments in which the vertical structure of the diabatic heating is solely of the $m = 0$ external mode and solely of the $m = 2$ internal mode. In Figures 4.11 and 4.12, we show the normalized total streamfunction ψ and fractional streamfunction ψ fields as a function of time using the parameters $z_T = 13$ km, $N = 1.2 \times 10^{-2} \text{ s}^{-1}$, $(y_1, y_2) = (1000, 1500)$ km, and $\gamma^{-1} = 3$ h for the $m = 2$ and $m = 0$ diabatic heating, respectively.

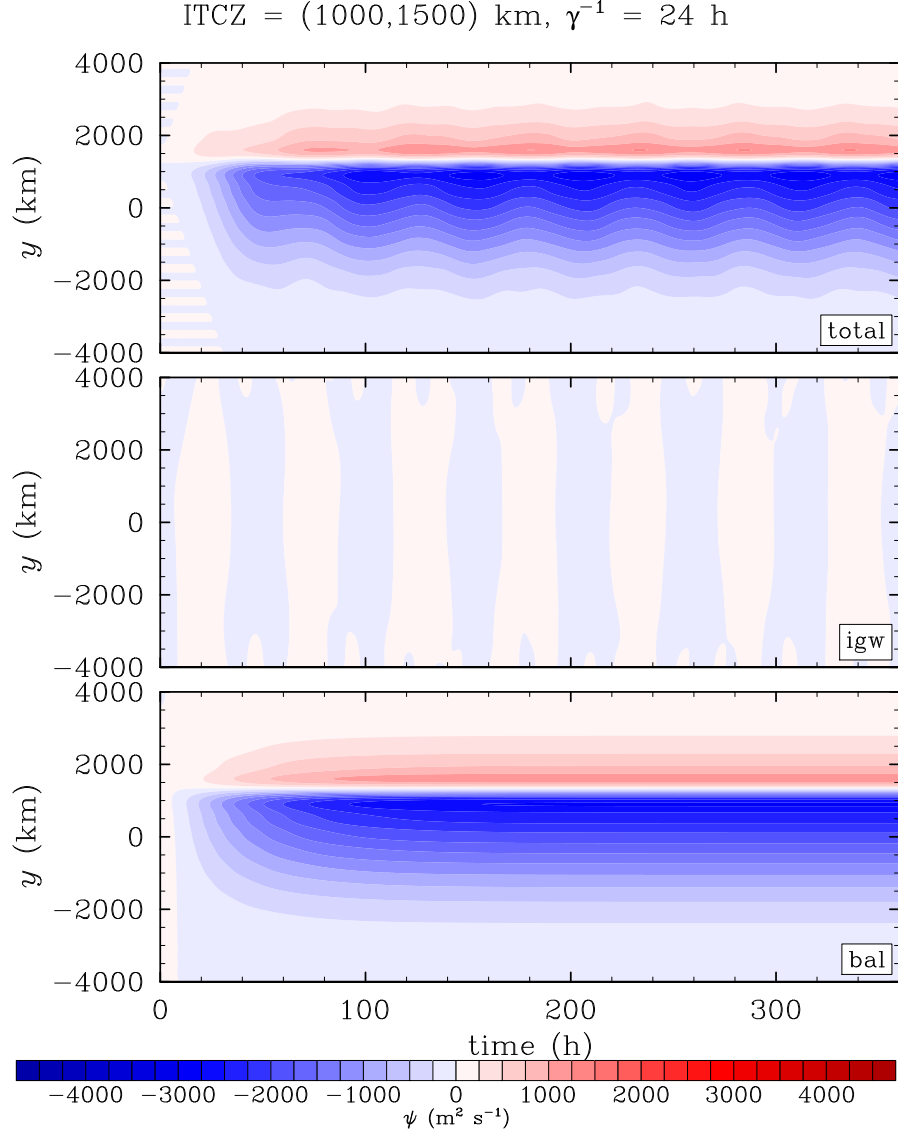


FIG. 4.10. Solutions of $\psi(y, t)$ in $\text{m}^2 \text{s}^{-1}$ at $z \approx 6$ km: the total ψ solution (total), the inertia-gravity part of ψ (igw), and the balanced part of ψ (bal) using the parameters $z_T = 13$ km, $N = 1.2 \times 10^{-2} \text{ s}^{-1}$, $(y_1, y_2) = (1000, 1500)$ km, and $\gamma^{-1} = 24$ h.

The ideas we have postulated thus far for the $m = 1$ diabatic forcing apply to the $m = 0$ and $m = 2$ cases in that there is significant pulsating of the winter and summer Hadley cells leading to oscillations in the total streamfunction. The pulsating for the $m = 2$ diabatic heating leads to slower inertia-gravity wave packets than the $m = 1$ case, with a period of about 3 days (72.1 h), while the pulsating for the $m = 0$ diabatic heating leads to faster inertia-gravity wave

ITCZ = (1000,1500) km, $m = 2$, $\gamma^{-1} = 3$ h

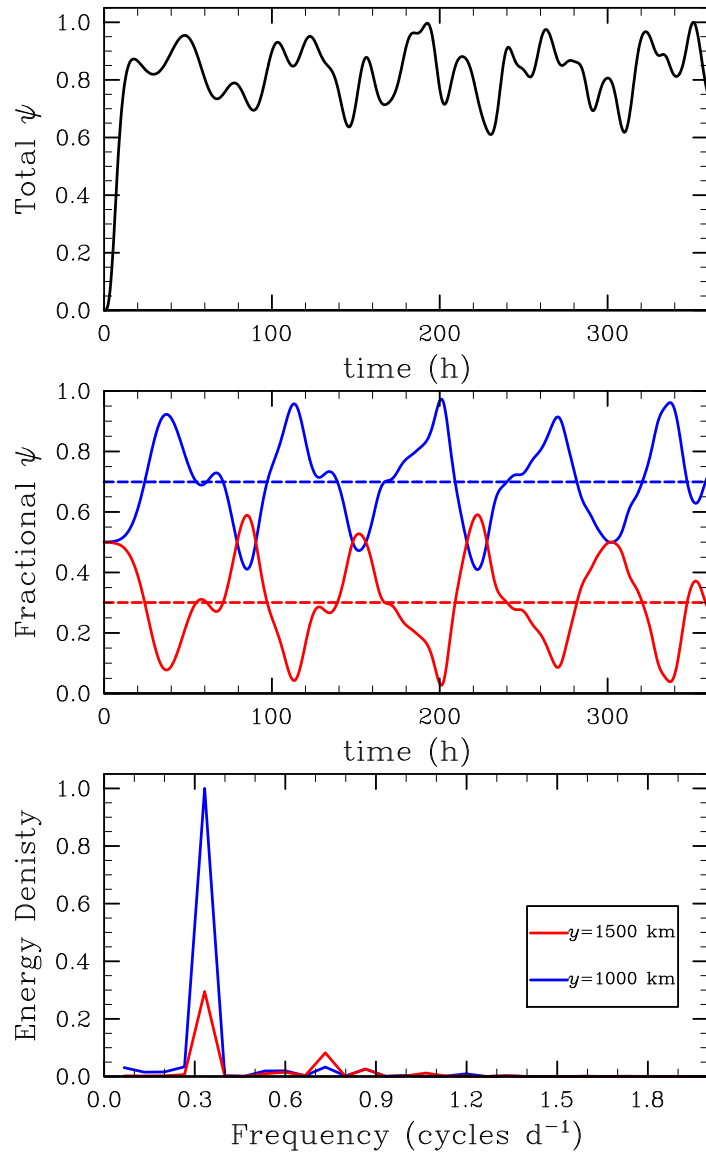


FIG. 4.11. The top panel illustrates the total streamfunction ψ as a function of time computed by summing ψ for the winter and summer Hadley cells and normalizing it by the maximum total ψ . The bottom panel shows the fractional ψ of the winter (summer) Hadley cell in blue (red) as a function of time. The normalized energy density as a function of frequency is shown in the bottom panel for the winter (blue) and summer (red) Hadley cell. The $m = 2$ diabatic heating is located between 1000 and 1500 km and $\gamma^{-1} = 3$ h.

packets than the $m = 1$ case, with a period of about 1 day (22.5 h). This result has to do with the fact that the internal gravity wave speed decreases as a function of vertical wavenumber m . Even though the turning latitude decreases as m increases, the decrease in gravity wave speed has

ITCZ = (1000,1500) km, $m = 0$, $\gamma^{-1} = 3$ h

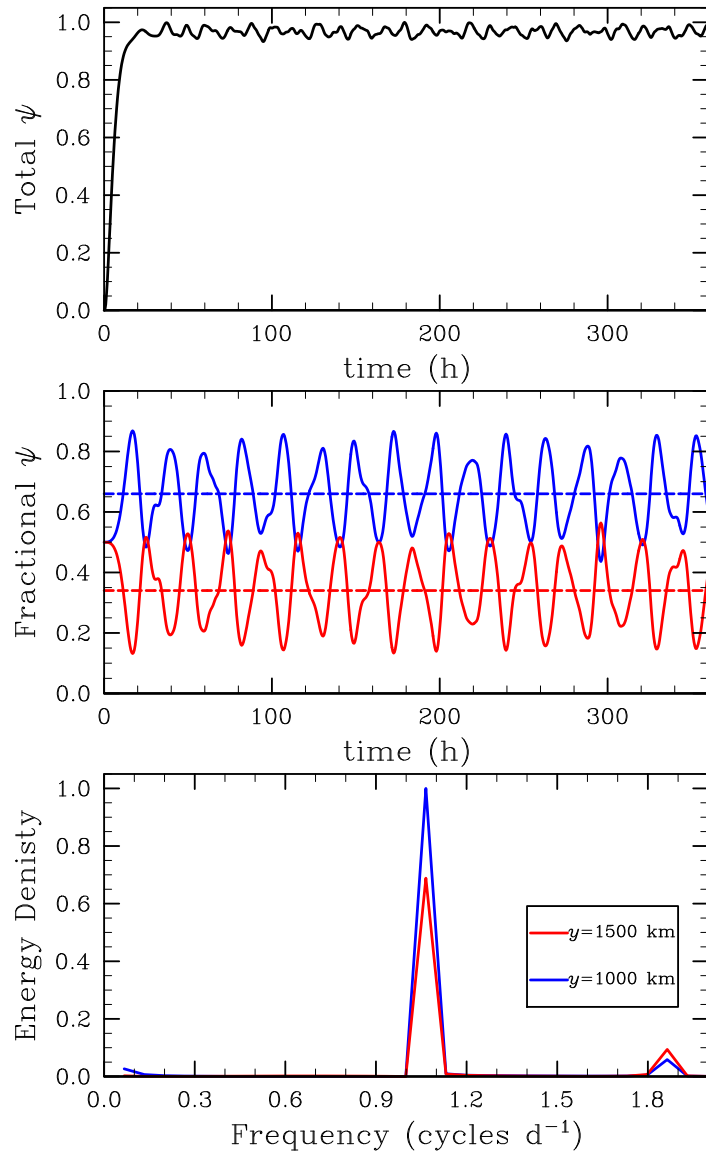


FIG. 4.12. The same as Fig. 11 for a $m = 0$ diabatic heating.

a larger effect on the wave packets. This implies that the wave packets take longer to reach their critical latitudes as the vertical structure of diabatic heating becomes more complex (e.g., higher internal modes), leading to a longer period of pulsating of the Hadley circulation. Another feature worth discussing is the total streamfunction plots on the top panels of Fig. 4.11 and 4.12. As m increases, the influence of the inertia-gravity waves on the total ψ increases. This is most evident in the $m = 0$ case, where the inertia-gravity waves seem to have less of an impact on the total ψ .

A possible explanation for this behavior has to do with the idea that as the forcing involves higher vertical wavenumbers, the asymmetry between the winter and summer cells increases, as discussed in Chapter 2.

In concluding this section it is interesting to note that, as t becomes large, $\mathcal{T}(t) \rightarrow 1$ and the forced divergent circulation (v, w) comes into steady state. However, as can be seen from (4.1) and (4.5), the zonal flow and the temperature continue to evolve. In fact, as discussed by Gonzalez and Mora Rojas (2014), these fields evolve in such a way that the associated potential vorticity field develops local extrema in the ITCZ, leading to a zonal flow that satisfies the Charney-Stern necessary condition for combined barotropic-baroclinic instability (Charney and Stern 1962). Thus, one should not expect the evolving zonal flow to remain zonally symmetric for more than approximately 10–15 days (Nieto Ferreira and Schubert 1997; Wang and Magnusdottir 2005; Magnusdottir and Wang 2008).

4.7. ANALYSIS OF THE INERTIA-GRAVITY WAVE PACKETS

Thus far we have learned that when the intensity of ITCZ convection fluctuates, inertia-gravity wave packets are emitted toward the north and south. The movement of these wave packets depends critically on the wave guide effect, i.e., the effect by which the variable Coriolis parameter traps the inertia-gravity wave energy in the equatorial region (Blandford 1966). The meridional structure of our solutions in the last section are solely composed from the Hermite functions, which have both oscillatory and evanescent behavior. Now we take a different approach by abandoning the idea of Hermite functions and instead assuming that the meridional structure of the solutions are solely oscillatory. This procedure is often called an asymptotic, Liouville-Green (LG), or Wentzel-Kramers-Brillouine-Jeffreys (WKBJ) analysis. To accomplish this, we seek approximate solutions

of the homogeneous version of (4.6). The approximate solutions have the form

$$\hat{\psi}_m(y, t) = A_m(y, t)e^{i\varphi_m(y, t)}, \quad (4.34)$$

where $\varphi_m(y, t)$ is the phase and $A_m(y, t)$ is the local amplitude. The local meridional wavenumber $\ell(y, t)$ and the local frequency $\omega(y, t)$ are defined by

$$\ell(y, t) = \frac{\partial\varphi(y, t)}{\partial y} \quad \text{and} \quad \omega(y, t) = -\frac{\partial\varphi(y, t)}{\partial t}, \quad (4.35)$$

and a relationship that immediately follows (4.35) is

$$\frac{\partial\ell}{\partial t} + \frac{\partial\omega}{\partial y} = 0. \quad (4.36)$$

Note that we have dropped the subscript m and superscript $\hat{\psi}$ for convenience. The functions $A(y, t)$, $\ell(y, t)$, and $\omega(y, t)$ are all assumed to be slowly varying in y and t . Substituting (4.34) into the homogeneous version of (4.6), neglecting y and t derivatives of the slowly varying functions $A(y, t)$, $\ell(y, t)$, and $\omega(y, t)$, we obtain the local dispersion relation

$$\omega(y, t) = \pm [c^2\ell^2(y, t) + \beta^2y^2]^{1/2}. \quad (4.37)$$

Note that, because of the β^2y^2 term in (4.37), the inertia-gravity waves propagate through a nonuniform medium. In other words, ω varies as a function of both ℓ and y , whereas ω depends on only ℓ in a uniform medium. From (4.36) and with the knowledge of the additional dependence of ω on y , we can rewrite (4.36) as

$$\frac{\partial\ell}{\partial t} + \frac{\partial\omega}{\partial\ell} \frac{\partial\ell}{\partial y} = -\frac{\partial\omega}{\partial y},$$

and in its characteristic form (Whitham 1974)

$$\frac{d\ell}{dt} = -\frac{\partial\omega}{\partial y} \quad \text{on} \quad \frac{dy}{dt} = \frac{\partial\omega}{\partial\ell}. \quad (4.38)$$

As discussed by Whitham (1974), the trajectory (or group velocity) of a wave packet is given by

$$\frac{dy}{dt} = \frac{\partial\omega}{\partial\ell} = \frac{c^2\ell}{\omega}, \quad (4.39)$$

where the rightmost formula is computed after using the dispersion relation (4.37) and neglecting y and t derivatives of the slowly varying function $\ell(y, t)$. Along this trajectory, ω satisfies the relation

$$\frac{d\omega}{dt} = 0, \quad (4.40)$$

where we have used the assumption that medium is independent of time in (4.40). In summary, we have

$$\left. \begin{array}{l} \frac{d\omega}{dt} = 0 \\ \frac{d\ell}{dt} = -\frac{\partial\omega}{\partial y} \end{array} \right\} \quad \text{on} \quad \frac{dy}{dt} = \frac{\partial\omega}{\partial\ell}. \quad (4.41)$$

Using the local dispersion relation (4.37), we can write (4.39) in the form

$$\frac{dy}{(\omega^2 - \beta^2 y^2)^{1/2}} = \pm \frac{c dt}{\omega}. \quad (4.42)$$

Similarly, we can write first entry in (4.40) in the form

$$\frac{d\ell}{(\omega^2 - c^2 \ell^2)^{1/2}} = \pm \frac{\beta dt}{\omega}. \quad (4.43)$$

Integration of (4.42) and (4.43) yields the solutions

$$y(t) = \left(\frac{\omega}{\beta}\right) \sin \left\{ \sin^{-1} \left(\frac{\beta y_0}{\omega}\right) \pm \frac{\beta ct}{\omega} \right\}. \quad (4.44)$$

$$\ell(t) = \left(\frac{\omega}{c}\right) \cos \left\{ \sin^{-1} \left(\frac{\beta y_0}{\omega}\right) \pm \frac{\beta ct}{\omega} \right\}. \quad (4.45)$$

Note that (4.44) describes two rays, one starting at y_0 and initially moving northward, and the other also starting at y_0 but initially moving southward. Plots of $y(t)$ and $\ell(t)$ are shown in Figure 4.13 for $m = 1$ and two arbitrary initial meridional wavenumbers, $\ell(t = 0) = 1, 2 \times 10^{-3} \text{ km}^{-1}$. Note how the rays $y(t)$ bounce back at particular turning latitudes, ≈ 2560 and 4410 km . Recall that we introduced turning latitudes in the previous section, but because we have abandoned the idea of meridional modes n , the turning latitudes seen in Fig. 4.13 do not correspond to any particular meridional mode. When the wave packets reach their turning latitude their local meridional wavenumber crosses $\ell = 0$, which signifies that this analysis breaks down as discussed in Wunsch and Gill (1976). Also note how the rays spread out over time. This behavior has to do with the fact that the energy decays along rays with time following the formula

$$\frac{d\mathcal{E}}{dt} = -\frac{\mathcal{E}}{t}, \quad (4.46)$$

where $\mathcal{E} = \frac{1}{2}\omega^2 A^2$ is the energy as derived using Whitham's the variational approach (Whitham 1974).

4.8. CONCLUDING REMARKS

To understand the dynamics of the deep and shallow meridional overturning circulations, a zonally symmetric model on the equatorial β -plane has been formulated and the associated meridional circulation equation has been derived. This meridional circulation equation is a partial differential

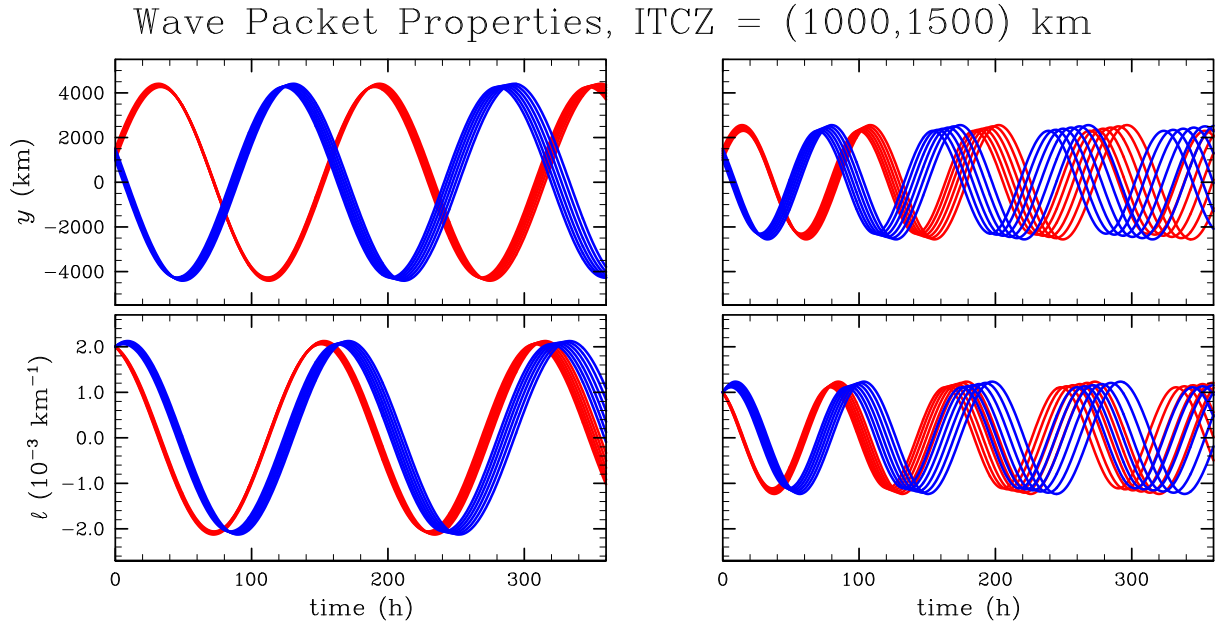


FIG. 4.13. Solutions of (4.44) and (4.45) for $m = 1$ and two arbitrary initial meridional wavenumbers, $\ell(t = 0) = 1, 2 \times 10^{-3} \text{ km}^{-1}$. Note how the rays $y(t)$ bounce at particular turning latitudes, ≈ 2560 and 4410 km.

equation in (y, z, t) . It contains two types of forcing: (1) horizontal variation of the interior diabatic heating; (2) Ekman pumping at the top of the boundary layer. Since the problem is linear, the meridional circulations attributable to these two forcing effects can be treated separately, and then the resulting flows can simply be added together to obtain the total response. In this chapter we focus on the diabatic heating of the $m = 0, 1, 2$ vertical modes as the forcing.

The meridional circulation equation has been solved analytically by first performing a vertical transform that converts the partial differential equation in (y, z, t) into a system of partial differential equations in (y, t) for the meridional structures of all the vertical modes. These partial differential equations have been solved via both the Green's function approach (evanescent basis functions) and the Hermite transform approach (oscillatory basis functions). These two approaches yield two different mathematical representations of the same physical solution. For understanding the basic asymmetry between the intensities of the winter hemisphere and the summer hemisphere

Hadley cells, the Green's function approach is preferable because of the efficiency of the mathematical representation, which is simply a superposition of two Green's functions written in terms of parabolic cylinder functions of order $-\frac{1}{2}$. For understanding the transient behavior of the Hadley cells it is preferable to solve the equations using Hermite functions.

The solutions illustrate the fundamental result which involves inertia-gravity wave packets emanating from the ITCZ and bouncing off a spectrum of turning latitudes when the ITCZ is switched on at various rates. These packets are therefore equatorially-trapped and cause the Hadley cells to pulsate with a period of about 1, 2, and 3 days for the $m = 0, 1, 2$ vertical modes. When the forcing is switched on slowly (e.g., about 100 hours to be almost fully switched on), the transient behavior is minimal, and the solutions are similar to the balanced results shown in Gonzalez and Mora Rojas (2014). When the ITCZ is located off the equator, both parts of the response reveal a basic asymmetry between the winter and summer hemispheres, with the winter hemisphere side containing most of the quasi-balanced compensating subsidence and most of the transient inertia-gravity wave activity.

In closing we note that the analytical solutions of the meridional circulation equation are consistent with the extent and shape of upper tropospheric dry regions regularly observed in satellite water vapor images, such as the one shown in Figure 4.1. These upper tropospheric dry regions play an important role in our ability to observe the universe with surface-based visible, infrared, and millimeter/sub-millimeter telescopes. The best astronomical observatory sites are at high altitudes in regions of persistently low upper tropospheric water vapor, such as Mauna Kea, Hawaii, the mountains of northern Chile, and the Canary Islands. These sites are above the trade wind inversion layer, which normally lies between 2000 and 2500 m. Above the trade wind inversion the

clear, dry air generally provides excellent observing conditions, but there can be important variations on synoptic, seasonal, and interannual time scales. As discussed by Businger et al. (2002), forecasts of weather conditions can play an important role in telescope scheduling and observing strategy at these sites.

In closing, we iterate that the tropical atmosphere may contain a considerable amount of inertia-gravity wave activity which our present observational systems are not capable of detecting. Therefore, this theoretical work should serve as motivation for future observational work on inertia-gravity waves in the tropics.

CHAPTER 5

Shock-like Structures in the ITCZ Boundary Layer

5.1. SYNOPSIS

This chapter presents numerical solutions and idealized analytical solutions of zonally symmetric models of the ITCZ boundary layer. In the numerical model, the boundary layer zonal and meridional flow is forced by a specified pressure field, which can also be interpreted as a specified geostrophically balanced zonal wind field $u_g(\phi)$ or vorticity field $\zeta_g(\phi)$. To better understand the dynamics of boundary layer structures, analytical solutions are presented for two simplified versions of the model. In the simplified analytical models, which do not include horizontal diffusion, the $v(\partial v/a\partial\phi)$ term in the meridional equation of motion and the $v(\partial u/a\partial\phi)$ term in the zonal equation of motion produce discontinuities in the zonal and meridional wind, with associated singularities in the boundary layer pumping and the boundary layer vorticity. In the numerical model, which does include horizontal diffusion, the zonal and meridional wind structures are not true discontinuities, but are shock-like. Finally, the numerical model is forced by the Year of Tropical Convection (YOTC) reanalysis pressure gradient fields during July 2008, March 2009, and March 2010. The numerical model agrees well with the YOTC dynamical fields while adding important details about the boundary layer pumping and vorticity.

5.2. INTRODUCTION

Figure 5.1 is a GOES visible image of the Pacific on 24 November 2010, a day when the ITCZ formed a well-defined east-west line. A striking feature of this image, and many other similar

images, is the narrowness of the ITCZ, and hence the narrowness of the rising branch of the Hadley circulation (Charney 1968). The purpose of this chapter is to better understand the dynamical

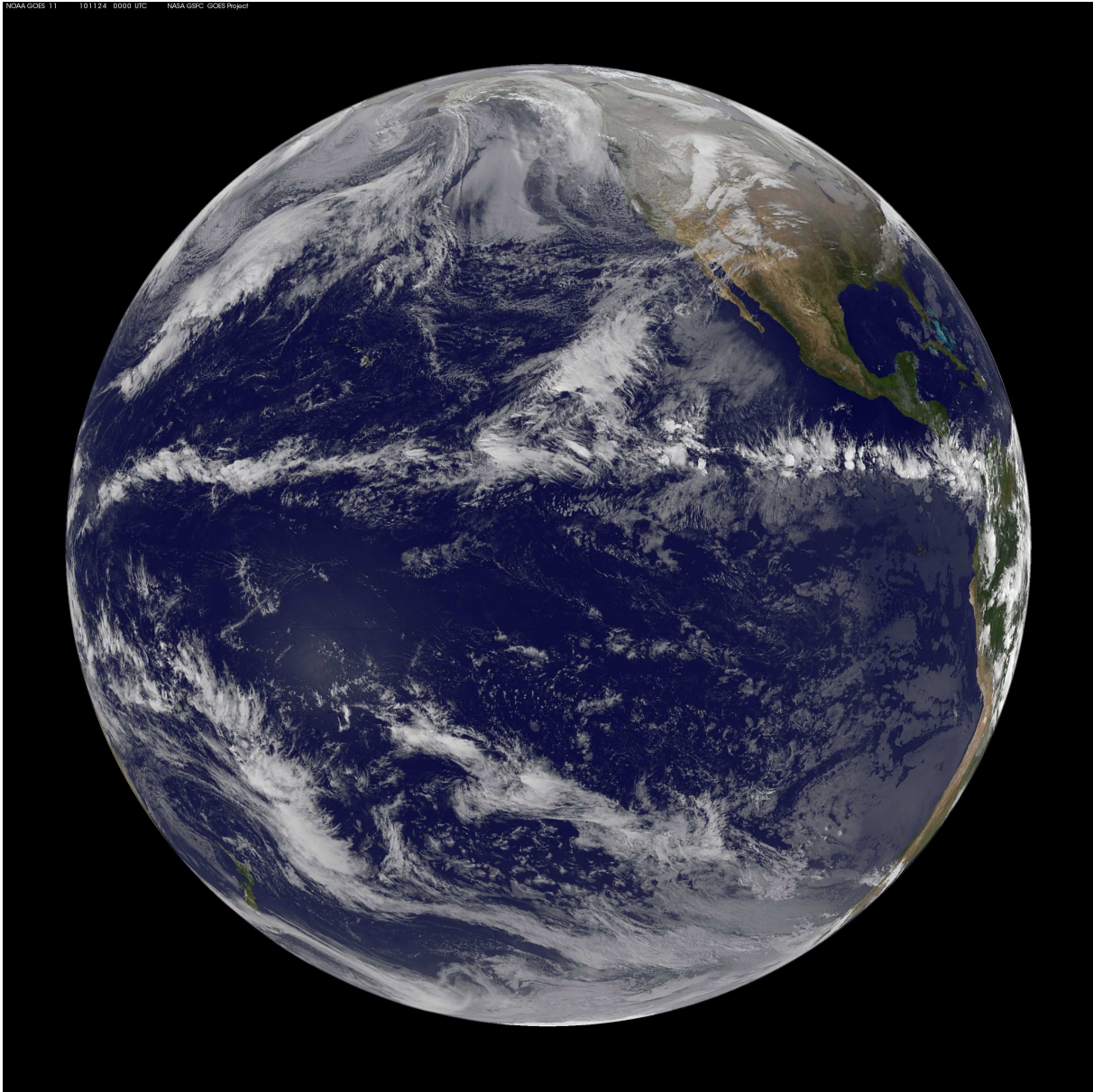


FIG. 5.1. NOAA GOES 11 visible image at 00:00 UTC on 24 November 2010.

reasons for this feature. The question is explored by examining the meridional distribution of Ekman pumping at the top of the boundary layer in and around the ITCZ. The argument is based on a zonally symmetric slab boundary layer model which does not strictly conform to Ekman

balance. The model includes the meridional advection terms, such as $v(\partial v/a\partial\phi)$, where v is the meridional velocity, ϕ is the latitude, and a is the Earth's radius. When the boundary layer meridional flow is strong, the neglect of this advection term in the meridional momentum equation is not justifiable. With the inclusion of the $v(\partial v/a\partial\phi)$ term in the boundary layer dynamics, shock-like structures can appear in both the u and v fields, and the relative vorticity and Ekman pumping can become very localized. The term, "shock" refers to a discontinuity in the wind field in the absence of horizontal diffusion whereas "shock-like" refers to a sharp gradient that is not a true discontinuity due to the presence of diffusion. An analogous process in the hurricane eyewall has recently been studied by Williams et al. (2013) and Slocum et al. (2014). If a hurricane can be described as a mesoscale power plant (the eyewall) with a synoptic scale supporting structure Ooyama (1997), then the Hadley circulation can be described as a mesoscale power plant (the ITCZ) with a planetary scale supporting structure.

Classic theory on the formation of the ITCZ stems back to papers such as Charney (1968, 1971); Holton et al. (1971); Yamasaki (1971); Pike (1971, 1972). All of these studies focused on the idea that the ITCZ rarely forms on the equator and does not form poleward of about 20° . In particular, Charney (1971) and Pike (1971) theorized that the ITCZ may form near the equator but quickly moves poleward due to the upwelling of cold SSTs in the presence of easterly flow. Holton et al. (1971) approached the problem by using linearized boundary layer equations on the equatorial β -plane forced by a specified pressure field. They found that convergence is frictionally driven and concentrated at critical latitudes, where the disturbance frequency is equal to the Coriolis parameter. Holton (1975) extended Holton et al. (1971) by including the horizontal advection terms and forcing the model with a mixed Rossby-gravity wave geopotential field. Once again, low-level convergence was concentrated near the critical latitudes. Mahrt (1972a,b) considered the

effects of horizontal advection in a zonally symmetric equatorial β -plane model. These studies showed that cross-equatorial flow can produce a thick advective boundary layer with strong cross-isobar flow and with significant off-equatorial rising motion where there is a transition from an advective-type layer to a quasi-Ekman-type layer. This was further explored by Smith and Mahrt (1981), but on an f -plane, with the result that low-level convergence is also located at the critical latitudes. Despite what seemed to be general agreement between many of these studies on the idea of low-level convergence being concentrated at the critical latitudes, the acceptance of these ideas began to fade in the early-mid 1980s.

Lindzen and Nigam (1987) presented what is now a well-accepted theory on some of the key mechanisms to understanding the ITCZ from a steady-state perspective. Their model conforms to an Ekman balance in the horizontal momentum equations, which is a balance between the Coriolis, pressure gradient, and frictional forces. They illustrate the importance of SST gradients in creating large-scale pressure gradients which in turn enhance low-level horizontal wind convergence. Although there are some limits to their model, they do not use a traditional slab boundary layer model in that they suppress the influence of the higher layers by forcing horizontal pressure gradients to vanish at 700 hPa. Therefore, they have to use a “back-pressure” effect to include a free tropospheric redistribution of mass with the trade cumulus boundary layer to minimize excessive surface convergence. Their model also neglects the local tendencies and horizontal advection of the horizontal winds, e.g., $v(\partial u/a\partial\phi)$ and $v(\partial v/a\partial\phi)$. Therefore, Lindzen and Nigam (1987) treat the ITCZ as a balanced phenomenon instead of a transient phenomenon that goes through ITCZ breakdown and reformation (Nieto Ferreira and Schubert 1997; Wang and Magnusdottir 2006).

Since Lindzen and Nigam (1987), many studies choose to use a set of equations that is in some balance to understand the ITCZ boundary layer. For example, the extended Ekman model

(a local balance) was used by Stevens et al. (2002) and by McGauley et al. (2004). Raymond et al. (2006) studied data from the East Pacific Investigations of Climate (EPIC) field project and also used the extended Ekman model. They argued that scale analysis shows that the $v(\partial v/a\partial\phi)$ term is not important. However, in shock formation there is no well-defined horizontal scale on which to base a scale analysis due to scale-collapse. A more general model, one that includes the $v(\partial v/a\partial\phi)$ term, was used by Tomas et al. (1999), who suggest that the meridional advection of the zonal velocity $v(\partial u/a\partial\phi)$ is the term most vital to correctly simulating the ITCZ. They claim that this term allows for anticyclonic absolute vorticity to form on the low pressure side of the equator, leading to a convergence-divergence doublet in the boundary layer. Sobel and Neelin (2006) studied the ITCZ boundary layer and free troposphere using an equatorial β -plane model which includes the $v(\partial u/a\partial\phi)$ and $v(\partial v/a\partial\phi)$ terms. Their experiments were run until a steady state was reached, and then a scale analysis of the individual terms was performed. They note that SST gradients associated with the Lindzen and Nigam (1987) effect are most important in determining ITCZ width and intensity. Indeed the next largest term in their scale analysis is the horizontal advection, but it's likely that their large diffusion might lessen the effects of shocks. In fact, as they decrease the value of the horizontal moisture diffusivity, they produce narrower and more intense ITCZs, but state that such precipitation rates are unrealistic.

A recent study by Back and Bretherton (2009b) agrees with some of the ideas in Lindzen and Nigam (1987) and Sobel and Neelin (2006). More specifically, Back and Bretherton (2009b) suggest that boundary layer temperature gradients are the primary contributor to the meridional winds, low-level convergence, and 850 hPa vertical motion, while the zonal surface winds are mainly determined by free tropospheric pressure gradients and downward momentum mixing. In this study, we present a dynamical and transient viewpoint of the ITCZ, where the pressure gradient

in and just above the boundary layer support both the evolution of the boundary layer zonal and meridional winds along with the formation and narrowing of Ekman pumping and vorticity in the ITCZ due to the Burgers' equation (Burgers 1948) embedded in the meridional momentum equation.

Another interesting feature of the tropical circulation is the formation of ITCZs just north and south of the equator, often referred to as double ITCZs. Figure 5.2 is a GOES visible image of the Pacific on 11 March 2015, a day when the eastern Pacific contained two thin ITCZs on either side of the equator. There are many observational papers on the double ITCZ in the eastern Pacific, starting with Hubert et al. (1969) and continuing with the work of Hayes et al. (1989), Mitchell and Wallace (1992); Lietzke et al. (2001); Zhang (2001); Liu and Xie (2002). A very interesting paper is that of Gu et al. (2005), who analyzed TRMM precipitation data and QuikScat surface wind divergence data for several boreal springs (March and April). They identify four types of patterns in the eastern Pacific: (1) El Niño; (2) double ITCZ; (3) north dominant double ITCZ; (4) south dominant double ITCZ. This chapter discusses some of the dynamical reasons for the formation of double ITCZs in regions such as the eastern Pacific. Many studies identify double ITCZs by convection or precipitation using satellite data mainly because there is a lack of observational wind data in the tropics. If double ITCZs were instead defined using the low-level convergence field, as the name ITCZ suggests, double ITCZs seem to be more common, as suggested by Liu and Xie (2002) and McNoldy et al. (2004). In fact, Liu and Xie (2002) note that double ITCZs are common year round in both the Atlantic and eastern Pacific Ocean. There are a number of theories that explore why low-level convergence does not always lead to convection, such as those described by Zhang et al. (2004), Gonzalez and Mora Rojas (2014), and Back and Bretherton (2006).

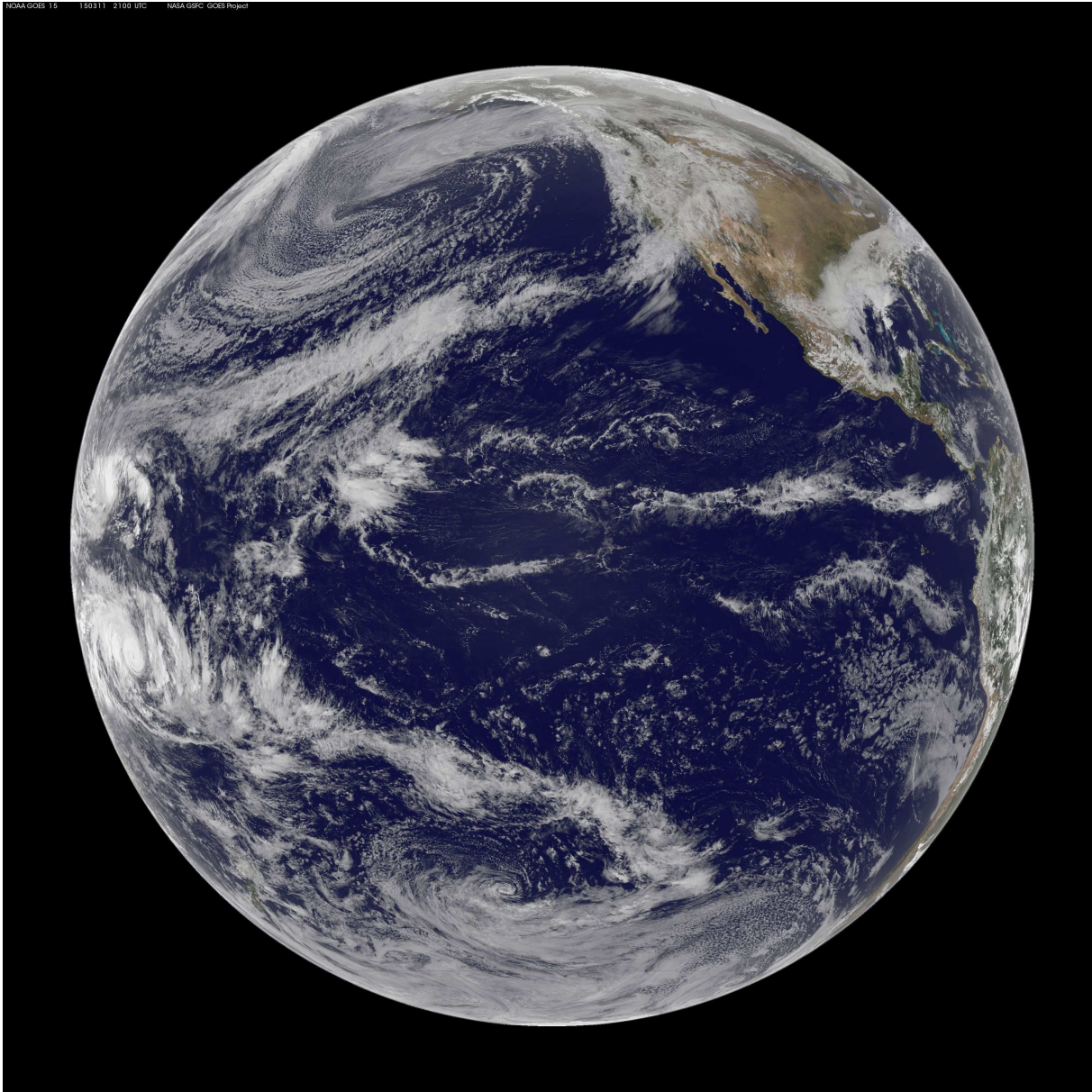


FIG. 5.2. NOAA GOES 11 visible image at 18:00 UTC on 11 March 2015.

The ITCZ boundary layer is an environment conducive to shock formation. We expect such shocks to appear intermittently in the ITCZ, causing thin east-west lines of deep convection in this conditionally unstable region. These lines are expected to be more common in the eastern oceans, where the opposing meridional flows associated with the subtropical highs are stronger.

The chapter is organized in the following way. Section 5.3 presents the governing set of partial differential equations for the slab model. Sections 5.4 and 5.5 present heuristic models in order

to gain insight into the role of Burgers' equation on the slab boundary layer dynamics. Section 5.6 contains numerical solutions of the slab boundary layer model forced by an idealized balanced zonal wind field. Section 5.7 presents numerical solutions of the slab boundary layer model forced by a pressure field from the Year of Tropical Convection (YOTC) reanalysis. Some concluding remarks are presented in section 5.8.

5.3. SLAB BOUNDARY LAYER MODEL

The model considers zonally symmetric, boundary layer motions of an incompressible fluid on the sphere. The frictional boundary layer is assumed to have constant depth h , with zonal and meridional velocities $u(\phi, t)$ and $v(\phi, t)$ that are independent of height between the top of a thin surface layer and height h , and with vertical velocity $w(\phi, t)$ at height h . In the overlying layer the meridional velocity is assumed to be negligible and the zonal velocity $u_g(\phi, t)$ is assumed to be in geostrophic balance and to be a specified function of latitude and time. The governing system of differential equations for the boundary layer variables $u(\phi, t)$, $v(\phi, t)$, and $w(\phi, t)$ then takes the form

$$\frac{\partial u}{\partial t} + v \frac{\partial u}{a \partial \phi} - \frac{w}{h} (1 - \alpha) (u - u_g) = \left(2\Omega \sin \phi + \frac{u \tan \phi}{a} \right) v - c_D U \frac{u}{h} + K \frac{\partial}{a \partial \phi} \left(\frac{\partial (u \cos \phi)}{a \cos \phi \partial \phi} \right), \quad (5.1)$$

$$\begin{aligned} \frac{\partial v}{\partial t} + v \frac{\partial v}{a \partial \phi} - \frac{w}{h} (1 - \alpha) v = & - \left(2\Omega \sin \phi + \frac{u \tan \phi}{a} \right) u - \frac{1}{\rho} \frac{\partial p}{a \partial \phi} - c_D U \frac{v}{h} \\ & + K \frac{\partial}{a \partial \phi} \left(\frac{\partial (v \cos \phi)}{a \cos \phi \partial \phi} \right), \end{aligned} \quad (5.2)$$

$$w = -h \frac{\partial (v \cos \phi)}{a \cos \phi \partial \phi} \quad \text{and} \quad \alpha = \begin{cases} 1 & \text{if } w \geq 0 \\ 0 & \text{if } w < 0, \end{cases} \quad (5.3)$$

where

$$U = 0.78 (u^2 + v^2)^{1/2} \quad (5.4)$$

is the wind speed at 10 m height, Ω is the Earth's rotation rate, and K is the constant horizontal diffusivity. The drag factor $c_D U$ is assumed to depend on the 10 m wind speed according to (Large et al. 1994)

$$c_D U = 10^{-3} (2.70 + 0.142 U + 0.0764 U^2), \quad (\text{for } U \leq 25), \quad (5.5)$$

where the 10 m wind speed U is expressed in m s^{-1} .

The boundary layer flow is driven by the same meridional pressure gradient force that occurs in the overlying fluid, so that, in the meridional equation of boundary layer motion, the pressure gradient force can be expressed as the specified function $[2\Omega \sin \phi + (u_g \tan \phi)/a]u_g$ so that equation (5.2) can be written in the form

$$\frac{\partial v}{\partial t} + v \frac{\partial v}{a \partial \phi} - \frac{w}{h} (1 - \alpha) v = - \left(2\Omega \sin \phi + \frac{(u + u_g) \tan \phi}{a} \right) (u - u_g) - c_D U \frac{v}{h} + K \frac{\partial}{a \partial \phi} \left(\frac{\partial (v \cos \phi)}{a \cos \phi \partial \phi} \right), \quad (5.6)$$

In the absence of the horizontal diffusion terms, the slab boundary layer equations constitute a hyperbolic system that can be written in characteristic form (see Appendix C). A knowledge of the characteristic form is useful in understanding the formation of shocks. In fact, before presenting numerical solutions of the system (5.1), (5.3), and (5.6) in section 6, we first discuss analytical solutions of two simplified versions of the model, i.e., two versions that have very simple characteristic forms. These analytical solutions aid in understanding the formation of discontinuities in the zonal and meridional flow, and hence singularities in the vorticity and vertical velocity.

5.4. HEURISTIC ARGUMENT I

The formation of shocks in the ITCZ boundary layer depends on the $v(\partial v/a\partial\phi)$ term in (5.2), with the term proportional to the ageostrophic zonal flow $(u - u_g)$ serving as a forcing mechanism for $(\partial v/\partial t)$, the surface friction term serving to damp v , and the horizontal diffusion term serving to control the structure near the shock. The formation of a shock in v leads to a shock in u through the $v(\partial u/a\partial\phi)$ term in (5.1). This discontinuity in the zonal flow means there is an east-west oriented infinite vorticity sheet in the boundary layer.

To obtain a semi-quantitative understanding of the above concepts before computing numerical solutions, we now approximate (5.1) and (5.2) by neglecting the horizontal diffusion terms, the w terms, the surface drag terms, and the $(u - u_g)$ forcing term. By making these assumptions, we aim to understand the atmospheric conditions needed to form shocks in the ITCZ boundary layer given a suite of different initial conditions. The zonal and meridional momentum equations (5.1) and (5.2) then simplify to

$$\frac{\partial m}{\partial t} + v \frac{\partial m}{a\partial\phi} = 0, \quad (5.7)$$

$$\frac{\partial v}{\partial t} + v \frac{\partial v}{a\partial\phi} = 0, \quad (5.8)$$

where $m = (u + \Omega a \cos \phi)a \cos \phi$ is the absolute angular momentum per unit mass.

The solutions of (5.7) and (5.8) are easily obtained by noting that these two equations can be written in the form

$$\frac{dm}{dt} = 0, \quad (5.9)$$

$$\frac{dv}{dt} = 0, \quad (5.10)$$

where $(d/dt) = (\partial/\partial t) + v(\partial/a\partial\phi)$ is the derivative following the boundary layer meridional motion. Integration of (5.9) and (5.10), with use of appropriate initial conditions yields the solutions

$$u(\phi, t) = \left(u_0(\hat{\phi}) + \Omega a \cos \hat{\phi} \right) \frac{\cos \hat{\phi}}{\cos \phi} - \Omega a \cos \phi, \quad (5.11)$$

$$v(\phi, t) = v_0(\hat{\phi}), \quad (5.12)$$

where the characteristics $\hat{\phi}(\phi, t)$ are given implicitly by

$$\phi = \hat{\phi} + (t/a)v_0(\hat{\phi}), \quad (5.13)$$

which is easily obtained by integration of $(d\phi/dt) = v/a$, with v given by (5.12). For a given $\hat{\phi}$, (5.13) defines a straight characteristic in (ϕ, t) , along which the absolute angular momentum $(u + \Omega a \cos \phi)a \cos \phi$ is fixed according to (5.11), and along which $v(\phi, t)$ is fixed according to (5.12).

To understand when the derivatives $(\partial u/\partial \phi)$ and $(\partial v/\partial \phi)$ become infinite, and to also check that (5.11)–(5.13) constitute solutions of (5.7) and (5.8), we first note that $(\partial/\partial t)$ and $(\partial/\partial \phi)$ of (5.13) yield

$$\begin{aligned} -\frac{\partial \hat{\phi}}{\partial t} &= \frac{v_0(\hat{\phi})}{a + tv'_0(\hat{\phi})}, \\ \frac{\partial \hat{\phi}}{\partial \phi} &= \frac{a}{a + tv'_0(\hat{\phi})}. \end{aligned} \quad (5.14)$$

Therefore $(\partial/\partial t)$ and $v(\partial/a\partial\phi)$ of $m(\phi, t) = m_0(\hat{\phi})$ yield

$$\begin{aligned}\frac{\partial m}{\partial t} &= m'_0(\hat{\phi})\frac{\partial\hat{\phi}}{\partial t} = -\frac{v_0(\hat{\phi})m'_0(\hat{\phi})}{a + tv'_0(\hat{\phi})}, \\ v\frac{\partial m}{a\partial\phi} &= v_0(\hat{\phi})m'_0(\hat{\phi})\frac{\partial\hat{\phi}}{a\partial\phi} = \frac{v_0(\hat{\phi})m'_0(\hat{\phi})}{a + tv'_0(\hat{\phi})},\end{aligned}\tag{5.15}$$

while $(\partial/\partial t)$ and $v(\partial/a\partial\phi)$ of $v(\phi, t) = v_0(\hat{\phi})$ yield

$$\begin{aligned}\frac{\partial v}{\partial t} &= v'_0(\hat{\phi})\frac{\partial\hat{\phi}}{\partial t} = -\frac{v_0(\hat{\phi})v'_0(\hat{\phi})}{a + tv'_0(\hat{\phi})}, \\ v\frac{\partial v}{a\partial\phi} &= v_0(\hat{\phi})v'_0(\hat{\phi})\frac{\partial\hat{\phi}}{a\partial\phi} = \frac{v_0(\hat{\phi})v'_0(\hat{\phi})}{a + tv'_0(\hat{\phi})},\end{aligned}\tag{5.16}$$

where the final equalities in (5.15) and (5.16) follow from using (5.14) to eliminate $(\partial\hat{\phi}/\partial t)$ and $(\partial\hat{\phi}/\partial\phi)$. The sum of the two lines in (5.15) then confirms that (5.11) and (5.13) constitute a solution of (5.7), while the sum of the two lines in (5.16) confirms that (5.12) and (5.13) constitute a solution of (5.8). However, these solutions may be multivalued, in which case (5.11) and (5.12) must be amended in such a way as to guarantee the solutions are single valued. We will return to this point by using a shock fitting procedure later. From the denominators on the right hand sides of (5.15) and (5.16), it is evident that the derivatives $(\partial m/\partial t)$, $(\partial m/\partial\phi)$, $(\partial v/\partial t)$, and $(\partial v/\partial\phi)$ become infinite when

$$tv'_0(\hat{\phi}) = -a\tag{5.17}$$

along one or more of the characteristics. Let $\hat{\phi}_s$ denote the characteristic that originates at the minimum value of $v'_0(\hat{\phi})$, i.e., $v'_0(\hat{\phi}_s) = [v'_0(\hat{\phi})]_{\min}$. Then, the time of shock formation, determined from (5.17), is

$$t_s = -\frac{a}{v'_0(\hat{\phi}_s)},\tag{5.18}$$

and the latitude of shock formation, determined from (5.13) and (5.18), is

$$\phi_s = \hat{\phi}_s - \frac{v_0(\hat{\phi}_s)}{v'_0(\hat{\phi}_s)}. \quad (5.19)$$

From the solutions (5.11) and (5.12) we can compute the solutions for the relative vorticity $\zeta(\phi, t) = -\partial[u(\phi, t) \cos \phi]/a \cos \phi \partial \phi$ and the divergence $\delta(\phi, t) = \partial[v(\phi, t) \cos \phi]/a \cos \phi \partial \phi$. It is interesting to first note that the way in which ζ and δ behave along a characteristic is quite different than the way in which m and v behave. For example, from (5.7) or (5.9), it is easily shown that

$$\frac{d\eta}{dt} = -\eta\delta, \quad (5.20)$$

where $\eta = 2\Omega \sin \phi + \zeta$ is the absolute vorticity. Thus, while m and v are fixed along a given characteristic according to (5.9) and (5.10), the absolute vorticity can rapidly increase along certain characteristics when $\delta < 0$. A similar argument applies to the variation of δ along certain characteristics.

The relative vorticity is obtained by differentiation of (5.11), which yields

$$\zeta(\phi, t) = \left(\frac{2\Omega \sin \hat{\phi} + \zeta_0(\hat{\phi})}{1 + (t/a)v'_0(\hat{\phi})} \right) \frac{\cos \hat{\phi}}{\cos \phi} - 2\Omega \sin \phi, \quad (5.21)$$

where $\zeta_0(\phi) = -\partial[u_0(\phi) \cos \phi]/a \cos \phi \partial \phi$ is the initial relative vorticity. Similarly, the boundary layer divergence $\delta(\phi, t)$, or equivalently the boundary layer pumping $w(\phi, t) = -h\delta(\phi, t)$, is obtained by using (5.12) in (5.3), which yields

$$w(\phi, t) = -\frac{h}{a} \left(\frac{v'_0(\hat{\phi})}{1 + (t/a)v'_0(\hat{\phi})} - v_0(\hat{\phi}) \tan \phi \right). \quad (5.22)$$

Because of the factors $1 + (t/a)v'_0(\hat{\phi})$ in the denominators of (5.21) and (5.22), the relative vorticity $\zeta(\phi, t)$ and the boundary layer pumping $w(\phi, t)$ become infinite at the same time ($t = t_s$) and the same place ($\phi = \phi_s$).

As a simple example, consider the initial condition

$$v_0(\phi) = v_m \left(\frac{2\phi_w(\phi_0 - \phi)}{\phi_w^2 + (\phi - \phi_0)^2} \right), \quad (5.23)$$

where the constants v_m , ϕ_0 , and ϕ_w specify the strength, location, and half-width of the initial ITCZ inflow. The derivative of (5.23) is

$$v'_0(\phi) = -\frac{2v_m}{\phi_w} \left(\frac{1 - [(\phi - \phi_0)/\phi_w]^2}{\{1 + [(\phi - \phi_0)/\phi_w]^2\}^2} \right). \quad (5.24)$$

From (5.18), the shock formation time is

$$t_s = \frac{a\phi_w}{2v_m}. \quad (5.25)$$

Table 5.1 lists the constants used in various test cases of Heuristic Model I and Heuristic Model II (to be discussed in the next section) using the initial conditions (5.23) and (5.24). Plots of $u(\phi, t)$, $v(\phi, t)$, $w(\phi, t)$, and $\zeta(\phi, t)$ are shown in Figure 5.3 for test case S5, which uses the constants: $a\phi_0 = 1000$ km, $v_m = 2.5$ m s⁻¹, and $a\phi_w = 400$ km. The u and v fields become discontinuous while the w and ζ fields become singular at $a\phi = a\phi_s = 1000$ km and $t = t_s = 22.2$ h. This implies that in the absence of surface drag, a shock would form in less than a day for a 800 km wide ITCZ with 2.5 m s⁻¹ meridional winds on either side. Of course surface drag does play a significant role on such timescales, therefore we extend Heuristic Model I to include a linearized surface drag in the next section.

TABLE 5.1. Test Cases and Results for Heuristic Models I and II

Test Case	Parameters Defining Initial Conditions			Typical Values Needed in Model II		Shock Results From Models I and II	
	$a\phi_w$ (km)	v_m (m s ⁻¹)	U (m s ⁻¹)	τ (h)	$a\phi_s$ (km)	$t_s^{(I)}$ (h)	$t_s^{(II)}$ (h)
S1	400	0.5	0.87	96.4	1000	111	No Shock
S2	400	1.0	2.84	74.7	1000	55.6	102
S3	400	1.5	3.33	69.1	1000	37.0	53.1
S4	400	2.0	4.20	59.8	1000	27.8	37.3
S5	400	2.5	4.36	58.2	1000	22.2	28.0
S6	400	3.0	4.55	56.4	1000	18.5	22.4
S7	400	3.5	4.76	54.4	1000	15.9	18.8
S8	400	4.0	4.99	52.3	1000	13.9	16.1

After shock formation, the multivalued solutions for (5.17)–(5.19) need to be amended by a shock fitting procedure that guarantees a single valued solution. Let $\Phi(t)$ denote the shock latitude at time t , and let $\hat{\phi}_1(t)$ denote the label of the characteristic that just touches the southern edge of the shock at time t , and let $\hat{\phi}_2(t)$ denote the label of the characteristic that just touches the northern edge of the shock at time t .

Then, using (5.19), we obtain the algebraic relations

$$\Phi(t) = \hat{\phi}_1(t) + (t/a)v_0(\hat{\phi}_1(t)), \quad (5.26)$$

$$\Phi(t) = \hat{\phi}_2(t) + (t/a)v_0(\hat{\phi}_2(t)). \quad (5.27)$$

Since the meridional velocity of the shock is simply the average of the (discontinuous) meridional flow velocities across the shock, the first order ordinary differential equation for $\Phi(t)$ is given by

$$a \frac{d\Phi(t)}{dt} = \frac{1}{2} \left[v_0(\hat{\phi}_1(t)) + v_0(\hat{\phi}_2(t)) \right], \quad (5.28)$$

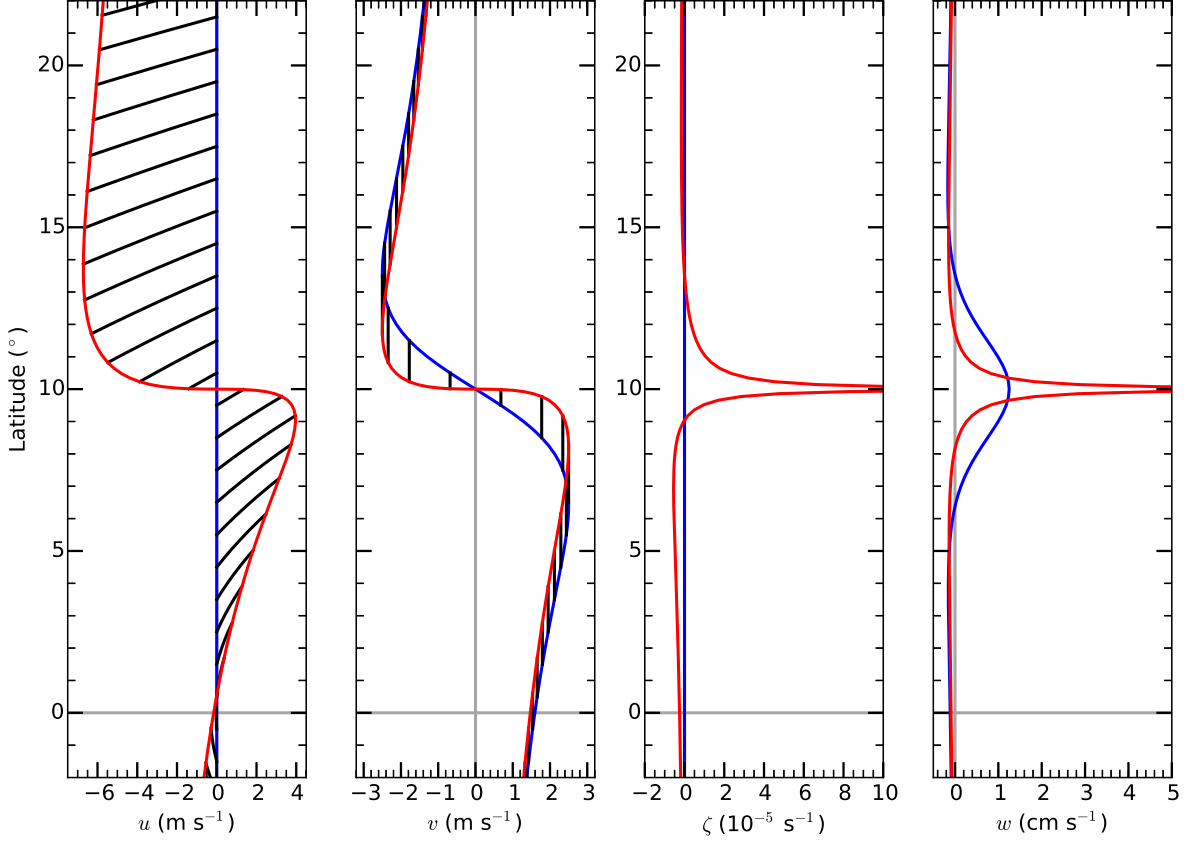


FIG. 5.3. Plots of $u(\phi, t)$, $v(\phi, t)$, $\zeta(\phi, t)$, and $w(\phi, t)$ at $t = 0$ in the blue curves, and right before shock formation, $t = t_s$ in the red curves for Heuristic Model I equations (5.7), (5.8), and (5.3). Fluid particle displacements are also shown by the black curves for equally spaced particles at the initial time. We use the initial condition (5.23) and the constants in test case S5: $a\phi_0 = 1000$ km, $v_m = 2.5$ m $^{-1}$, and $a\phi_w = 400$ km.

for the three functions $\Phi(t)$, $\hat{\phi}_1(t)$, $\hat{\phi}_2(t)$. Once the shock position $\Phi(t)$ is determined from (5.26)–(5.28), characteristics intersecting $\Phi(t)$ from lower latitudes are terminated there, while characteristics intersecting $\Phi(t)$ from higher latitudes are also terminated there. This guarantees that u and v are single valued but discontinuous across $\Phi(t)$. For more details about this procedure, refer to Whitham (1974).

Since the initial condition (5.23) is antisymmetric around $\phi = \phi_0$, the right hand side of $\Phi(t) = \phi_0$ for $t \geq t_s$. Thus, for the initial condition (5.23), the solution of (5.12) becomes

$$v(\phi, t) = v_m \left(\frac{2\phi_w(\phi_0 - \hat{\phi})}{\phi_w^2 + (\hat{\phi} - \phi_0)^2} \right), \quad (5.29)$$

where $\hat{\phi}(\phi, t)$ is given implicitly by

$$\phi = \hat{\phi} + v_m t \left(\frac{2\phi_w(\phi_0 - \hat{\phi})}{\phi_w^2 + (\hat{\phi} - \phi_0)^2} \right), \quad (5.30)$$

with the requirement that $\hat{\phi}(\phi, t) < \phi_0$ if $\phi < \phi_0$ and $\hat{\phi}(\phi, t) > \phi_0$ if $\phi > \phi_0$. Figure 5.4 shows another view of the solutions, via contours of $u(\phi, t)$ and $v(\phi, t)$ in the (ϕ, t) -plane, along with a family of characteristics $\hat{\phi}(\phi, t)$ for the choices $v_m = 2.5 \text{ m s}^{-1}$, $a\phi_0 = 1000 \text{ km}$, $a\phi_w = 400 \text{ km}$, and for $\hat{\phi} = -1.5^\circ, -0.5^\circ, \dots, 21.5^\circ$. It is apparent that v is constant along the characteristics but u increases in magnitude along characteristics. We can see why u increases in magnitude along characteristics by rewriting an approximate form of (5.7) as $(du/dt) \approx 2\Omega v \sin \phi$. The asymmetry in u about the $\phi = \phi_0$ arises from the $\sin \phi$ factor, allowing u to speed up faster on the north side of $\phi = \phi_0$.

5.5. HEURISTIC ARGUMENT II

We now consider a second analytical model that adds surface drag effects to the model considered in the previous section. For simplicity, we linearize the surface drag terms so the zonal and meridional momentum equations become

$$\frac{\partial m}{\partial t} + v \frac{\partial m}{a \partial \phi} = -\frac{m - m_e}{\tau}, \quad (5.31)$$

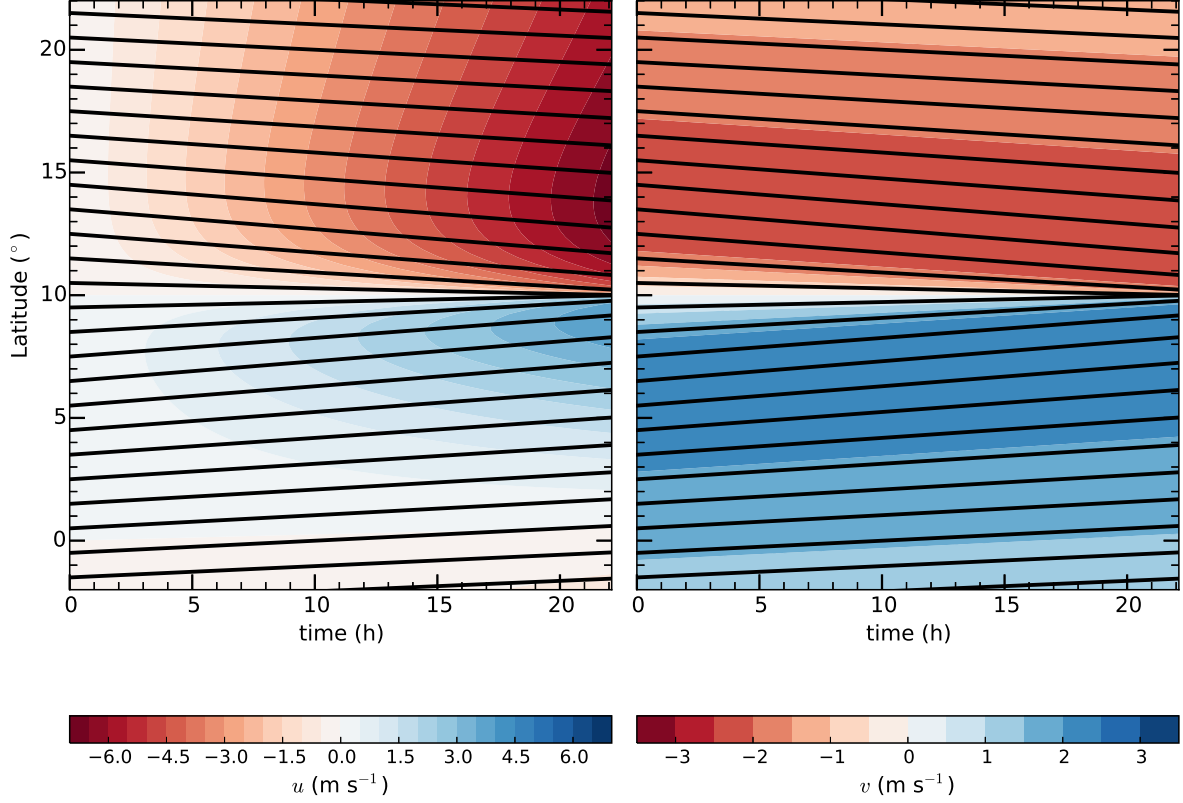


FIG. 5.4. Analytical solutions of the Heuristic Model I equations (5.7) and (5.8) of $u(\phi, t)$ and $v(\phi, t)$ in the (ϕ, t) -plane (contours), along with the family of characteristics $\hat{\phi}(\phi, t)$ for test case S5, and where $\hat{\phi} = -1.5^\circ, -0.5^\circ, \dots, 21.5^\circ$.

$$\frac{\partial v}{\partial t} + v \frac{\partial v}{a \partial \phi} = -\frac{v}{\tau}, \quad (5.32)$$

where the constant damping time scale τ is a typical value of $h/(c_D U)$ computed using typical values of U .

The solutions of (5.31) and (5.32) are easily obtained by noting that these two equations can be written in the form

$$\frac{d}{dt} (u \cos \phi e^{t/\tau} + v e^{t/\tau} F(\phi, t)) = 0, \quad (5.33)$$

$$\frac{d}{dt} (v e^{t/\tau}) = 0, \quad (5.34)$$

where $(d/dt) = (\partial/\partial t) + v(\partial/a\partial\phi)$ is the derivative following the boundary layer meridional motion and $F(\phi, t)$ is given by

$$F(\phi, t) = \Omega\tau \left\{ \sin [2(\phi + \tau v/a)] \text{ci}(2\tau v/a) - \cos [2(\phi + \tau v/a)] \text{si}(2\tau v/a) \right\}, \quad (5.35)$$

and where

$$\text{si}(x) = - \int_x^\infty \frac{\sin x'}{x'} dx' \quad \text{and} \quad \text{ci}(x) = - \int_x^\infty \frac{\cos x'}{x'} dx' \quad (5.36)$$

are respectively the sine integral and the cosine integral. Therefore $x(d/dx) \text{ci}(x) = \cos(x)$ and $x(d/dx) \text{si}(x) = \sin(x)$.

Integration of (5.33) and (5.34), with use of appropriate initial conditions and (5.35), yields the solutions

$$u(\phi, t) = \left\{ u_0(\hat{\phi}) \cos \hat{\phi} - v_0(\hat{\phi}) [F(\phi, t) - F_0(\hat{\phi})] \right\} \frac{e^{-t/\tau}}{\cos \phi}, \quad (5.37)$$

$$v(\phi, t) = v_0(\hat{\phi}) e^{-t/\tau}, \quad (5.38)$$

where the characteristics $\hat{\phi}(\phi, t)$ are given implicitly by

$$\phi = \hat{\phi} + (\hat{t}/a)v_0(\hat{\phi}), \quad (5.39)$$

which is easily obtained by integration of $(d\phi/dt) = v/a$, with v given by (5.38), and where

$$\hat{t} = \tau (1 - e^{-t/\tau}). \quad (5.40)$$

For a given $\hat{\phi}$, (5.39) defines a curved characteristic in (ϕ, t) , along which $v(\phi, t)$ exponentially damps according to (5.38).

To check that (5.37) and (5.38) constitute a solution of (5.31) and (5.32), we first note that $(\partial/\partial t)$ and $(\partial/\partial\phi)$ of (5.39) yield

$$\begin{aligned} -\frac{\partial\hat{\phi}}{\partial t} &= \frac{v_0(\hat{\phi})e^{-t/\tau}}{a + \hat{t}v'_0(\hat{\phi})} \\ \frac{\partial\hat{\phi}}{\partial\phi} &= \frac{a}{a + \hat{t}v'_0(\hat{\phi})}, \end{aligned} \tag{5.41}$$

so that $(\partial/\partial t + 1/\tau)$ and $v(\partial/a\partial\phi)$ of (5.37) yields

$$\begin{aligned} \frac{\partial m}{\partial t} + \frac{m - m_e}{\tau} &= a \left[a\zeta_0(\hat{\phi}) \cos \hat{\phi} + v_0(\hat{\phi})F'_0(\hat{\phi}) \right] \frac{\partial\hat{\phi}}{\partial t} e^{-t/\tau} \\ &\quad - a \left(\frac{\partial v}{\partial t} + \frac{v}{\tau} \right) \left[F(\phi, t) - F_0(\hat{\phi}) \right] - va \frac{\partial F}{\partial t} \\ v \frac{\partial m}{a\partial\phi} &= \left[a\zeta_0(\hat{\phi}) \cos \hat{\phi} + v_0(\hat{\phi})F'_0(\hat{\phi}) \right] \frac{\partial\hat{\phi}}{\partial\phi} v_0(\hat{\phi}) e^{-2t/\tau} \\ &\quad - v \frac{\partial v}{\partial\phi} \left[F(\phi, t) - F_0(\hat{\phi}) \right] - v^2 \frac{\partial F}{\partial\phi} - 2\Omega va \sin \phi \cos \phi, \end{aligned} \tag{5.42}$$

and $(\partial/\partial t + 1/\tau)$ and $v(\partial/a\partial\phi)$ of (5.38) yields

$$\begin{aligned} \frac{\partial v}{\partial t} + \frac{v}{\tau} &= e^{-t/\tau} v'_0(\hat{\phi}) \frac{\partial\hat{\phi}}{\partial t} = -\frac{e^{-2t/\tau} v_0(\hat{\phi}) v'_0(\hat{\phi})}{a + \hat{t}v'_0(\hat{\phi})}, \\ v \frac{\partial v}{a\partial\phi} &= e^{-2t/\tau} v_0(\hat{\phi}) v'_0(\hat{\phi}) \frac{\partial\hat{\phi}}{a\partial\phi} = \frac{e^{-2t/\tau} v_0(\hat{\phi}) v'_0(\hat{\phi})}{a + \hat{t}v'_0(\hat{\phi})} \end{aligned} \tag{5.43}$$

The final equalities in (5.42) and (5.43) follow from using (5.41) to eliminate $(\partial\hat{\phi}/\partial t)$ and $(\partial\hat{\phi}/\partial\phi)$.

The sum of the four lines in (5.42) then confirms that (5.37) constitutes a solution of (5.31) and the sum of the two lines in (5.43) confirms that (5.38) constitutes a solution of (5.32). Once again, this solution may be multivalued, in which case (5.37)–(5.39) must be amended in such a way as to guarantee the solution is single valued. The shock fitting procedure involves solving the same system as (5.26) and (5.27) with t/a replaced by \hat{t}/a on the right hand sides and multiplying (5.28)

by $e^{t/\tau}$. From the denominators on the right hand sides of (5.42) and (5.43), it is evident that the derivatives $(\partial v/\partial t)$ and $(\partial v/a\partial\phi)$, for example, can become infinite if

$$(1 - e^{-t/\tau}) (\tau/a)v'_0(\hat{\phi}) = -1 \quad (5.44)$$

along one or more of the characteristics. This is possible if and only if

$$(\tau/a)[v'_0(\phi)]_{\min} < -1 \quad (5.45)$$

where $[v'_0(\phi)]_{\min}$ denotes the minimum value of the derivative of the initial condition. In other words, if the initial meridional velocity $v_0(\phi)$ has a large enough negative slope, the solution will become multivalued. The time of shock formation, determined from (5.44), is

$$t_s = -\tau \ln \left(1 - \frac{a}{\tau[v'_0(\phi)]_{\min}} \right). \quad (5.46)$$

From the solutions (5.37) and (5.38) we can compute the solutions for the relative vorticity $\zeta(\phi, t) = -\partial[u(\phi, t) \cos \phi]/a \cos \phi \partial\phi$ and the divergence $\delta(\phi, t) = \partial[v(\phi, t) \cos \phi]/a \cos \phi \partial\phi$. The relative vorticity is obtained by differentiation of (5.37), which yields

$$\begin{aligned} \zeta(\phi, t) = & v_0(\hat{\phi}) \frac{\partial F}{\partial \phi} \frac{e^{-t/\tau}}{a \cos \phi} \\ & + \left[\zeta_0(\hat{\phi}) a \cos \hat{\phi} + v'_0(\hat{\phi}) \left(F(\phi, t) - F_0(\hat{\phi}) \right) - v_0(\hat{\phi}) F'_0(\hat{\phi}) \right] \frac{e^{-t/\tau}}{a \cos \phi \left[1 + (\hat{t}/a)v'_0(\hat{\phi}) \right]}, \end{aligned} \quad (5.47)$$

where $\zeta_0(\phi) = -\partial[u_0(\phi) \cos \phi]/a \cos \phi \partial\phi$ is the initial relative vorticity. Similarly, the boundary layer divergence $\delta(\phi, t)$, or equivalently the boundary layer pumping $w(\phi, t) = -h\delta(\phi, t)$, is

obtained by using (5.38) in (5.3), which yields

$$w(\phi, t) = -\frac{h}{a} \left(\frac{v'_0(\hat{\phi})}{1 + (\hat{t}/a)v'_0(\hat{\phi})} - v_0(\hat{\phi}) \tan \phi \right) e^{-t/\tau}. \quad (5.48)$$

Because of the factors $1 + (t/a)v'_0(\hat{\phi})$ in the denominators of (5.47) and (5.48), the relative vorticity $\zeta(\phi, t)$ and the boundary layer pumping $w(\phi, t)$ become infinite at the same time ($t = t_s$) and the same place ($\phi = \phi_s$).

As a simple example, consider the initial condition given (5.23) from section 3. Note that the minimum value of $v'_0(\phi)$ occurs at $\phi = \phi_0$, so that $[v'_0(\phi)]_{\min} = -2v_m/\phi_w$ and the condition (5.44) for shock formation becomes

$$\frac{a\phi_w}{2\tau v_m} < 1. \quad (5.49)$$

When the initial condition satisfies (5.23), a shock forms at $\phi = \phi_0$. From (5.46), the shock formation time is

$$t_s = -\tau \ln \left(1 - \frac{a\phi_w}{2\tau v_m} \right). \quad (5.50)$$

The last column of Table 5.1 lists values of t_s for an ITCZ with half-width $a\phi_w = 400$ km and for eight values of v_m . Plots of $u(\phi, t)$, $v(\phi, t)$, $w(\phi, t)$, and $\zeta(\phi, t)$ are shown in Figure 5.5 for test case S5. The u and v fields become discontinuous while the w and ζ fields become singular at $a\phi = a\phi_s = 1000$ km and $t = t_s = 28.0$ h. Thus, if the difference in the meridional flow across a 800 km wide ITCZ is 1 m s^{-1} or larger, the surface drag in the meridional equation of motion cannot prevent the development of a shock in the v -field.

We also emphasize the dual role played by the surface stress terms. In the zonal equation of motion the surface stress term decelerates the zonal flow, producing subgeostrophic flow. In the meridional equation of motion this $(u - u_g)$ term produces a meridional flow down the pressure

gradient, which is favorable for shock formation. In contrast, the surface stress term in the meridional equation of motion tends to retard shock formation. For a narrow enough ITCZ, this retarding effect is overcome by the shock generation process.

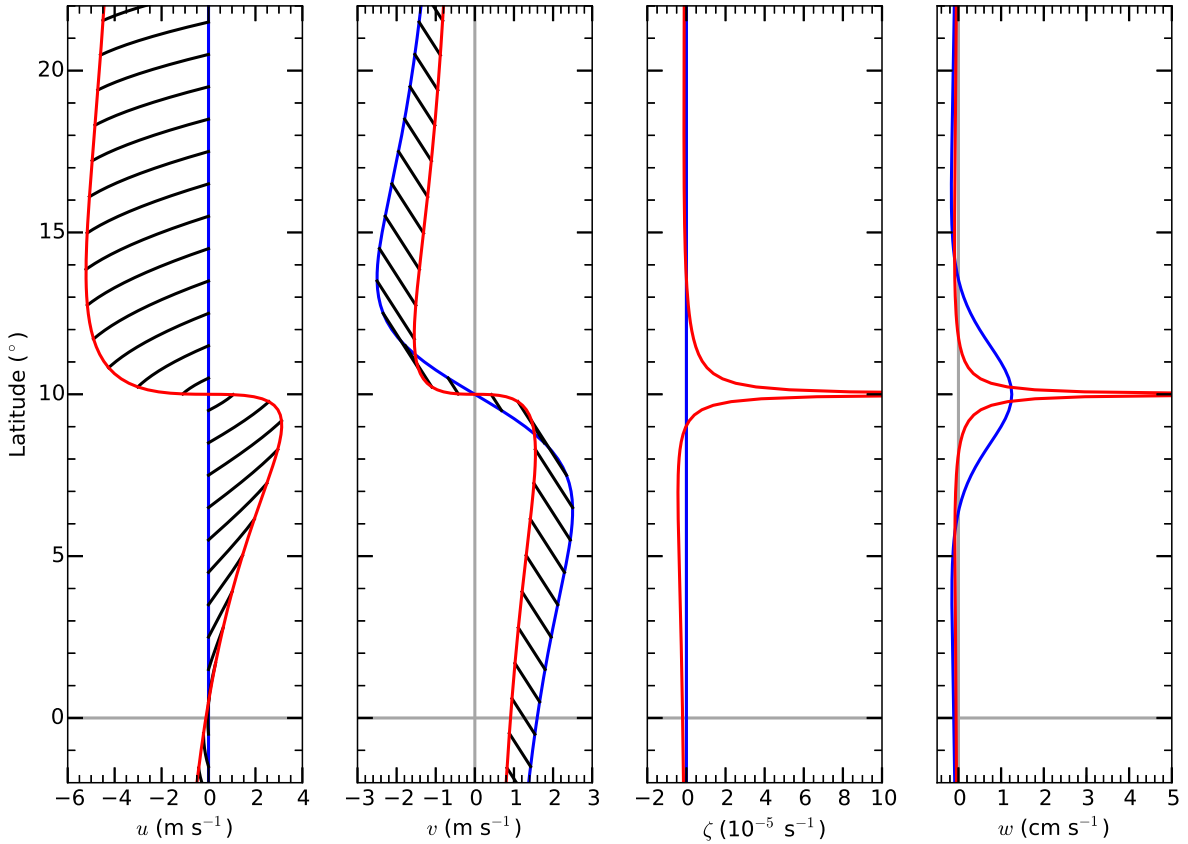


FIG. 5.5. Same as Figure 5.3, but for Heuristic Model II equations (5.31), (5.32), and (5.3) for test case S5.

Since the initial condition (5.23) is antisymmetric around $\phi = \phi_0$, $\Phi(t) = \phi_0$ for $t \geq t_s$. Thus, for the initial condition (5.23), the solution (5.37)–(5.38) becomes

$$v(\phi, t) = v_{\max} \left(\frac{2(\phi_0 - \hat{\phi})/\phi_w}{1 + [(\hat{\phi} - \phi_0)/\phi_w]^2} \right) e^{-t/\tau}, \quad (5.51)$$

where $\hat{\phi}(\phi, t)$ is given implicitly by

$$\phi = \hat{\phi} + v_{\max}(\tau/a) (1 - e^{-t/\tau}) \left(\frac{2(\phi_0 - \hat{\phi})/\phi_w}{1 + [(\hat{\phi} - \phi_0)/\phi_w]^2} \right), \quad (5.52)$$

with the requirement that $\hat{\phi}(\phi, t) < \phi_0$ if $\phi < \phi_0$ and $\hat{\phi}(\phi, t) > \phi_0$ if $\phi > \phi_0$. Figures 5.5 and 5.6 display isolines of $v(\phi, t)$ in the (ϕ, t) -plane, along with a family of characteristics $\hat{\phi}(\phi, t)$ for the choices $v_{\max} = 4 \text{ m s}^{-1}$, $a\phi_0 = 1000 \text{ km}$, $a\phi_w = 400 \text{ km}$, and for $\hat{\phi} = -1.5^\circ, -0.5^\circ, \dots, 21.5^\circ$. The characteristics are now curved instead of straight, indicating the retarding effect of surface drag. Because of this, v decreases along the characteristics but u still increases in magnitude along characteristics. We rewrite (5.31) in the approximate form $(du/dt) \approx 2\Omega v \sin \phi - u/\tau$ and realize that the surface drag is not strong enough to prevent u from increasing with time, but the magnitude of u is smaller compared to when surface drag is neglected.

5.6. NUMERICAL SIMULATION OF ITCZ SHOCKS - IDEALIZED u_g FORCING

Now that we have some understanding of how shocks form using a simplified version of the slab boundary layer model, we shall perform experiments with the full slab boundary layer equations, (5.1), (5.3), and (5.6). The problem has been solved using centered, second-order, spatial finite difference methods on the domain $-\pi/4 \leq \phi \leq \pi/4$ or $-45^\circ \leq \phi \leq 45^\circ$ with a uniform meridional grid spacing of $a\Delta\phi \approx 100 \text{ m}$, and a three-stage third-order strong stability-preserving Runge-Kutta time differencing scheme (Shu and Osher 1988) with a time step Δt of 5 s. The boundary conditions are given by

$$\left. \begin{aligned} \frac{\partial (u \cos \phi)}{\partial \phi} &= 0, \\ \frac{\partial (v \cos \phi)}{\partial \phi} &= 0, \end{aligned} \right\} \quad \text{at} \quad \phi = \pm \frac{\pi}{4}. \quad (5.53)$$

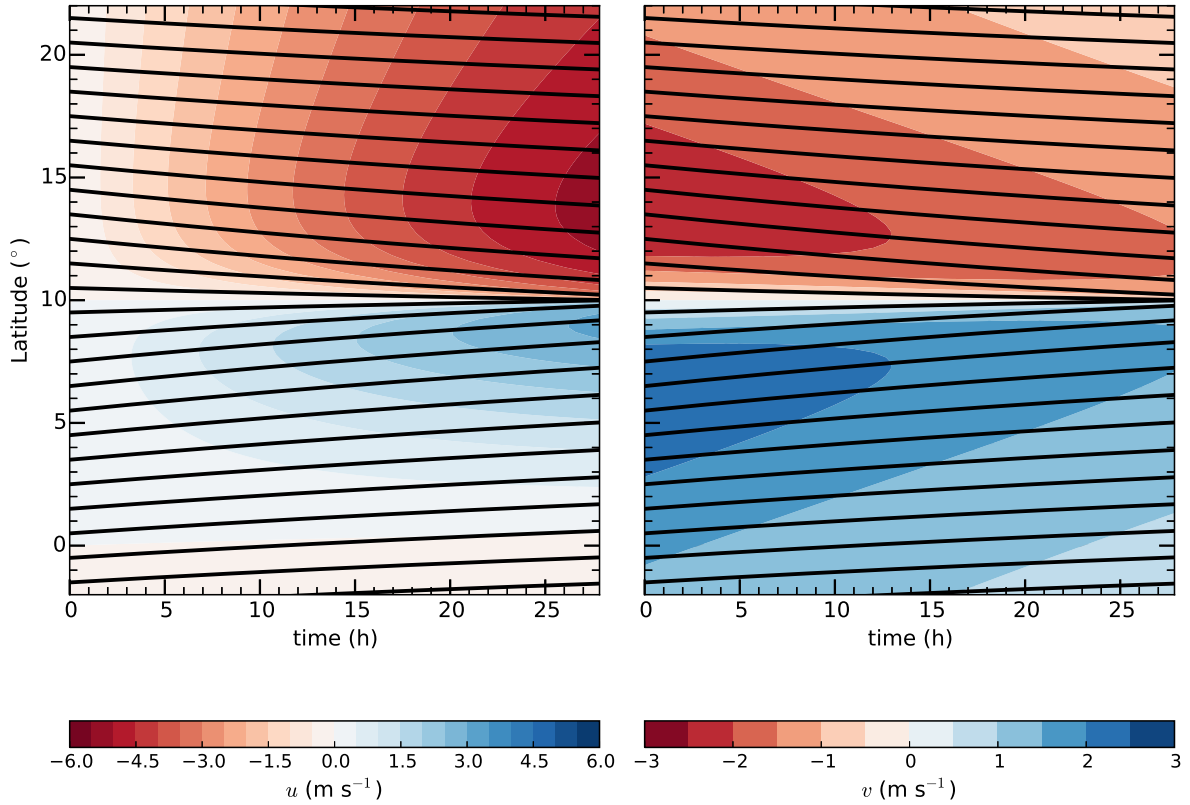


FIG. 5.6. Same as Figure 5.4, but for Heuristic Model II equations (5.31) and (5.32) for test case S5.

We would like to run the model until a steady state is reached, therefore we use the initial conditions $u(\phi, 0) = u_g(\phi)$ and $v(\phi, 0) = 0$. The constants have been chosen as $h = 1 \text{ km}$, $\rho = 1.2 \text{ kg m}^{-3}$, and $K = 1000 \text{ m}^2 \text{ s}^{-1}$. The CFL condition associated with the horizontal diffusion terms sets the stability constraint $K\Delta t / (a\Delta\phi)^2 \leq 2/3$ so that for $a\Delta\phi = 100 \text{ m}$ and $\Delta t = 5 \text{ s}$ we have to satisfy $K \leq 1333 \text{ m}^2 \text{ s}^{-1}$. The forcing is prescribed through the $\zeta_g(\phi)$ field, from which we can integrate

to compute $u_g(\phi)$ and $p(\phi)$. We assume ζ_g is of the form

$$\zeta_g(\phi) = \begin{cases} 0 & -\frac{\pi}{4} \leq \phi \leq \phi_1, \\ \zeta_1 S\left(\frac{\phi_2 - \phi}{\phi_2 - \phi_1}\right) & \phi_1 \leq \phi \leq \phi_2, \\ \zeta_1 S\left(\frac{\phi - \phi_2}{\phi_3 - \phi_2}\right) + \zeta_2 S\left(\frac{\phi_3 - \phi}{\phi_3 - \phi_2}\right) & \phi_2 \leq \phi \leq \phi_3, \\ \zeta_2 S\left(\frac{\phi - \phi_3}{\phi_4 - \phi_3}\right) + \zeta_3 S\left(\frac{\phi_4 - \phi}{\phi_4 - \phi_3}\right) & \phi_3 \leq \phi \leq \phi_4, \\ \zeta_3 S\left(\frac{\phi - \phi_4}{\phi_5 - \phi_4}\right) + \zeta_4 S\left(\frac{\phi_5 - \phi}{\phi_5 - \phi_4}\right) & \phi_4 \leq \phi \leq \phi_5, \\ \zeta_4 S\left(\frac{\phi - \phi_5}{\phi_6 - \phi_5}\right) & \phi_5 \leq \phi \leq \phi_6, \\ 0 & \phi_6 \leq \phi \leq \frac{\pi}{4}. \end{cases} \quad (5.54)$$

where $\phi_1, \phi_2, \phi_3, \phi_4, \phi_5, \phi_6, \zeta_1, \zeta_2, \zeta_3,$ and ζ_4 are specified constants, and $S(s) = 1 - 3s^2 + 2s^3$ is an interpolating function that satisfies $S(0) = 1, S(1) = 0,$ and $S'(1) = S'(0) = 0$. Figure 5.7 shows $\zeta_g(\phi)$ along with its associated fields $u_g(\phi)$ and $p(\phi)$ for the three test cases with the parameter values listed in Table 5.2. The difference between these ITCZs is the strength of the westerlies south of the relative vorticity maximum, with maximum westerlies of 0, 3, and 6 m s⁻¹ respectively. The $p(\phi, t)$ field illustrates that as the westerlies increase, the low pressure minimum north of the equator exceeds that of the minimum at the equator. Also note that the pressure difference between the tropics and subtropics is on the order of 6–8 hPa.

TABLE 5.2. Information about the first set of experiments at 10°.

Test Case	ϕ_1 (°)	ϕ_2 (°)	ϕ_3 (°)	ϕ_4 (°)	ϕ_5 (°)	ϕ_6 (°)	ζ_1 (10 ⁻⁶ s ⁻¹)	ζ_2 (10 ⁻⁶ s ⁻¹)	ζ_3 (10 ⁻⁶ s ⁻¹)	ζ_4 (10 ⁻⁶ s ⁻¹)
C1	-35	-20	6	10	20	40	6.20	-7.26	14.18	-6.80
C2	-35	-20	6	10	20	40	6.45	-9.18	18.20	6.90
C3	-35	-20	6	10	20	40	6.66	-11.10	22.40	7.00

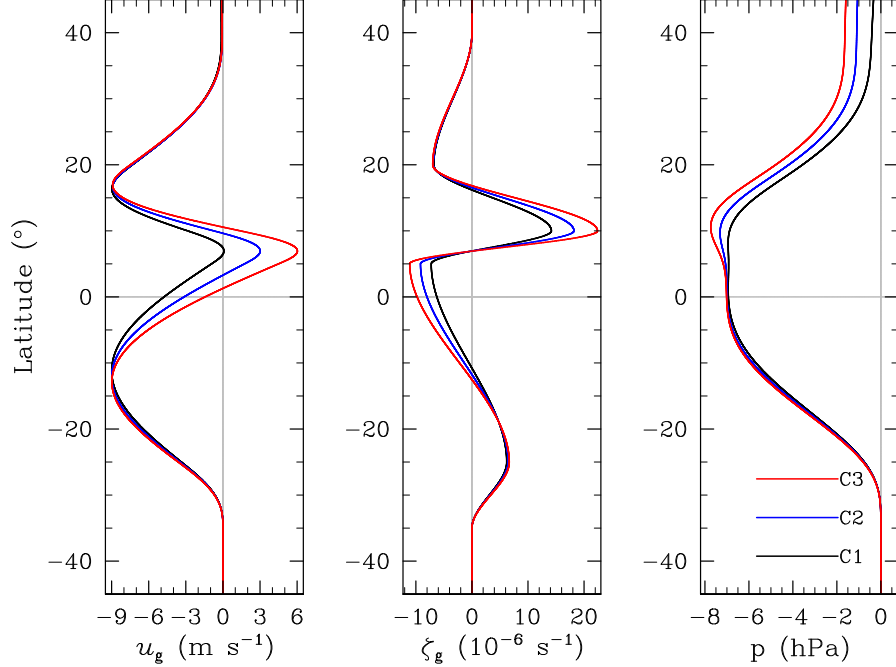


FIG. 5.7. Idealized $u_g(\phi)$, $\zeta_g(\phi)$, $p(\phi)$ fields for the 10° ITCZ displacement set of experiments using (5.54) and the values listed in Table 5.2. C1, C2, and C3 correspond to maximum westerlies of 0, 3, and 6 m s^{-1} respectively.

It turns out that shock-like structures do not appear in the vicinity of 10° if the westerlies are weak ($< 4 \text{ m s}^{-1}$), such as in cases C1 and C2. Therefore, we will focus on the C3 experiment, where the westerlies maximize at 6 m s^{-1} . Figure 5.8 shows the temporal evolution of the boundary layer flow in the C3 run. The four plots of Figure 5.8 show meridional profiles ($-25^\circ \leq \phi \leq 25^\circ$) of the boundary layer zonal wind u , meridional wind v , relative vorticity ζ , and vertical velocity at the top of the boundary layer w for two times: $t = 0$ and 12 days. Remember that the initial v is zero while the initial u is in geostrophic balance with the pressure gradient in the overlying layer. Note that meridional inflow, supergeostrophic/subgeostrophic zonal winds, large Ekman pumping at the top of the boundary layer, and large boundary layer relative vorticity quickly develop, with the establishment of a near steady state around 8–12 days. Such timescales seem reasonable for the formation of the ITCZ, as discussed by Nieto Ferreira and Schubert (1997); Wang and Magnusdottir (2006).

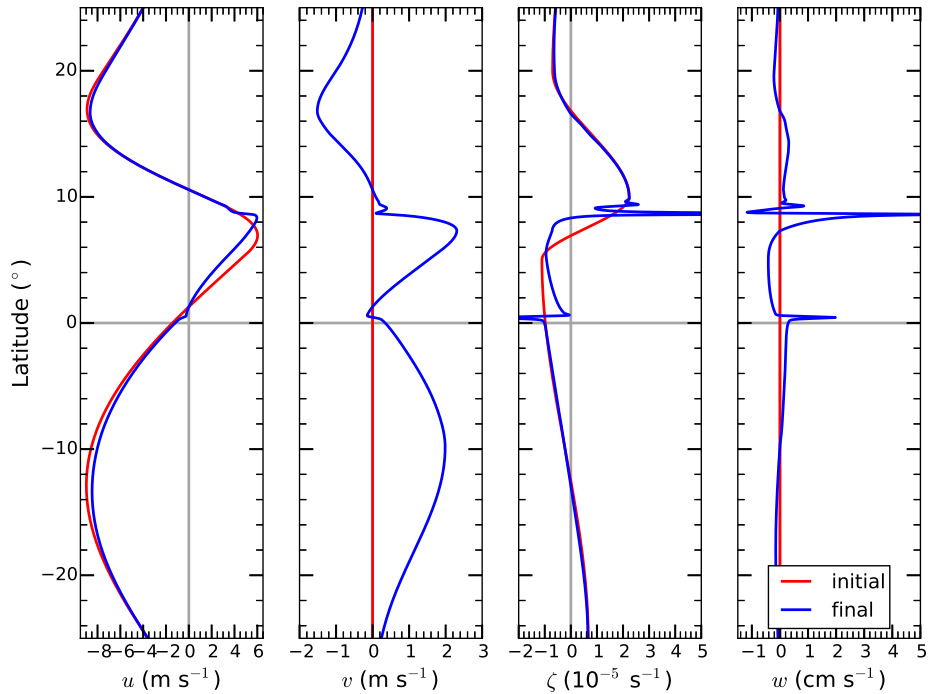


FIG. 5.8. Slab boundary layer model results for the 10° ITCZ displacement C3 forcing case (6 m s^{-1} westerlies). The four plots show the zonal winds $u(\phi, t)$, meridional winds $v(\phi, t)$, relative vorticity $\zeta(\phi, t)$, and vertical velocity at the top of the boundary layer $w(\phi, t)$ for the region $-25^\circ \leq \phi \leq 25^\circ$. The results at the two times $t = 0$ and 12 days are color coded.

Note that a shock-like structure develops a few hundred kilometers north of the meridional location of maximum westerlies. This response is due to the $v(\partial v/a\partial\phi)$ term in the meridional momentum equation. The maximum meridional inflow associated with these supergeostrophic westerlies is approximately 2.3 m s^{-1} . Near this shock, the meridional winds decrease by about 2 m s^{-1} over a 30 km interval, thereby producing a narrow spike in the Ekman pumping at the top of the boundary layer of about 6.0 cm s^{-1} . Associated with this concentrated region of convergence is a relative vorticity sheet, which is almost six times as large ($11.9 \times 10^{-5} \text{ s}^{-1}$) as its initial value ($2.2 \times 10^{-5} \text{ s}^{-1}$). Also note that the easterlies north of the the westerlies never become supergeostrophic, therefore they do not produce shock-like structures, but they do produce weak

boundary layer pumping of $\approx 5 \text{ mm s}^{-1}$. This process is explained as follows: the Coriolis force $2\Omega v \sin \phi$ acts to speed up the zonal winds while the surface drag acts to slow down the easterlies. To form shock-like structures, the zonal flow must be sufficiently subgeostrophic at some point in time to be able to produce strong enough meridional inflow. Therefore, the region south of the ITCZ is slowed down more by the surface drag.

Another region of localized Ekman pumping worth mentioning is the region near the equator, where the Coriolis force approaches zero. In this region the forcing is quite weak, although it does help produce some southerly flow. It acts more like the viscous Burgers' equation (e.g., Heuristic Model II) in that the surface drag tries to overcome the shock. The model tends to produce shock-like structures ($\approx 2 \text{ cm s}^{-1}$ pumping) near the equator even though an ITCZ at the equator is rarely observed in nature. Also, the vorticity sheet associated with this shock-like structure is anticyclonic in the northern hemisphere, which seems to be unrealistic. However, observations such as those shown by Liu and Xie (2002) suggest that localized low-level convergence near the equator is more common than previously thought, especially in regions such as the Atlantic and eastern Pacific, as illustrated in Fig. 5.9. Since this convergence does not typically couple to convection it is possible that the atmospheric thermodynamic conditions and Ekman upwelling of cold ocean water in this region helps to suppress convection, as discussed by Charney (1968, 1971); Pike (1971, 1972).

Table 5.3 shows the next set of experiments, which test the sensitivity of shock-like formation to the meridional location of the forcing: 0° (d00), 5° (d05), 10° (d10), and 15° (d15). Each test case considers a $u_g(\phi)$ profile that has maximum westerlies of 6 m s^{-1} , as done in the previous test case C3 at 10° . Note that test case d10 is the same as C3 in Table 5.2. Figure 5.10 shows $\zeta_g(\phi)$ along with its associated fields $u_g(\phi)$ and $p(\phi)$ for the three test cases d05, d10, and d15, with the parameter values listed in Table 5.2. The $p(\phi, t)$ field illustrates that as the ITCZ is

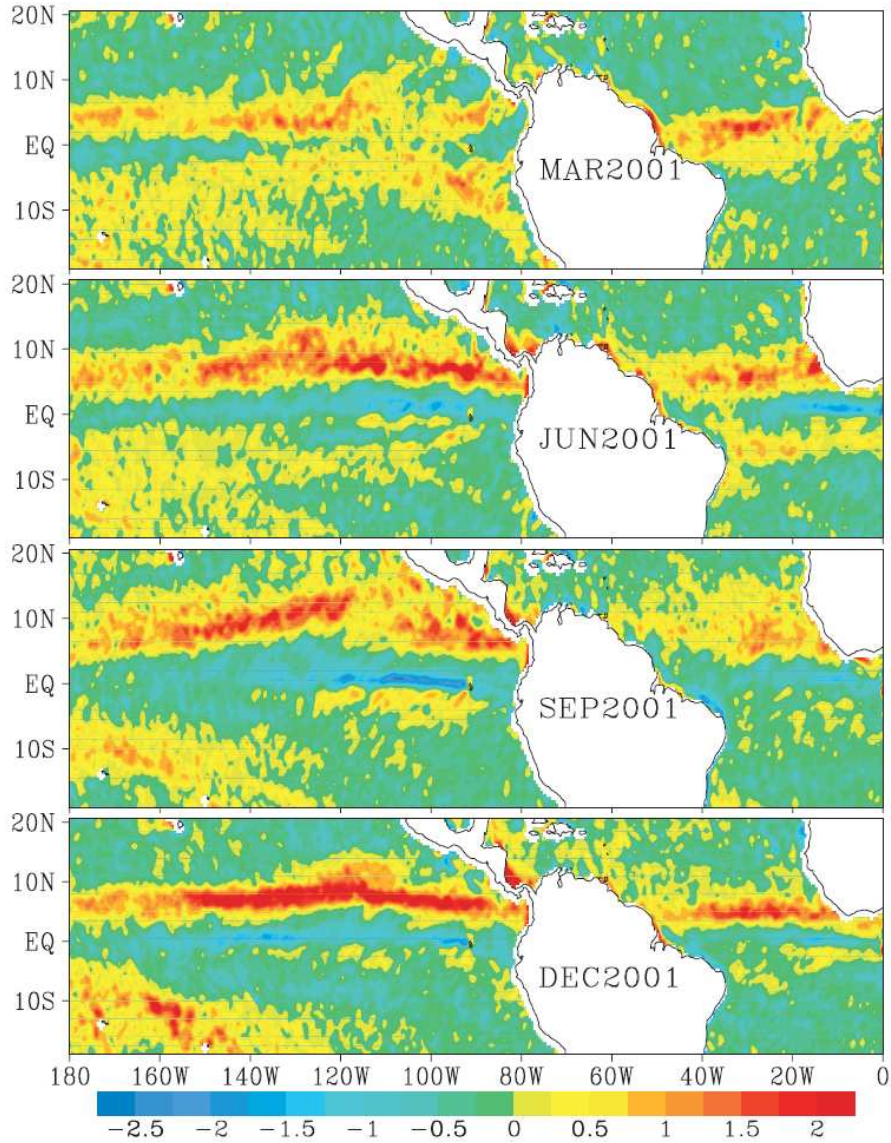


FIG. 5.9. Surface wind convergence (10^{-5} s^{-1}) from QuikSCAT for the months of March, June, September, and December 2001. From Liu and Xie (2002).

displaced poleward, the low pressure minimum north of the equator exceeds that of the minimum at the equator. As we will see, this does not necessarily mean that ITCZ shock-like structures are stronger as the ITCZ is displaced poleward.

Figure 5.11 illustrates the slab boundary layer model $u(\phi, t)$, $v(\phi, t)$, $\zeta(\phi, t)$, and $w(\phi, t)$ fields at $t = 12$ days for the three ITCZ displacements: 5° (d05), 10° (d10), and 15° (d15). Shock-like structures form in the initially cyclonic vorticity region in experiments d05 and d10, but not

so much in d15. The determining factor involves the region that initially had cyclonic relative vorticity. If this region's cyclonic relative vorticity contains a vorticity sheet significantly stronger than the initial cyclonic vorticity and a collocated narrow spike in Ekman pumping, then it has produced ITCZ shock-like structures where we expect them. Experiment d15 does indeed produce shock-like structures near the equator, but this is not the region where the initial relative vorticity was cyclonic. Also, the vorticity sheet associated with the equatorial spike in Ekman pumping is anticyclonic in the northern hemisphere, which seems to be unrealistic. A fourth experiment where the initial cyclonic vorticity region is centered about 20° (d20, not shown) also failed to produce shock-like structures in the initially cyclonic vorticity region. These results suggest that ITCZ shocks are most common close to the equator, $-15^\circ < \phi < 15^\circ$. The reasons for this result have to do with the delicate balance between the forcing (pressure gradient force), the Coriolis force, and the surface drag throughout the time period before a steady state is reached, as discussed before.

TABLE 5.3. Information about the second set of experiments at 5° , 10° , and 15° .

Displacement	ϕ_1 ($^\circ$)	ϕ_2 ($^\circ$)	ϕ_3 ($^\circ$)	ϕ_4 ($^\circ$)	ϕ_5 ($^\circ$)	ϕ_6 ($^\circ$)	ζ_1 (10^{-6} s^{-1})	ζ_2 (10^{-6} s^{-1})	ζ_3 (10^{-6} s^{-1})	ζ_4 (10^{-6} s^{-1})
d05	-40	-30	0	5	15	35	6.77	-11.07	22.40	-6.90
d10	-35	-25	5	10	20	40	6.66	-11.10	22.40	-7.00
d15	-30	-20	10	15	25	45	6.55	-11.13	22.50	-7.10

Figure 5.11 also shows the $u(\phi, t)$, $v(\phi, t)$, $\zeta(\phi, t)$, and $w(\phi, t)$ fields at $t = 12$ days for the d05 run. Shock-like structures develop in a similar manner as in d10, with meridional inflow, supergeostrophic/subgeostrophic zonal winds, large Ekman pumping at the top of the boundary layer, and large boundary layer relative vorticity. The boundary layer pumping is a bit smaller in magnitude when compared to d10, and that is due to the weaker meridional inflow produced by the forcing. It is interesting to note that the steady-state westerlies just south of the narrow vorticity sheet are about 2 m s^{-1} slower than those in the d10 run. There is still a region of supergeostrophic

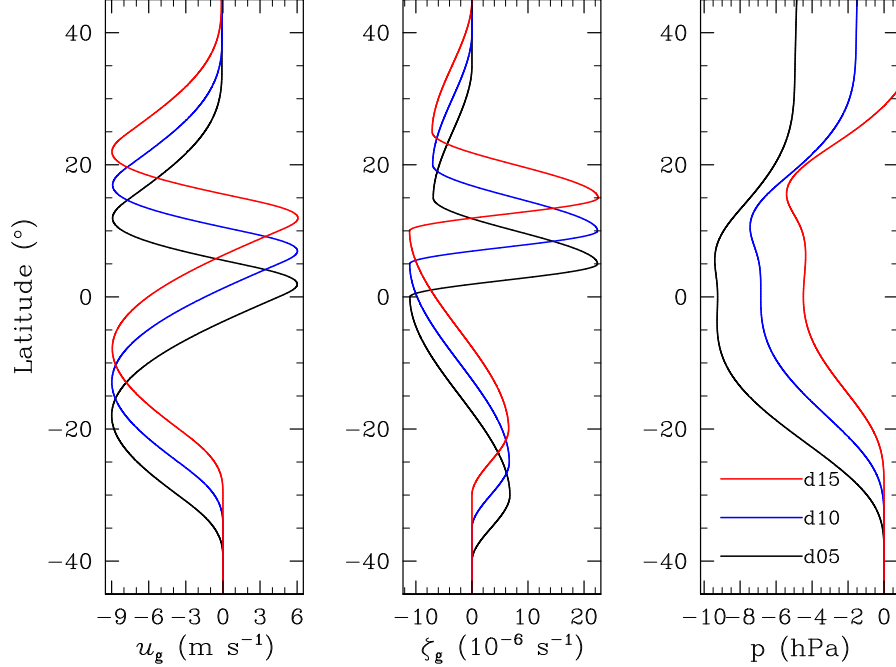


FIG. 5.10. Idealized $u_g(\phi)$, $\zeta_g(\phi)$, $p(\phi)$ fields for the 10° ITCZ displacement set of experiments using (5.54) and the values listed in the last three rows d05, d10, and d15 listed in Table 5.3.

flow, but the region of subgeostrophic flow is broader than the d10 run. This result is due to the fact that the forcing goes to zero as one approaches the equator, allowing surface drag to be more efficient in slowing down the horizontal winds in this case.

As we discussed in the Heuristic Model sections, characteristics are very helpful in understanding the development of shocks and shock-like structures. Since the form of the slab boundary layer model used here contains horizontal diffusion, we do not have a hyperbolic system with associated families of characteristics. For simplicity, we limit our analysis to trajectories rather than characteristics. Figure 5.12 shows the trajectories in the (ϕ, t) -plane along with contours of the zonal and meridional winds $u(\phi, t)$ and $v(\phi, t)$ for the 10° (d10) experiment. The trajectories were computed by numerically integrating $a(d\phi/dt) = v$ using the same 5 s time step used for the numerical solutions of (5.1) and (5.6). To aid in our interpretation of the trajectories we have the Lagrangian

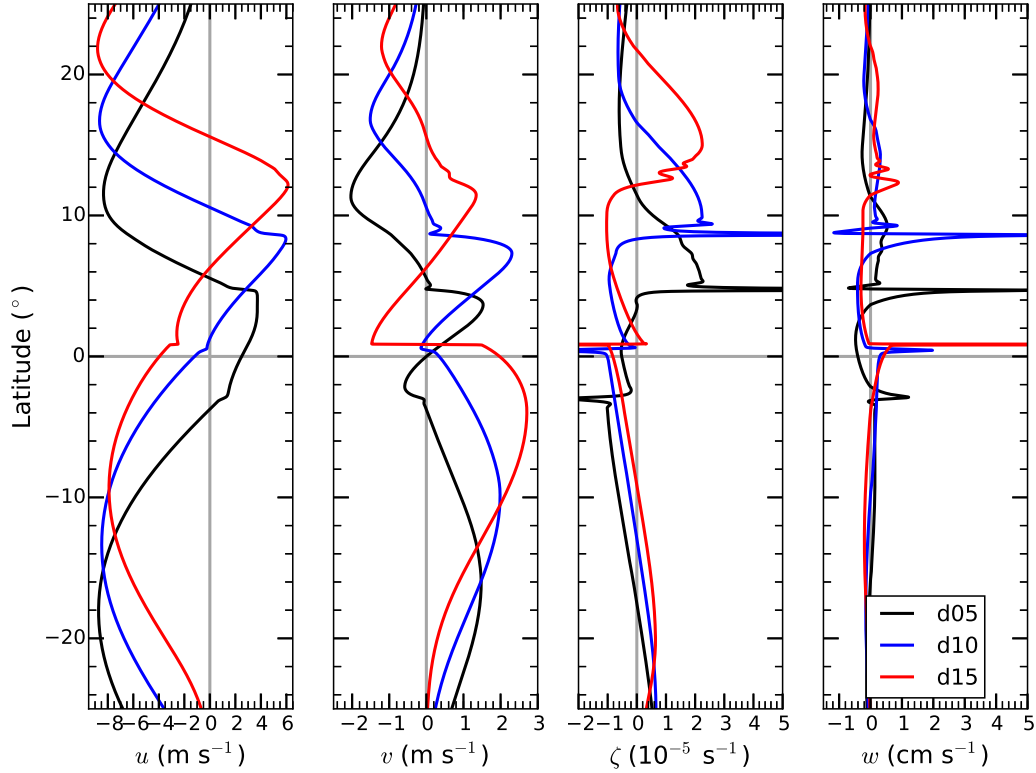


FIG. 5.11. Slab boundary layer model results for the 5° (d05), 10°(d10), and 15° (d15) ITCZ displacements (6 m s⁻¹ westerlies). The four plots show the zonal winds $u(\phi, t)$, meridional winds $v(\phi, t)$, relative vorticity $\zeta(\phi, t)$, and vertical velocity at the top of the boundary layer $w(\phi, t)$ for the region $-25^\circ \leq \phi \leq 25^\circ$. The results shown are when $t = 12$ days and the different displacements are color coded.

form of (5.1)

$$\frac{du}{dt} = \left(\frac{w(1-\alpha)(u-u_g) - c_D U u}{h} \right) + \left(2\Omega \sin \phi + \frac{u \tan \phi}{a} \right) v + K \frac{\partial}{\partial \phi} \left(\frac{\partial(u \cos \phi)}{a \cos \phi \partial \phi} \right), \quad (5.55)$$

and the Lagrangian form of (5.6)

$$\frac{dv}{dt} = \left(\frac{w(1-\alpha) - c_D U}{h} \right) v - \left(2\Omega \sin \phi + \frac{(u+u_g) \tan \phi}{a} \right) (u-u_g) + K \frac{\partial}{\partial \phi} \left(\frac{\partial(v \cos \phi)}{a \cos \phi \partial \phi} \right), \quad (5.56)$$

where $(d/dt) = (\partial/\partial t) + v(\partial/a\partial\phi)$ is the derivative following the meridional flow, i.e., the derivative along trajectories defined by $a(d\phi/dt) = v$. The trajectories are horizontal for the first few hours since the meridional flow is negligible there, and they are always horizontal near the equator since the meridional flow is negligible there. As the meridional flow increases, the trajectories flow toward the convergence regions, but note that they are not straight lines. Instead, they curve toward or away from the convergence regions. This is reminiscent of the Heuristic Model II results in that surface drag acts to curve the characteristics (or trajectories) away from the convergence regions.

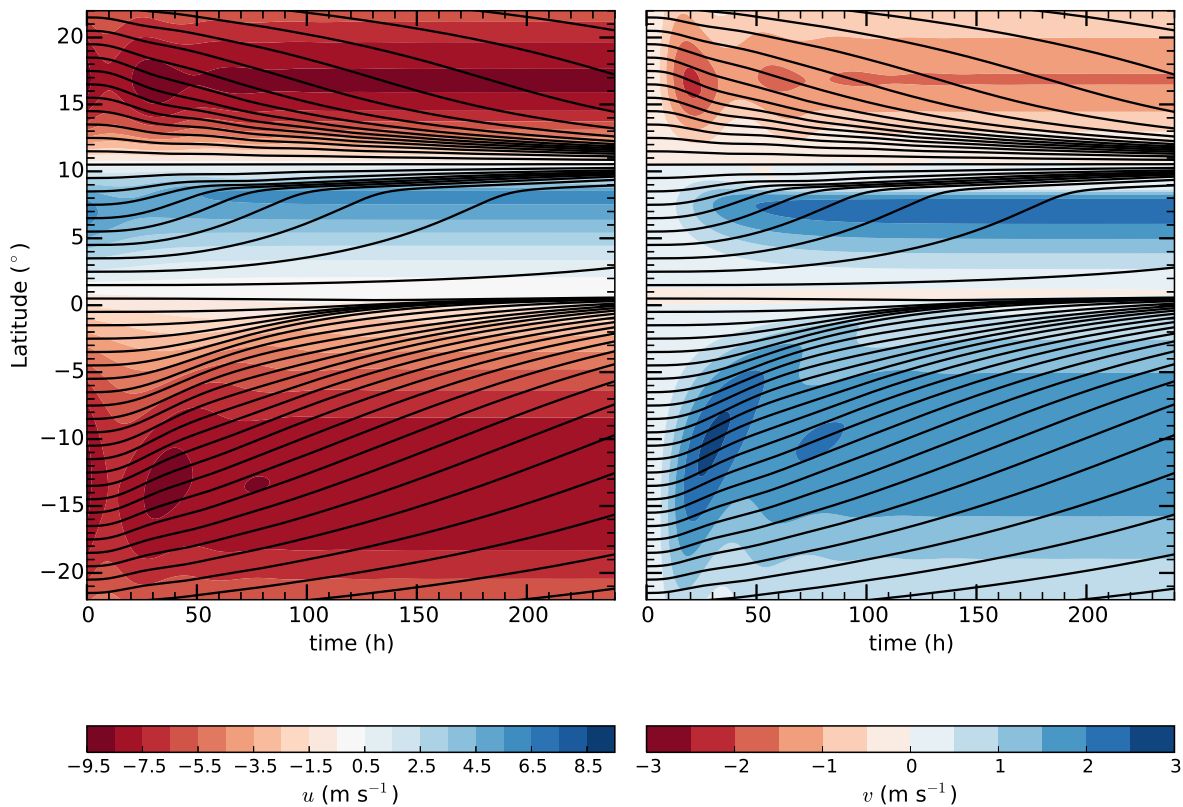


FIG. 5.12. Trajectory curves in the (ϕ, t) plane for the d10 forcing case in the two plots, along with contours of the zonal winds u (left) and meridional winds v (right).

For example, the trajectories a couple of degrees north of the equator experience an increase in meridional flow as they move northward until they are just south of 8° , where their meridional flow decreases and they converge with the other trajectories, producing a shock-like structure after

about 72 h (Fig. 5.12, right panel). When these trajectories are south of 8° their zonal winds are subgeostrophic (Fig. 5.12, left panel), causing $(dv/dt) > 0$ due to $(u - u_g) < 0$ and $\sin \phi > 0$ in the Coriolis terms in (5.56), despite the presence of meridional surface drag. Once these trajectories are north of about 8° their zonal winds become supergeostrophic, which along with the meridional surface drag, act to decrease v quickly, as shown in (5.56). This quick decrease in v signifies the spike in boundary layer pumping, shown in Fig. 5.13. We must emphasize the importance of the Burgers' term $v(\partial v / a \partial \phi)$ in the first 10 hours, which is when the zonal flow is decreasing with time along trajectories. The zonal surface drag plays a vital role in slowing down the zonal winds, helping drive meridional inflow down the pressure gradient. This is why we believe shocks are features confined to the boundary layer.

Taking a look at the isolines of u in Figure 5.12, we see that they behave quite differently than meridional winds along trajectories. The zonal winds weaken along trajectories for the first 10 h due to zonal surface drag, then begin to increase in magnitude due to the $\sin \phi$ factors in the Coriolis terms in (5.57). As the trajectories move toward the convergence regions their zonal winds decrease in magnitude quickly due to both the quick weakening of v in the Coriolis terms in (5.57) and the presence of zonal surface drag. In this region there forms a narrow vorticity sheet along with a spike in Ekman pumping, as illustrated in Figure 5.13.

In Figure 5.13, the boundary layer relative vorticity ζ and pumping at the top of the boundary layer w are shown. As we discussed before in the Heuristic Model sections, the vorticity and pumping increase very quickly along trajectories. There are three main regions of large vorticity—near the equator, 8° - 10° , and 11° - 13° . Despite this, there is only one region that is collocated with significant Ekman pumping, 8° - 10° . It is also interesting to note that the spike in ζ is not exactly collocated with the peak in Ekman pumping. The pumping is located slightly south of the peak in

ζ and where the trajectories come together. This is similar to what was observed in the results of Williams et al. (2013).

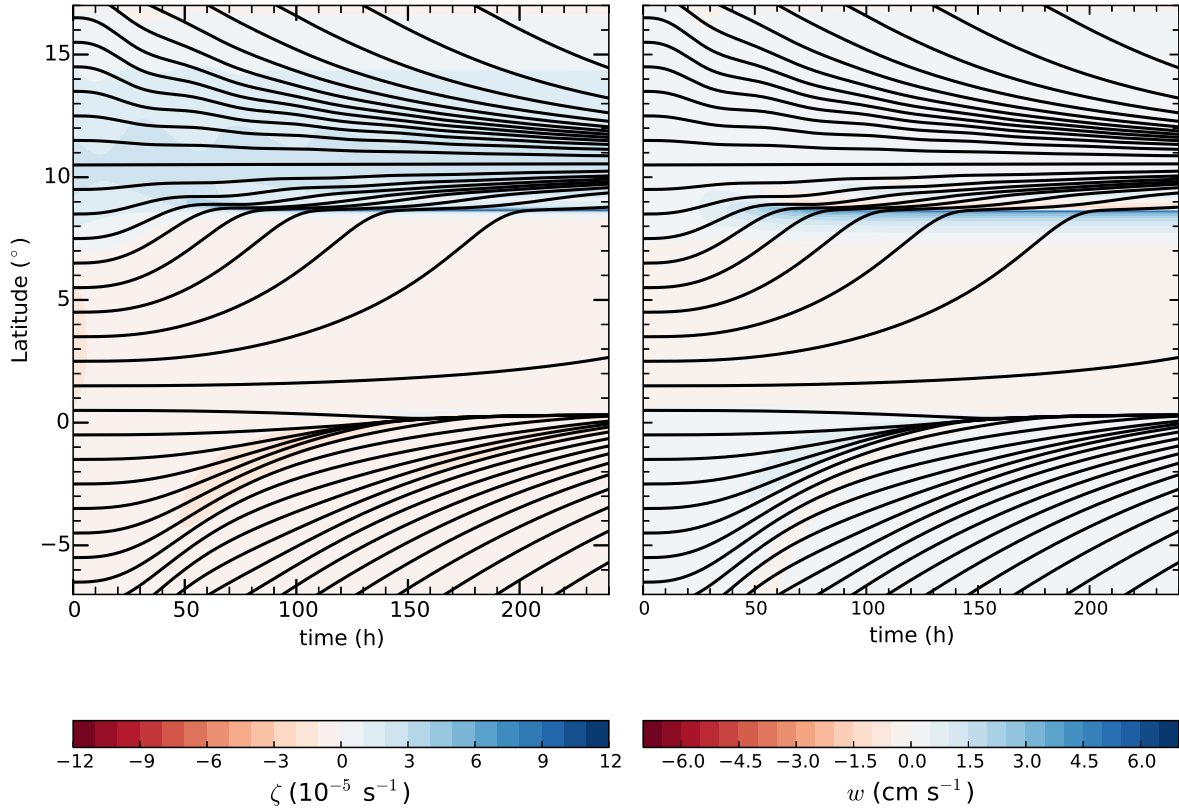


FIG. 5.13. Trajectory curves in the (ϕ, t) plane for the d10 forcing case in the two plots, along with contours of the relative vorticity ζ (left) and vertical velocity w (right).

In Figure 5.14, we show the trajectories as well as isolines of the absolute angular momentum m . As important relation to consider when interpreting this figure is

$$a \cos \phi \frac{du}{dt} = \frac{dm}{dt} + (2\Omega a \cos \phi + u) v \sin \phi. \quad (5.57)$$

In the region a few degrees north of the equator, m decreases along trajectories despite the fact that u increases after the first 10 hours. That is because the strong meridional inflow causes in the second term on the right hand side of (5.57) to be larger than $a \cos \phi (du/dt)$. In the regions south of

the equator and north about 10° m increases along trajectories along with u because the the second term on the right hand side of (5.57) is negative and is larger due to the $\cos \phi$ and $\sin \phi$ factors. South of the equator there are northward trajectories and a second shock-like structure appears near the equator. This shock-like structure takes about 100 h to become established. It remains to be seen how realistic this equatorial shock-like structure is, but it causes information coming from south of the equator to never cross it. North of the 10° a third shock-like structure tries to develop. But, as shown in Figure 5.13, there is no narrow vorticity or boundary layer pumping associated with it.

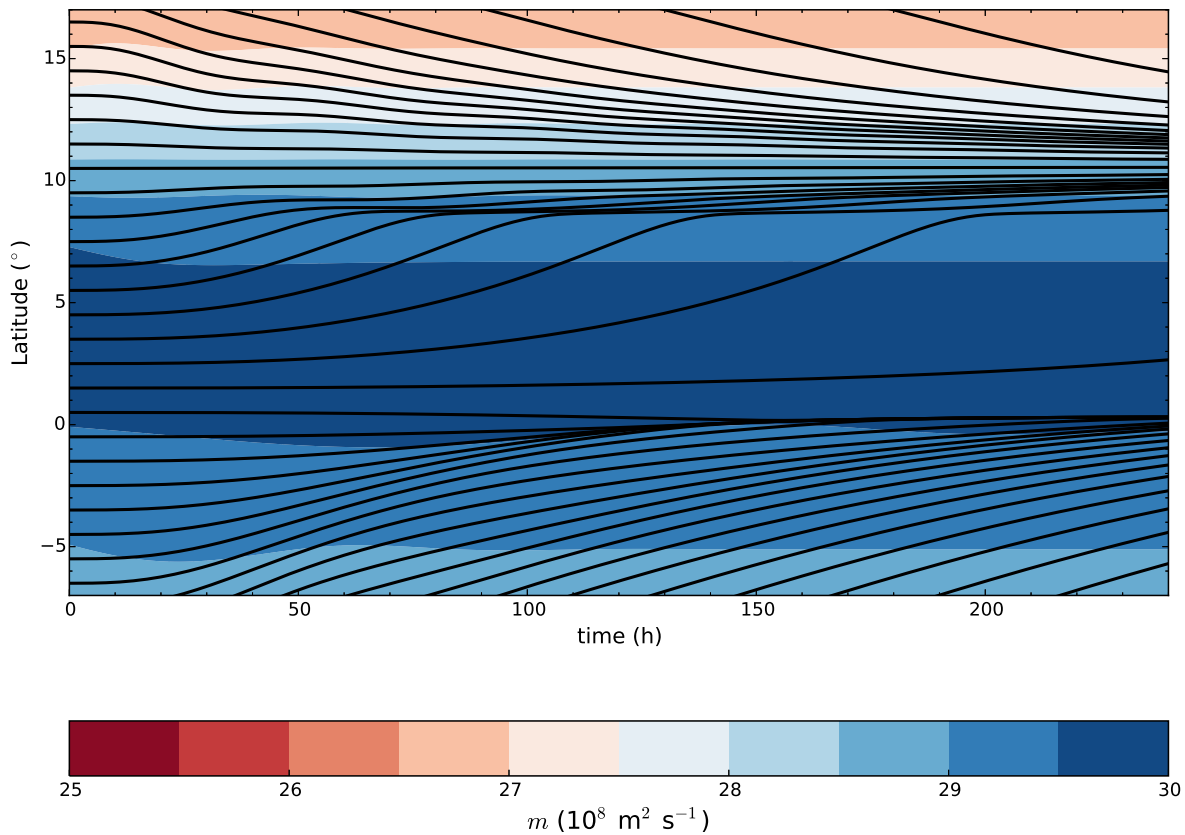


FIG. 5.14. Trajectory curves in the (ϕ, t) plane for the d10 forcing case in the two plots, along with contours of the absolute angular momentum m .

5.7. NUMERICAL SIMULATION OF ITCZ SHOCKS - YOTC REANALYSIS FORCING

Thus far we have analyzed the slab boundary layer model response to a variety of idealized $u_g(\phi)$ forcings. We would like to force the model with reanalysis fields during the contrasting months of July and March during Year of Tropical Convection (YOTC) reanalysis to investigate if our idealized zonally symmetric model can reproduce the dynamical aspects of the ITCZ. We shall use the slab boundary layer equations (5.1), (5.2), and (5.6) with the same constants as those used in the previous section but with the boundary conditions $u = v = 0$ at $\phi = \pm\pi/4$. We run the model at two horizontal resolutions: 100 m (high) and 28 km (low). The low resolution run is meant to emulate a resolution consistent with operational models such as the one used to produce the YOTC reanalysis fields. We also neglect one of the Ekman suction terms, $w(1 - \alpha)(u - u_g)$. This simplification allows us to prescribe one field, which is the pressure gradient field felt in the boundary layer. Experience from other runs (not shown for brevity) convinces us that this Ekman suction term tends to be small (differences in u, v on the order of $0.5\text{--}1 \text{ m s}^{-1}$). We compute the boundary layer pressure gradient by using the 950 hPa geopotential field from YOTC. Also, we switch on the pressure gradient forcing with time using the separable function

$$\mathcal{T}(t) = 1 - (1 + \gamma t) e^{-\gamma t}, \quad (5.58)$$

which is plotted previously in Figure 4.5. We use the constant $\gamma = (12 \text{ h})^{-1}$. This switch on function is used to avoid erratic oscillations that occur when the forcing is switched on too quickly. Also, the derivative of the geopotential field is quite erratic, therefore we use only ocean data points and smooth its derivative with the NCAR Command Language built-in cubic spline function `csa1xd`. YOTC is a global reanalysis product spanning the time period of May 2008–April 2010 that uses four-dimensional variational data assimilation at a horizontal resolution of 0.25 degrees (28 km,

July 2008 Geopotential Height (90W–150W)

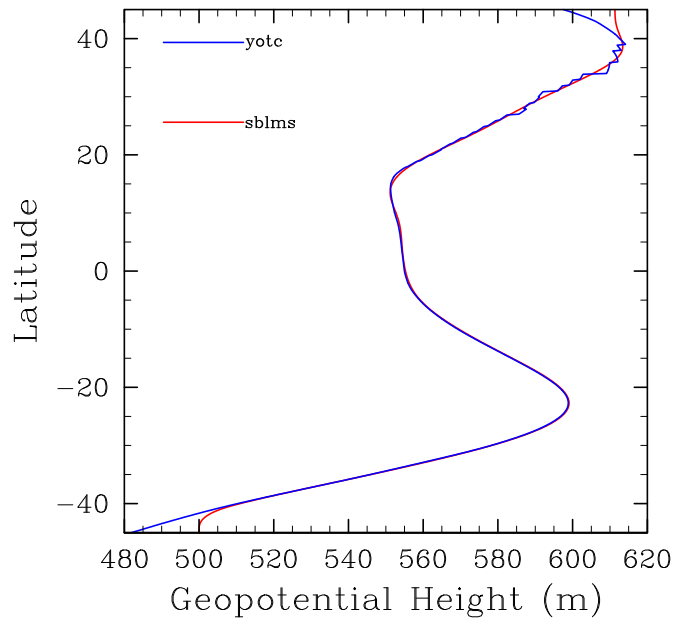


FIG. 5.15. YOTC July 2008 monthly and 90W–150W zonally averaged 950 hPa geopotential field (blue curve) and the idealized geopotential field used in the slab boundary layer model (red curve). The idealized geopotential was computed using the cubic spline interpolating NCAR Command Language function `csa1xd`.

T799), with 91 vertical levels. We choose the model fields outputted at a horizontal resolution of 0.25 degrees (28 km) for direct comparisons to the low resolution slab boundary layer model fields.

5.7.1. JULY 2008

July 2008 was a relatively weak El Niño month in the 90W–150W (Niño 3) region, as illustrated previously in Fig. 3.3. Figure 5.15 shows the July 2008 monthly and zonally averaged (90W–150W) geopotential field as seen before and after using a cubic spline interpolation, with appropriate treatment of the domain boundaries to satisfy the boundary conditions. There is low pressure in the tropics and high pressure in the subtropics due to the summertime subtropical anticyclones. We should note that even though the lowest pressure is located near 45S, the ITCZ is expected to form where the lowest pressure occurs in the tropics, about 10°–15°.

Figure 5.16 illustrates both high (sblm-hr) and low resolution (sblm-lr) slab boundary layer model u , v , ζ , and w fields when they reach a quasi steady state as well as the July 2008 monthly and 90W–150W zonally averaged u , v , ζ , and w YOTC fields (yotc). YOTC does not output the w field, but instead provides the horizontal divergence δ field. We use the formula $w = -h\delta$ with $h = 1$ km for consistency with the slab model. Overall, the slab boundary layer model qualitatively agrees with the monthly averaged YOTC fields, although the YOTC wind fields tend to be larger in magnitude while the relative vorticity and vertical velocity at the top of the boundary layer tend to be larger in the slab model. The 100 m model experiment shows a much more confined and intense Ekman pumping region. Also, there is a vorticity sheet seen in the 100 m run which is not seen in the 28 km run or in the YOTC vorticity field. These differences, albeit not surprising, are intended to highlight transient dynamical processes in the ITCZ such as Burgers' shock-like structures that are not captured as well in the YOTC or sblm-lr fields. It would be more practical to compare the slab boundary layer model to the YOTC fields if it were not zonally symmetric, so that the ITCZ could be influenced by zonal variations and breakdown. The timescale for breakdown is a few days to 3 weeks, as discussed in Wang and Magnusdottir (2006). It takes about 2 days for the pressure forcing to be sufficiently switched on ($> 90\%$) and about 4 days until the peak in Ekman pumping occurs (2.3 m s^{-1}), so that the approximate timescale for ITCZ shock formation is about 2 days. Since the model fields reach a quasi steady state after about 8-10 days, it is likely that the ITCZ would break down after the shock has occurred and either before or after a quasi steady state has been reached. Also, the timescale for shock formation of 2 days is in line with the results in Heuristic Model II.

Another interesting feature of the slab boundary layer model runs is the asymmetrical response of the meridional velocity. The pressure gradient force is about the same magnitude on either side

July 2008 (90W-150W)

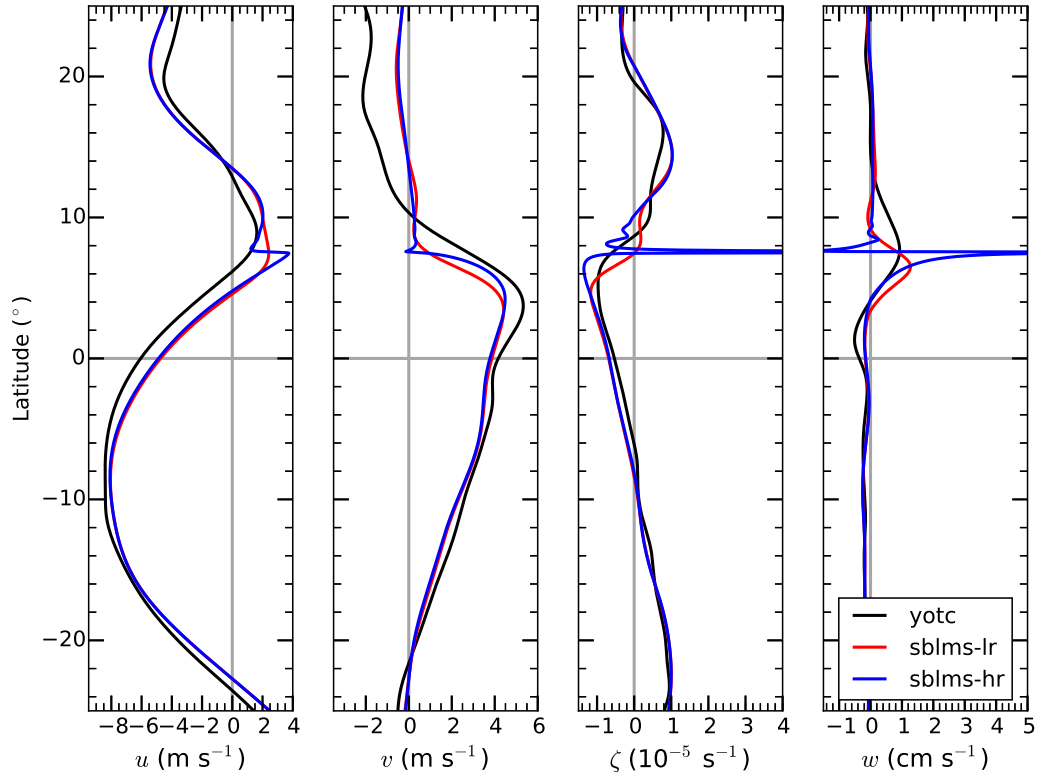


FIG. 5.16. High (sblm-hr) and low resolution (sblm-lr) slab boundary layer model solutions after 12 days against the corresponding YOTC July 2008 monthly and 90W-150W zonally averaged 950 hPa fields. The four plots show the zonal winds u , meridional winds v , relative vorticity ζ , and vertical velocity at the top of the boundary layer w for the region $-25^{\circ} \leq \phi \leq 25^{\circ}$. The model runs are forced solely by the YOTC July 2008 monthly and 90W-150W zonally averaged 950 hPa pressure gradient force. Refer to the text for more details.

of the two equatorial minima in geopotential (Figure 5.16, -5° – 15°), but there are small asymmetries in between the two minima as well. It is possible that these small asymmetries in the pressure gradient force are the main contributors to the asymmetries in v in the slab model, but it is also possible that the Coriolis force plays a role since it is anisotropic. This asymmetrical meridional wind response is also in the YOTC meridional winds, but it is not as dramatic. One possible explanation for this discrepancy between the slab model and YOTC is that there are nonlinear eddy contributions that are neglected in the slab boundary layer model since it is zonally symmetric. For

example, the eddy term $u(\partial v/a\partial\lambda)$ is large in the eastern ocean basins, where the subtropical highs help support strong meridional inflow. In particular, there is larger meridional inflow in the summer hemisphere since the subtropical highs are typically stronger (McNoldy et al. 2004). Figure 5.17 confirms that the subtropical highs were stronger during July 2008 in the summer hemisphere over the eastern Pacific. Another possible explanation for the discrepancies in the northerlies is the uncertainty in the pressure gradient field over land (there is land strictly north of about 12°).

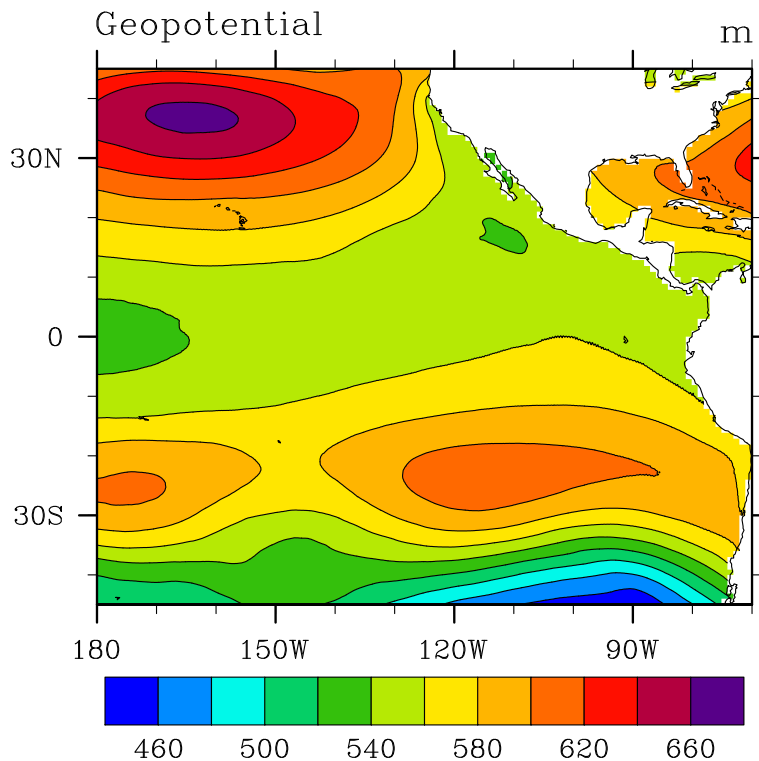


FIG. 5.17. YOTC July 2008 monthly averaged 950 hPa geopotential field (m) over the eastern Pacific Ocean. Note that the subtropical high in the summer hemisphere is significantly stronger than the subtropical highs in the winter hemisphere.

5.7.2. MARCH 2009

March 2009 was a month with modest La Niña conditions in the eastern and central Pacific (Niño 3 region), as illustrated before in Fig. 3.8. Hayes et al. (1989); Lietzke et al. (2001); Zhang (2001); Gu et al. (2005) have illustrated that double ITCZs are quite common during La Niña

and neutral conditions. In fact, the YOTC low-level 950 hPa divergence field does show a double ITCZ structure during March 2009. We would like to see if the slab boundary layer model can also reproduce a double ITCZ in the form of Ekman pumping on either side of the equator. In Figure 5.18, we illustrate the YOTC monthly and zonally averaged (90W–150W) geopotential field alongside the smoothed geopotential field used in the model. There is a broad low pressure region that is approximately symmetric about the equator within about 25 degrees of the equator. One might speculate that with only one pressure minimum there should only be one ITCZ, but as we will see, the Ekman pumping has two primary peaks on either side of the equator in both the slab boundary layer model and the YOTC reanalysis. Figure 5.19 shows the high and low

March 2009 Geopotential Height (90W–150W)

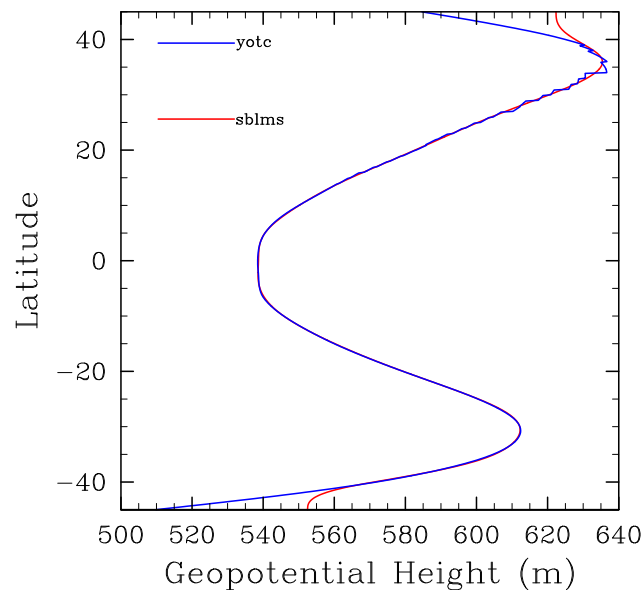


FIG. 5.18. YOTC March 2009 monthly and 90W–150W zonally averaged 950 hPa geopotential field (blue curve) and the idealized geopotential field used in the slab boundary layer model (red curve). The idealized geopotential was computed using the cubic spline interpolating NCAR Command Language function `csa1xd`.

resolution model run u , v , ζ , and w fields forced by the smoothed geopotential field shown in Figure 5.18 alongside the March 2009 monthly and zonally averaged YOTC u , v , ζ , and w fields. The slab boundary layer model horizontal winds are comparable to the YOTC zonal winds except

near the equator where the slab model tends to produce weaker easterlies in the 28 km run (up to 3 m s^{-1} weaker), and produces weak westerlies in the high resolution run (up to 5 m s^{-1} difference). Also, north of about 7° the model tends to have weaker northerlies, just as seen in the July 2008 model runs. Despite these discrepancies, the model does form a double ITCZ structure, with two peaks in cyclonic vorticity and Ekman pumping on either side of the equator, at about 3° . These fields tend to be narrower and more intense in the model experiments, just like the July 2008 runs. Another result worth mentioning is that the Ekman suction on the equator is weaker in the low and high resolution model runs compared to the YOTC w . Typically, the double ITCZ is described as having a cold SSTs in between the two ITCZs. Both the subsidence and cold water tend to stabilize the boundary layer, resisting the formation of an ITCZ on the equator and possibly further enhancing this subsidence.

5.7.3. MARCH 2010

Figure 5.20 illustrates the YOTC monthly and 90W–150W zonally averaged geopotential field alongside the smoothed geopotential field used in the model. March 2010 was characterized by modest El Niño conditions in the eastern and central Pacific (Niño 3 region), as illustrated previously in Fig. 3.9. Once again, studies such as Hayes et al. (1989); Lietzke et al. (2001); Zhang (2001); Gu et al. (2005) have illustrated that a single ITCZ just north of or on the equator is commonplace during El Niño conditions, mainly due to warmer SSTs on the equator. Just like March 2009, there is a broad low pressure region that is approximately symmetric about the equator within about 25 degrees of the equator. Therefore it would be surprising to see different results than those from March 2009.

The high and low resolution model u , v , ζ , and w fields are shown in Figure 5.21 alongside the March 2010 monthly and zonally averaged YOTC fields. The slab boundary layer model zonal

March 2009 (90W-150W)

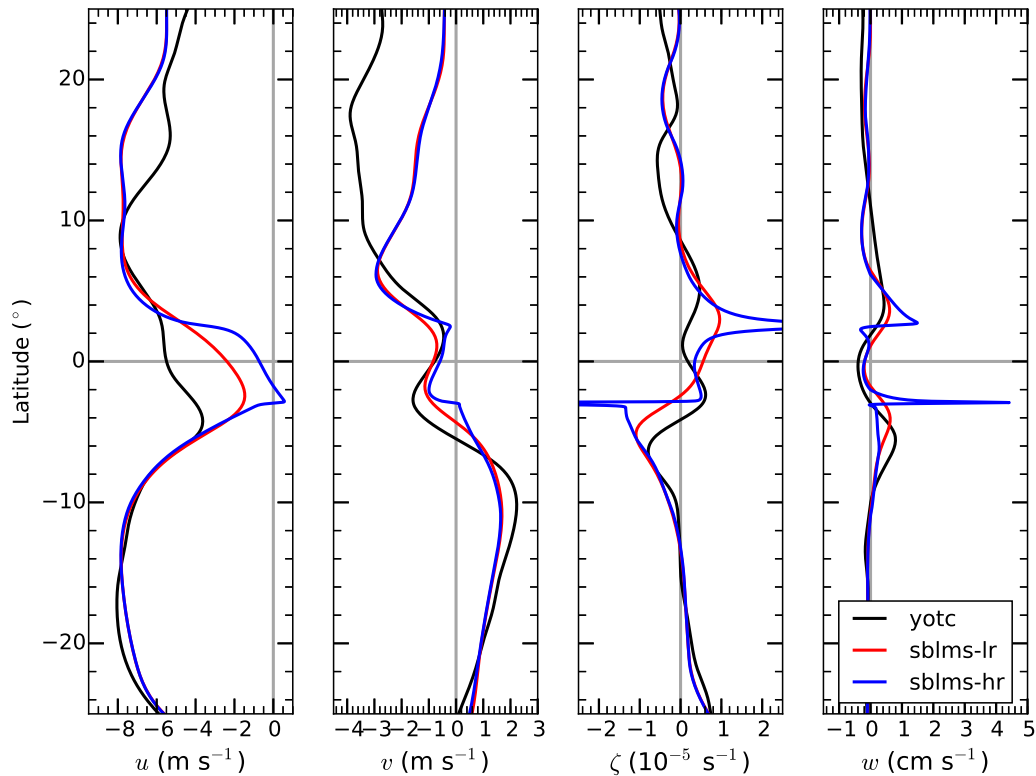


FIG. 5.19. High (sblm-hr) and low resolution (sblm-lr) slab boundary layer model solutions after 12 days against the corresponding YOTC March 2009 monthly and 90W–150W zonally averaged 950 hPa fields. The four plots show the zonal winds u , meridional winds v , relative vorticity ζ , and vertical velocity at the top of the boundary layer w for the region $-25^\circ \leq \phi \leq 25^\circ$. The model runs are forced solely by the YOTC March 2009 monthly and 90W–150W zonally averaged 950 hPa pressure gradient force. Refer to the text for more details.

winds are comparable to the YOTC zonal winds except in the northern hemisphere north of the peak Ekman pumping and near the equator. Near the equator the 100 m slab model once again tends to produce weaker easterlies of up to 2 m s^{-1} , similar to the behavior in the March 2009 runs. North of the peak Ekman pumping the slab model runs produce stronger easterlies (up to 3 m s^{-1}) than in YOTC. The meridional winds are once again weaker north of the ITCZ for the slab model runs. The model does agree with YOTC in producing a single ITCZ structure, with a peak

March 2010 Geopotential Height (90W–150W)

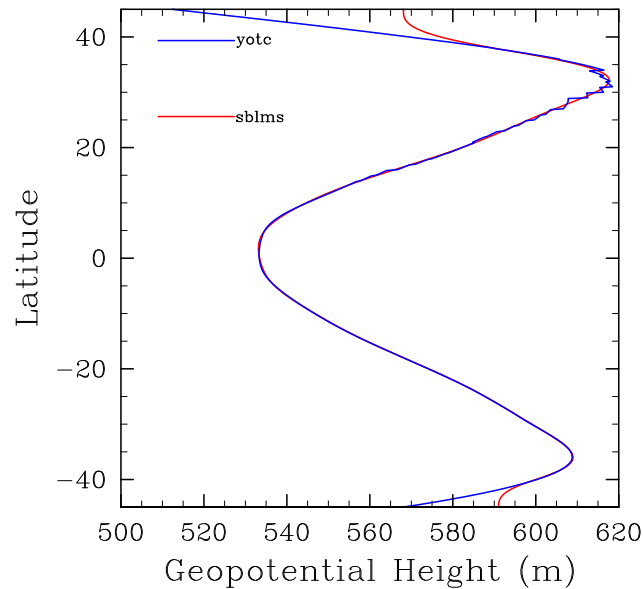


FIG. 5.20. YOTC March 2010 monthly and 90W–150W zonally averaged 950 hPa geopotential field (blue curve) and the idealized geopotential field used in the slab boundary layer model (red curve). The idealized geopotential was computed using the cubic spline interpolating NCAR Command Language function `csa1xd`.

in cyclonic vorticity and Ekman pumping around 4° . Once again these fields tend to be narrower and stronger in the model when compared to the YOTC fields.

It is quite surprising that the slab boundary layer model “correctly” produces a single ITCZ given the nearly symmetric structure (within 25 degrees of the equator) of the geopotential field shown in Fig. 5.20. This implies that small asymmetries in the pressure gradient field can make a significant difference in where the ITCZ will form. Even though the slab boundary layer model has no explicit information about the thermodynamics, it has implicit information about the temperature gradient since the temperature gradient affects the structure of the pressure gradient (Lindzen and Nigam 1987). Also, the location of the minimum in easterlies (or maximum in westerlies for the sblm-hr runs) seems to be quite telling for whether a single or double ITCZ will be produced. If this easterly minimum (or westerly maximum) is north of the equator, a single ITCZ north of

the equator seems to be favored while if this zonal wind minimum is south of the equator, a double ITCZ seems to be favored.

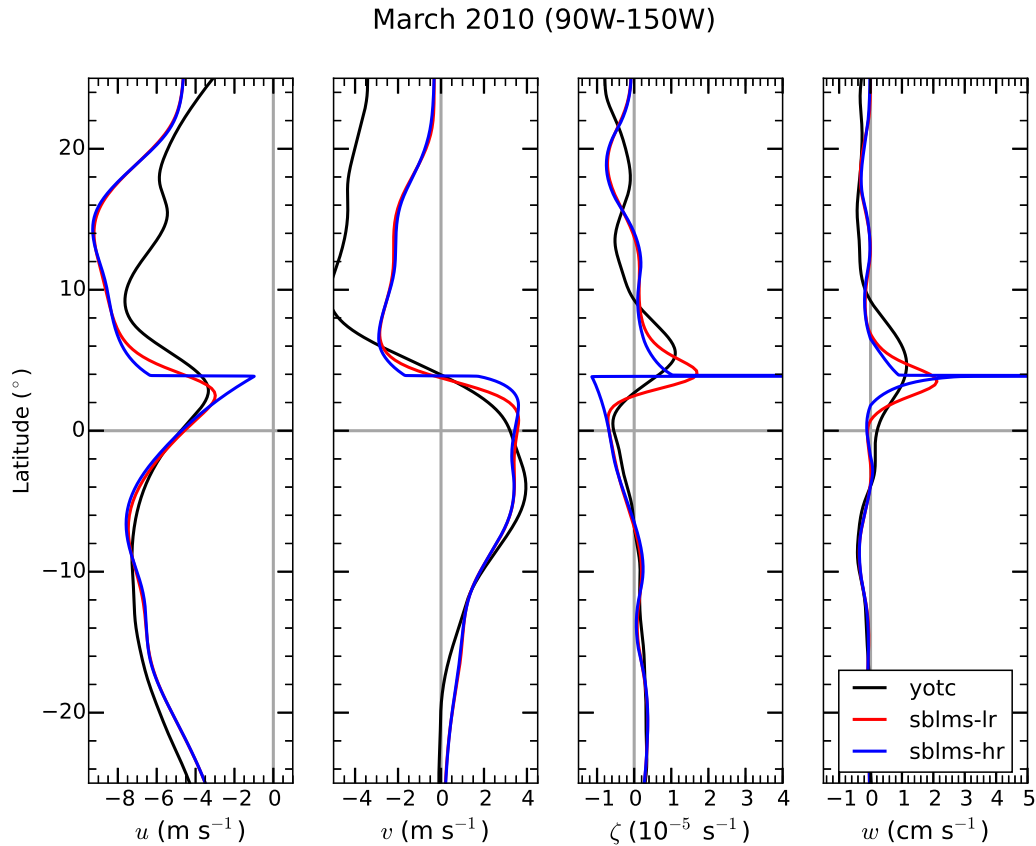


FIG. 5.21. High (sblm-hr) and low resolution (sblm-lr) slab boundary layer model solutions after 12 days against the corresponding YOTC March 2010 monthly and 90W-150W zonally averaged 950 hPa fields. The four plots show the zonal winds u , meridional winds v , relative vorticity ζ , and vertical velocity at the top of the boundary layer w for the region $-25^{\circ} \leq \phi \leq 25^{\circ}$. The model runs are forced solely by the YOTC March 2010 monthly and 90W-150W zonally averaged 950 hPa pressure gradient force. Refer to the text for more details.

Overall, the slab boundary layer model high and low resolution runs are able to reproduce the gross dynamical features in the YOTC fields. The main differences are that the slab boundary layer model tends to produce stronger gradients, most likely due to its higher resolution (especially in sblm-hr). Our results emphasize the importance of resolving small scale features in order to improve the placement of the Ekman pumping and vorticity in the ITCZ.

5.8. CONCLUDING REMARKS

The structure of the boundary layer wind field near the ITCZ has been interpreted in terms of a zonally symmetric slab boundary layer model. The narrowness of the ITCZ has been explained by dry dynamics, i.e., by the formation of a shock in the boundary layer meridional flow, with northerly flow on the north edge of the shock and southerly flow on the south edge of the shock. Shock formation is associated with the $v(\partial v/a\partial\phi)$ term in the meridional momentum equation due to the presence of Burgers' equation. Since v is an order of magnitude larger in the boundary layer than in the overlying fluid (approximately 5 m s^{-1} versus 0.5 m s^{-1}), shocks are primarily a phenomenon of the boundary layer. The development of a shock in the boundary layer meridional wind v leads to a shock in the boundary layer zonal wind u , since $(\partial u/\partial t) = -v(\partial u/a\partial\phi) + \dots$, with large northerly flow ($v < 0$) producing a large easterly acceleration ($\partial u/\partial t < 0$) on the north edge of the shock and a large westerly acceleration ($\partial u/\partial t > 0$) on the south edge of the shock. A thin sheet of very high vorticity develops in the boundary layer, and it may extend upward due to vertical advection. Horizontal diffusion has been used here to avoid multivalued solutions near the shock. Although horizontal diffusion is a simple and effective way to avoid this problem, it is not the only way. Alternatively, a shock fitting procedure could be used, such as in the Fortran routines in the Conservation Laws Package (Clawpack) described by Leveque (2002).

For the boundary layer structures simulated here, we have chosen to use the terms "boundary layer shock" or "Burgers' shock," rather than the terms "bore" or "front." Our assumption of constant h obviously precludes the development of jumps in the boundary layer depth, so use of the term "bore" would be confusing. In addition, we have chosen to reserve the term "front" for structures that arise not from $v(\partial v/a\partial\phi)$, but rather from the combination of $v(\partial u/a\partial\phi)$, $w(\partial u/\partial z)$,

$v(\partial\theta/a\partial\phi)$, and $w(\partial\theta/\partial z)$, with the rotational flow u and the potential temperature θ being related by thermal wind balance. However, it should be noted that this distinction is not completely sharp, since the “boundary layer shocks” studied here depend not only on the $v(\partial v/a\partial\phi)$ term in the meridional equation of motion, but also on the $v(\partial u/a\partial\phi)$ term (or more generally on the $(2\Omega \sin \phi + \zeta)v$ term) in the zonal equation of motion, which leads to the shock-like structure in the u -field. Even with this caveat, it is helpful to use terminology that distinguishes features that can be accurately modeled using the geostrophic balance assumption (i.e., fronts) from features that cannot be modeled using geostrophic balance (i.e., boundary layer shocks).

The slab boundary layer model described in section 5.3 can be regarded as a model that is at or near the bottom of a hierarchy of boundary layer models of increasing complexity. Although the constant depth slab model does not capture certain important features found in height-resolving models of the tropical boundary layer, the constant depth slab model does appear to capture the essence of the shock structure in the meridional flow and its consequences for boundary layer pumping and subgeostrophic/supergeostrophic behavior in the zonal wind.

The phenomenon of ITCZ boundary layer shocks puts demanding horizontal resolution requirements on global NWP and climate models. These horizontal resolution requirements are as strict or even stricter than those for accurate simulation of moist convection. In view of the importance of boundary layer shocks in determining the location of diabatic heating, accurate ITCZ simulations probably require accurate simulations of such fine scale aspects of the boundary layer.

In closing we reiterate the conclusion that a boundary layer shock is one of the essential ingredients of the ITCZ. In fact, it could be said that the formation of a boundary layer shock is one of the most important events in the formation of a narrow ITCZ, for it imposes on the ITCZ a classic shock-like structure.

REFERENCES

- Arfken, G. B. and H. J. Weber, 1985: *Mathematical Methods for Physicists*. Academic, 832 pp.
- Back, L. E. and C. S. Bretherton, 2006: Geographic variability in the export of moist static energy and vertical motion profiles in the tropical Pacific. *Geophys. Res. Lett.*, **33**, L17 810.
- Back, L. E. and C. S. Bretherton, 2009a: A simple model of climatological rainfall and vertical motion patterns over the tropical oceans. *J. Clim.*, **22**, 6477–6497.
- Back, L. E. and C. S. Bretherton, 2009b: On the relationship between SST gradients, boundary layer winds and convergence over the tropical oceans. *J. Clim.*, **22**, 4182–4196.
- Blandford, R., 1966: Mixed gravity-Rossby waves in the ocean. *Deep-Sea Res.*, **13**, 941–961.
- Burgers, J., 1948: A mathematical model illustrating the theory of turbulence. *Adv. Appl. Mech.*, **1**, 171–199.
- Businger, S., R. McLaren, R. R. Ogasawara, D. Simons, and R. J. Wainscoat, 2002: Starcasting. *Bull. Amer. Meteor. Soc.*, **83**, 858–871.
- Cau, P., J. Methven, and B. J. Hoskins, 2007: Origins of dry air in the tropics and subtropics. *J. Clim.*, **20**, 2745–2759.
- Chao, W. C., 1987: On the origin of the tropical intraseasonal oscillation. *J. Atmos. Sci.*, **44**.
- Charney, J. G., 1968: The Intertropical Convergence Zone and the Hadley circulation of the atmosphere. *WMO/IUGG Symposium on Numerical Weather Prediction*, Tokyo, Japan, Japanese Meteorological Agency, III–73–III–79.
- Charney, J. G., 1971: Geostrophic turbulence. *J. Atmos. Sci.*, **28**, 1087–1095.
- Charney, J. G. and M. E. Stern, 1962: On the stability of internal baroclinic jets in a rotating atmosphere. *J. Atmos. Sci.*, **19**, 159–172.
- Courant, R. and D. Hilbert, 1953: *Methods of Mathematical Physics*. 22d ed., Interscience, 560 pp.
- Eliassen, A., 1951: Slow thermally or frictionally controlled meridional circulation in a circular vortex. *Astrophys. Norv.*, **5**, 19–60.
- Fulton, S. R., 1980: Geostrophic adjustment in a stratified atmosphere. M.S. thesis, Dep. Atmos. Sci., Colorado State University, 97 pp.
- Fulton, S. R. and W. H. Schubert, 1985: Vertical normal mode transforms: Theory and application. *Mon. Weather Rev.*, **113**, 647–658.

- Galewsky, J., A. Sobel, and I. Held, 2005: Diagnosis of subtropical humidity dynamics using tracers of last saturation. *J. Atmos. Sci.*, **62**, 3353–3367.
- Garcia, R. R., , and M. L. Salby, 1987: Transient response to localized episodic heating in the tropics. Part II: Far-field behavior. *J. Atmos. Sci.*, **44**, 499–532.
- Gill, A. E., 1980: Some simple solutions for heat-induced tropical circulation. *Q.J.R. Meteorol. Soc.*, **106**, 447–462.
- Gonzalez, A. O. and G. Mora Rojas, 2014: Balanced dynamics of deep and shallow Hadley circulations in the tropics. *J. Adv. Model. Earth Syst.*, **6**, 777–804.
- Gu, G., R. F. Adler, and A. H. Sobel, 2005: The eastern Pacific ITCZ during the boreal spring. *J. Atmos. Sci.*, **62**, 1157–1174.
- Hack, J. J. and W. H. Schubert, 1990: Some dynamical properties of idealized thermally-forced meridional circulations in the tropics. *Meteorol. Atmos. Phys.*, **44**, 101–117.
- Hack, J. J., W. H. Schubert, D. E. Stevens, and H.-C. Kuo, 1989: Response of the Hadley circulation to convective forcing in the ITCZ. *J. Atmos. Sci.*, **46**, 2957–2973.
- Hadley, G., 1735: Concerning the cause of the general trade winds. *Philos. Trans.*, **39**, 58.
- Haertel, P. T. and G. N. Kiladis, 2004: Dynamics of 2-Day equatorial waves. *J. Atmos. Sci.*, **61**, 27072721.
- Hagos, S. M., C. Zhang, S. L. W. K. Tao, Y. N. Takayabu, S. Shige, M. Katsumata, B. Olson, and T. S. L'Ecuyer, 2010: Estimates of tropical diabatic heating profiles: commonalities and uncertainties. *J. Clim.*, **23**, 542–558.
- Halley, E., 1686: An historical account of the trade winds, and monsoons, observable in the seas between and near the tropicks, with an attempt to assign the physical cause of the said winds. *Philos. Trans.*, **16**, 153.
- Hayes, S. P., M. J. McPhaden, and J. M. Wallace, 1989: The influence of sea surface temperature on surface wind in the eastern equatorial Pacific: Weekly to monthly variability. *J. Clim.*, **2**, 1500–1506.
- Haynes, P. H. and T. G. Shepherd, 1989: The importance of surface pressure changes in the response of the atmosphere to zonally-symmetric thermal and mechanical forcing. *Q. J. R. Meteorol. Soc.*, **115**, 1181–1208.
- Held, I. M. and A. Y. Hou, 1980: Nonlinear axially symmetric circulations in a nearly inviscid atmosphere. *J. Atmos. Sci.*, **37**, 515–533.

- Higgins, W. and Coauthors, 2006: The NAME 2004 field campaign and modeling strategy. *Bull. Amer. Meteor. Soc.*, **87**, 79–94.
- Holton, J. R., 1975: On the influence of boundary layer friction on mixed Rossby-gravity waves. *Tellus*, **27**, 107–115.
- Holton, J. R., J. M. Wallace, and J. A. Young, 1971: On boundary layer dynamics and the ITCZ. *J. Atmos. Sci.*, **28**, 275–280.
- Hoskins, B., 1996: On the existence and strength of the summer subtropical anticyclones - Bernhard Haurwitz memorial lecture. *Bull. Amer. Meteor. Soc.*, **77**, 1287–1292.
- Hou, A. Y. and R. S. Lindzen, 1992: The influence of concentrated heating on the Hadley circulation. *J. Atmos. Sci.*, **49**, 1233–1241.
- Hubert, L. F., A. F. Krueger, and J. S. Winston, 1969: The double Intertropical Convergence Zone—Fact or fiction? *J. Atmos. Sci.*, **26**, 771–773.
- Jackson, D. L. and J. J. Bates, 2001: Upper tropospheric humidity algorithm assessment. *J. Geophys. Res.*, **106**, 32 259–32 270.
- Large, W. G., J. C. McWilliams, and S. C. Doney, 1994: Oceanic vertical mixing: A review and a model with a nonlocal boundary layer parameterization. *Rev. Geophys.*, 32(4), 363–403.
- Leveque, R. J., 2002: *Finite Volume Methods for Hyperbolic Problems*. Cambridge University Press, 558 pp.
- Lietzke, C. E., C. Deser, and T. H. V. Haar, 2001: Evolutionary structure of the Eastern Pacific double ITCZ based on satellite moisture profile retrievals. *J. Clim.*, **14**, 743–751.
- Lindzen, R. S. and A. Y. Hou, 1988: Hadley circulations for zonally averaged heating centered off the equator. *J. Atmos. Sci.*, **45**, 2416–2427.
- Lindzen, R. S. and S. Nigam, 1987: On the role of sea surface temperature gradients in forcing low-level winds and convergence in the tropics. *J. Atmos. Sci.*, **44**, 2418–2436.
- Ling, J. and C. Zhang, 2013: Diabatic heating profiles in recent global analyses. *J. Clim.*, **23**, 3307–3325.
- Liu, W. T. and X. Xie, 2002: Double Intertropical Convergence Zones—a new look using scatterometer. *Geophys. Res. Lett.*, 29(22), 2072.
- Magnusdottir, G. and C.-C. Wang, 2008: Intertropical convergence zones during the active season in daily data. *J. Atmos. Sci.*, **65**, 2425–2436.

- Mahrt, L., 1972a: A numerical study of coupling between the boundary layer and free atmosphere in an accelerated low-latitude flow. *J. Atmos. Sci.*, **29**, 1485–1495.
- Mahrt, L., 1972b: A numerical study of the influence of advective accelerations in an idealized, low-latitude, planetary boundary layer. *J. Atmos. Sci.*, **29**, 1477–1484.
- Mapes, B. E., T. T. Warner, M. Xu, and A. J. Negri, 2003: Diurnal patterns of rainfall in northwestern South America. Part I: Observations and context. *Mon. Wea. Rev.*, **131**, 799–812.
- Masarik, M. T. and W. H. Schubert, 2013: Analytical solutions of the potential vorticity invertibility principle. *J. Adv. Model. Earth Syst.*, **5**, 366–381.
- McGauley, M., C. Zhang, and N. A. Bond, 2004: Large-scale characteristics of the atmospheric boundary layer in the eastern Pacific cold tongue-ITCZ Region. *J. Clim.*, **17**, 3907–3920.
- McNoldy, B. D., P. E. Ciesielski, W. H. Schubert, and R. H. Johnson, 2004: Surface winds, divergence, and vorticity in stratocumulus regions using ikSCAT and reanalysis winds. *Geophys. Res. Lett.*, **31**, 8.
- Mechoso, C. R. and Coauthors, 1995: The seasonal cycle over the tropical Pacific in coupled ocean-atmosphere general circulation models. *Mon. Wea. Rev.*, **123**, 2825–2838.
- Mitchell, T. P. and J. M. Wallace, 1992: The annual cycle in equatorial convection and sea surface temperature. *J. Clim.*, **5**, 1140–1156.
- Neelin, J. D. and I. M. Held, 1987: Modeling tropical convergence based on the moist static energy budget. *Mon. Wea. Rev.*, **115**, 3–12.
- Nieto Ferreira, R. and W. H. Schubert, 1997: Barotropic aspects of ITCZ breakdown. *J. Atmos. Sci.*, **54**, 251–285.
- Nolan, D. S., S. W. Powell, C. Zhang, and B. E. Mapes, 2010: Idealized simulations of the Intertropical Convergence Zone and its multilevel flows. *J. Atmos. Sci.*, **67**, 4028–4053.
- Nolan, D. S., C. Zhang, and S.-H. Chen, 2007: Dynamics of the shallow meridional circulation around Intertropical Convergence Zones. *J. Atmos. Sci.*, **64**, 2262–2285.
- Ooyama, K. V., 1997: Footnotes to “conceptual evolution”. Preprint Volume, *22nd Conf. on Hurricanes and Tropical Meteorology*, Fort Collins, Colorado, American Meteorological Society, 13–18.
- Pierrehumbert, R. T., 1998: Lateral mixing as a source of subtropical water vapor. *Geophys. Res. Lett.*, **25**, 151–154.
- Pierrehumbert, R. T. and R. Roca, 1998: Evidence for control of Atlantic subtropical humidity by large scale advection. *Geophys. Res. Lett.*, **25**, 4537–4540.

- Pike, A. C., 1971: The Inter-Tropical Convergence Zone studied with an interacting atmosphere ocean model. *Mon. Wea. Rev.*, **99**, 469–477.
- Pike, A. C., 1972: Response of a tropical atmosphere and ocean model to seasonally variable forcing. *Mon. Wea. Rev.*, **100**, 424–433.
- Raymond, D. J., C. S. Bretherton, and J. Molinari, 2006: Dynamics of the Intertropical Convergence Zone of the east Pacific. *J. Atmos. Sci.*, **63**, 582–597.
- Salathé, E. and D. Hartmann, 1997: A trajectory analysis of tropical upper-tropospheric moisture and convection. *J. Clim.*, **10**, 2533–2547.
- Salby, M. L. and R. R. Garcia, 1987: Transient response to localized episodic heating in the tropics. Part I: Excitation and short-time near-field behavior. *J. Atmos. Sci.*, **44**, 458–498.
- Schneider, E. K. and R. S. Lindzen, 1977: Axially symmetric steady-state models of the basic state for instability and climate studies. Part I. Linearized calculations. *J. Atmos. Sci.*, **67**, 4028–4053.
- Schreck, C. J., L. Shi, J. P. Kossin, and J. J. Bates, 2013: Identifying the MJO, equatorial waves, and their impacts using 32 years of HIRS upper-tropospheric water vapor. *J. Clim.*, **26**, 1418–1431.
- Schubert, W. H., P. E. Ciesielski, D. E. Stevens, and H.-C. Kuo, 1991: Potential vorticity modeling of the ITCZ and the Hadley circulation. *J. Atmos. Sci.*, **48**, 1493–1509.
- Schubert, W. H. and B. D. McNoldy, 2010: Axially symmetric steady-state models of the basic state for instability and climate studies. Part I. Linearized calculations. *J. Adv. Model. Earth Sys.*, **2**, 13.
- Schumacher, C., R. A. H. Jr., and I. Kraucunas, 2004: The tropical dynamical response to latent heating estimates derived from the TRMM Precipitation Radar. *J. Atmos. Sci.*, **61**, 1341–1358.
- Sherwood, S. C., E. R. Kursinski, and W. G. Read, 2006: A distribution law for free-tropospheric relative humidity. *J. Clim.*, 6267–6277.
- Shu, C. W. and S. Osher, 1988: Efficient implementation of essentially nonoscillatory shock-capturing schemes. *J. Comp. Phys.*, **77**, 439–471.
- Slocum, C. J., G. J. Williams, R. K. Taft, and W. H. Schubert, 2014: Tropical cyclone boundary layer shocks. Atmospheric and Oceanic Physics, *arXiv:1405.7939*, 19.
- Smith, B. and L. Mahrt, 1981: A study of boundary-layer pressure adjustments. *J. Atmos. Sci.*, **38**, 334–346.

- Smith, T. M., R. Reynolds, T. Peterson, and J. Lawrimore, 2008: Improvements to NOAA's historical merged land-ocean surface temperature analysis. *J. Clim.*, **21**, 2283–2296.
- Sobel, A. H. and J. D. Neelin, 2006: The boundary layer contribution to intertropical convergence zones in the quasi-equilibrium tropical circulation model framework. *Theor. Comput. fluid dyn.*, doi:10.1007/s00162-006-0033-y.
- Soden, B. J. and F. P. Bretherton, 1993: Upper tropospheric relative humidity from the GOES 6.7 μm channel: Method and climatology for July 1987. *J. Geophys. Res.*, **98**, 16 669–16 688.
- Soden, B. J. and F. P. Bretherton, 1996: Interpretation of TOVS water vapor radiances in terms of layer-average relative humidities: Method and climatology for the upper, middle, and lower troposphere. *J. Geophys. Res.*, **101**, 9333–9343.
- Soden, B. J. and R. Fu, 1995: A satellite analysis of deep convection, upper-tropospheric humidity, and greenhouse effect. *J. Clim.*, **8**, 2333–2351.
- Stevens, B., J. Duan, J. C. McWilliams, M. Mnich, and J. D. Neelin, 2002: Entrainment, Rayleigh friction, and boundary layer winds over the tropical Pacific. *J. Clim.*, **15**, 30–44.
- Sun, D.-Z. and R. Lindzen, 1993: Distribution of tropical tropospheric water vapor. *J. Atmos. Sci.*, **50**, 1643–1660.
- Takayabu, Y. N., 1994: Large-scale cloud disturbances associated with equatorial waves. Part II: Westward-propagating inertia-gravity waves. *J. Meteor. Soc. Japan*, **72**, 451–465.
- Takayabu, Y. N., S. Shige, W.-K. Tao, and N. Hirota, 2010: Shallow and deep latent heating modes over tropical oceans observed with TRMM PR spectral latent heating data. *J. Clim.*, **23**, 2030–2046.
- Tomas, R. A., J. R. Holton, and P. J. Webster, 1999: The influence of cross-equatorial pressure gradients on the location of near-equatorial convection. *Q. J. R. Meteorol. Soc.*, **125**, 1107–1127.
- Tomas, R. A. and P. J. Webster, 1997: The role of inertial instability in determining the location and strength of near-equatorial convection. *Q. J. R. Meteorol. Soc.*, **123**, 1445–1482.
- Trenberth, K. E., D. P. Stepaniak, and J. M. Caron, 1997: The global monsoon as seen through the divergent atmospheric circulation. *J. Clim.*, **13**, 3969–3993.
- Waliser, D. E. and Coauthors, 2012: The Year of Tropical Convection (May 2008–April 2010): climate variability and weather highlights. *Bull. Amer. Meteor. Soc.*, **93**, 1189–1218.
- Wang, B. and H. Rui, 1990: Dynamics of the coupled moist Kelvin-Rossby wave on an equatorial β -plane. *J. Atmos. Sci.*, **47**, 397–413.

- Wang, C.-C. and G. Magnusdottir, 2005: ITCZ breakdown in three-dimensional flows. *J. Atmos. Sci.*, **62**, 1497–1512.
- Wang, C.-C. and G. Magnusdottir, 2006: The ITCZ in the central and eastern Pacific on synoptic time scales. *Mon. Weather Rev.*, **134**, 1405–1421.
- Webster, P. J. and J. R. Holton, 1982: Cross-equatorial response to middle-latitude forcing in a zonally varying basic state. *J. Atmos. Sci.*, **39**, 722–733.
- Whitham, G. B., 1974: *Linear and Nonlinear Waves*. John Wiley, New York, 636 pp.
- Williams, G. J., W. H. Schubert, and R. K. Taft, 2013: Shock-like structures in the tropical cyclone boundary layer. *J. Adv. Model. Earth Sys.*, **5**, 338–353.
- Wu, Z., E. S. Sarachik, and D. S. Battisti, 2000: Vertical structure of convective heating and the three-dimensional structure of the forced circulation on an equatorial beta plane. *J. Atmos. Sci.*, **57**, 2169–2187.
- Wunsch, C. and A. E. Gill, 1976: Observations of equatorially trapped waves in Pacific sea level variations. *Deep-Sea Res.*, **23**, 371–390.
- Yamasaki, M., 1971: Frictional convergence in Rossby waves in low latitudes. *J. Meteor. Soc.*, **49**, 691–698.
- Yanai, M., S. K. Esbensen, and J. Chu, 1973: Determination of bulk properties of tropical cloud clusters from large-scale heat and moisture budgets. *J. Atmos. Sci.*, **30**, 611–627.
- Yin, B. and B. A. Albrecht, 2000: Spatial variability of atmospheric boundary layer structure over the eastern equatorial Pacific. *J. Clim.*, **13**, 1574–1592.
- Yokoyama, C., E. J. Zipser, and C. Liu, 2014: TRMM shallow versus deep convection in the eastern Pacific related to large scale circulations in reanalyses. *J. Clim.*, **27**, 5575–5592.
- Zhang, C., 2001: Double ITCZs. *J. Geophys. Res.*, 106(D11), 11 785–11 792.
- Zhang, C. and S. M. Hagos, 2009: Bi-modal structure and variability of large-scale diabatic heating in the tropics. *J. Atmos. Sci.*, **66**, 3621–3640.
- Zhang, C., M. McGauley, and N. A. Bond, 2004: Shallow meridional circulation in the tropical eastern Pacific. *J. Clim.*, **17**, 133–139.
- Zhang, C., D. S. Nolan, C. D. Thorncroft, and H. Nguyen, 2008: Shallow meridional circulations in the tropical atmosphere. *J. Clim.*, **21**, 3453–3470.

APPENDIX A

Vertical transform

The mathematical principles underlying the vertical transform pair (2.21) and (2.22) are the orthonormality and completeness of the eigenfunctions $\mathcal{Z}_m(z)$. Consider the eigenfunction $\mathcal{Z}_m(z)$, which is a solution of (2.23)–(2.23), and the eigenfunction $\mathcal{Z}_{m'}(z)$, which is a solution of (2.23)–(2.25) with m replaced by m' . To obtain the orthonormality relation, we multiply the equation for $\mathcal{Z}_m(z)$ by $\mathcal{Z}_{m'}(z)$, then multiply the equation for $\mathcal{Z}_{m'}(z)$ by $\mathcal{Z}_m(z)$, and finally integrate the difference of the resulting equations to obtain

$$\begin{aligned} & \frac{1}{g} \left(\frac{1}{h_m} - \frac{1}{h_{m'}} \right) \int_0^{z_T} \mathcal{Z}_m(z) \mathcal{Z}_{m'}(z) N^2(z) dz \\ & + \left[\mathcal{Z}_{m'}(z) \frac{d\mathcal{Z}_m(z)}{dz} - \mathcal{Z}_m(z) \frac{d\mathcal{Z}_{m'}(z)}{dz} \right]_0^{z_T} = 0. \end{aligned} \tag{A.1}$$

The second line in (A.1) can be evaluated with the aid of the boundary conditions (2.24) and (2.25). Then, for distinct eigenvalues ($h_m \neq h_{m'}$) and for normalized $\mathcal{Z}_m(z)$, there is an orthonormality relation

$$\begin{aligned} & \frac{1}{g} \int_0^{z_T} \mathcal{Z}_m(z) \mathcal{Z}_{m'}(z) N^2(z) dz + \mathcal{Z}_m(0) \mathcal{Z}_{m'}(0) \\ & = \begin{cases} 1 & \text{if } m = m' \\ 0 & \text{if } m \neq m'. \end{cases} \end{aligned} \tag{A.2}$$

To confirm that (2.21) is the proper transform for the expansion (2.22), we multiply (2.22) by $\mathcal{Z}_{m'}(z)N^2(z)$ and then integrate over z to obtain

$$\begin{aligned} & \int_0^{z_T} \hat{\psi}(y, z) \mathcal{Z}_{m'}(z) N^2(z) dz \\ &= \sum_{m=0}^{\infty} \hat{\psi}_m(y) \int_0^{z_T} \mathcal{Z}_m(z) \mathcal{Z}_{m'}(z) N^2(z) dz. \end{aligned} \quad (\text{A.3})$$

Similarly, we multiply (2.22), evaluated at $z = 0$, by $\mathcal{Z}_{m'}(0)$ to obtain

$$\hat{\psi}(y, 0) \mathcal{Z}_{m'}(0) = \sum_{m=0}^{\infty} \hat{\psi}_m(y) \mathcal{Z}_m(0) \mathcal{Z}_{m'}(0). \quad (\text{A.4})$$

Multiplying (A.3) by $1/g$, adding the result to (A.4), and then using the orthonormality relation (A2), (2.21) is obtained, confirming the validity of the transform pair (2.21) and (2.22).

To prove that all the eigenvalues of the problem (2.23)–(2.25) are positive, we multiply (2.23) by $\mathcal{Z}_m(z)$ to obtain

$$\frac{N^2 \mathcal{Z}_m^2}{gh_m} + \frac{d}{dz} \left(\mathcal{Z}_m \frac{d\mathcal{Z}_m}{dz} \right) = \left(\frac{d\mathcal{Z}_m}{dz} \right)^2 + \left(\frac{\mathcal{Z}_m}{2H} \right)^2. \quad (\text{A.5})$$

Integrating (A.5) over z and making use of the boundary conditions (2.24) and (2.25) results in

$$\begin{aligned} & \frac{1}{h_m} \left\{ \frac{1}{g} \int_0^{z_T} \mathcal{Z}_m^2(z) N^2(z) dz + \mathcal{Z}_m^2(0) \right\} \\ &= \int_0^{z_T} \left\{ \left(\frac{d\mathcal{Z}_m(z)}{dz} \right)^2 + \left(\frac{\mathcal{Z}_m(z)}{2H} \right)^2 \right\} dz + \frac{\mathcal{Z}_m^2(0)}{2H}. \end{aligned} \quad (\text{A.6})$$

The right hand side of (A.6) is positive. Since $N^2 > 0$, the term in braces on the left hand side of (A.6) is also positive. Thus, all the eigenvalues are positive, i.e., $h_m > 0$ for all m .

To determine if the eigenfunctions $\mathcal{Z}_m(z)$ form a complete set, we first write (2.21) in the form

$$\hat{\psi}_m(y) = \frac{1}{g} \int_0^{z_T} [1 + \delta(z')] \hat{\psi}(y, z') \mathcal{Z}_m(z') N^2(z') dz', \quad (\text{A.7})$$

where $\delta(z')$ satisfies

$$\frac{1}{g} \int_0^{z_T} \delta(z') N^2(z') dz' = 1. \quad (\text{A.8})$$

Using (A.7) in (2.22) results in

$$\begin{aligned} \hat{\psi}(y, z) = \\ \frac{1}{g} \int_0^{z_T} \left\{ [1 + \delta(z')] \sum_{m=0}^{\infty} \mathcal{Z}_m(z) \mathcal{Z}_m(z') \right\} \hat{\psi}(y, z') N^2(z') dz'. \end{aligned} \quad (\text{A.9})$$

The right hand side of (A.9) evaluates to $\hat{\psi}(y, z)$ if

$$[1 + \delta(z')] \sum_{m=0}^{\infty} \mathcal{Z}_m(z') \mathcal{Z}_m(z) = \delta(z' - z), \quad (\text{A.10})$$

which is the completeness relation. Although a general proof of (A.7) is not given, it is confirmed numerically for the special case of constant N in Appendix B. For further discussion, see section 8.4 of Arfken and Weber (1985) and section 6.3 of Courant and Hilbert (1953).

APPENDIX B

Calculation of h_m and $\mathcal{Z}_m(z)$

To solve the Sturm-Liouville problem (2.23)–(2.25), consider the idealized case in which the buoyancy frequency N is a constant given by $N = 1.2 \times 10^{-2} \text{ s}^{-1}$. The solution of the second order equation (2.23) has different forms depending on the eigenvalues h_m . We begin by exploring the possibility that one of the eigenvalues is given by \hat{h} , which is defined by $\hat{h} = (2NH)^2/g = 4328 \text{ m}$. The corresponding eigenfunction $\hat{\mathcal{Z}}(z)$ then satisfies $d^2\hat{\mathcal{Z}}/dz^2 = 0$, in which case the solution satisfying the upper boundary condition (2.24) is $\hat{\mathcal{Z}}(z) = C(z_T - z)$, where C is a constant. The lower boundary condition is satisfied if $\{1 + z_T[(1/H) - (1/\hat{h})]\}C = 0$. We assume that the constant z_T is specified in such a way that $z_T \neq [(1/\hat{h}) - (1/H)]^{-1} = 8731 \text{ m}$, so that $1 + z_T[(1/H) - (1/\hat{h})] \neq 0$ and $C = 0$, meaning that the boundary value problem does not have a nontrivial eigenfunction with corresponding eigenvalue $h_m = \hat{h}$. Below, the two cases are investigated separately: $h_m > \hat{h}$ (Case 1) and $0 < h_m < \hat{h}$ (Case 2). The solutions involve solving a transcendental equation using Newton's iterative method for h_m .

Case 1. If the eigenvalues satisfy $h_m > \hat{h}$, then the equation for $\mathcal{Z}_m(z)$ is

$$\frac{d^2\mathcal{Z}_m(z)}{dz^2} - \frac{\mu_m^2}{z_T^2}\mathcal{Z}_m = 0, \quad (\text{B.1})$$

where

$$\frac{\mu_m^2}{z_T^2} = \frac{N^2}{g} \left(\frac{1}{\hat{h}} - \frac{1}{h_m} \right) > 0. \quad (\text{B.2})$$

In this case the vertical structure functions satisfying the upper boundary condition are

$$\mathcal{Z}_m(z) = A_m \sinh[\mu_m(1 - z/z_T)], \quad (\text{B.3})$$

where A_m is the normalization factor. Through application of the lower boundary condition (2.25), it can be shown that μ_m is the solution of

$$\tanh(\mu_m) = \frac{\mu_m}{(z_T/\hat{h})[1 - \hat{h}/2H - (2H\mu_m/z_T)^2]}. \quad (\text{B.4})$$

The transcendental equation (B.4) has only one solution, denoted by μ_0 and having the value $\mu_0 = 0.4686$. The corresponding eigenvalue h_0 is obtained from (B2), written in the form

$$h_0 = \hat{h} [1 - (2H\mu_0/z_T)^2]^{-1} \approx 7075 \text{ m}. \quad (\text{B.5})$$

The top line in the orthonormality relation (A2) is satisfied if the normalization factor is given by

$$A_0 = \left\{ \frac{N^2 z_T}{2g} \left[\frac{\sinh(\mu_0) \cosh(\mu_0)}{\mu_0} - 1 \right] + \sinh^2(\mu_0) \right\}^{-1/2}. \quad (\text{B.6})$$

Case 2. If the eigenvalues lie in the range $0 < h_m < \hat{h}$, then the equation for $\mathcal{Z}_m(z)$ is

$$\frac{d^2 \mathcal{Z}_m(z)}{dz^2} + \frac{\nu_m^2}{z_T^2} \mathcal{Z}_m = 0, \quad (\text{B.7})$$

where

$$\frac{\nu_m^2}{z_T^2} = \frac{N^2}{g} \left(\frac{1}{h_m} - \frac{1}{\hat{h}} \right) > 0. \quad (\text{B.8})$$

In this case the vertical structure functions satisfying the upper boundary condition are

$$\mathcal{Z}_m(z) = B_m \sin[\nu_m(1 - z/z_T)], \quad (\text{B.9})$$

where B_m is the normalization factor. Through application of the lower boundary condition (2.25), it can be shown that ν_m is the solution of

$$\tan(\nu_m) = \frac{\nu_m}{(z_T/\hat{h})[1 - \hat{h}/2H + (2H\nu_m/z_T)^2]}. \quad (\text{B.10})$$

After the transcendental equation (B.10) is solved for ν_m , the eigenvalues h_m can be obtained from (B.8), written in the form

$$h_m = \hat{h} [1 + (2H\nu_m/z_T)^2]^{-1} \approx \hat{h} [1 + (2Hm\pi/z_T)^2]^{-1}. \quad (\text{B.11})$$

The second (approximate) equality follows from the fact that the solutions of the transcendental equation (B.10) are approximately $\nu_m \approx m\pi$ for $m = 1, 2, \dots$, with the accuracy of the estimate improving as m increases. The exact and approximate eigenvalues are listed in Table 2.1. Finally, the top line in the orthonormality relation (A2) is satisfied if the normalization factor is given by

$$B_m = \left\{ \frac{N^2 z_T}{2g} \left[1 - \frac{\sin(\nu_m) \cos(\nu_m)}{\nu_m} \right] + \sin^2(\nu_m) \right\}^{-1/2}. \quad (\text{B.12})$$

Note that the dependence of the normalization factors B_m on m is weak because $\nu_m \approx m\pi$, making the $\sin(\nu_m)$ terms in (B.12) negligible, which leads to $B_m \approx [2g/(N^2 z_T)]^{1/2} \approx 3.2$.

To summarize, the eigenvalue for the external mode is given by (B.5) where μ_0 is the single solution of the transcendental equation (B4), while the eigenvalues for the internal modes are given by (B.11) where ν_m are the solutions of the transcendental equation (B.10). The corresponding

eigenfunctions are

$$\mathcal{Z}_m(z) = \begin{cases} A_0 \sinh[\mu_0(1 - z/z_T)] & m = 0 \\ B_m \sin[\nu_m(1 - z/z_T)] & m \geq 1, \end{cases} \quad (\text{B.13})$$

where the normalization factors are given by (B.6) and (B.12). The first five eigenvalues h_m ($m = 0, 1, 2, 3, 4$) are listed in Table 2.1, while the corresponding eigenfunctions are plotted in Fig. 2.2.

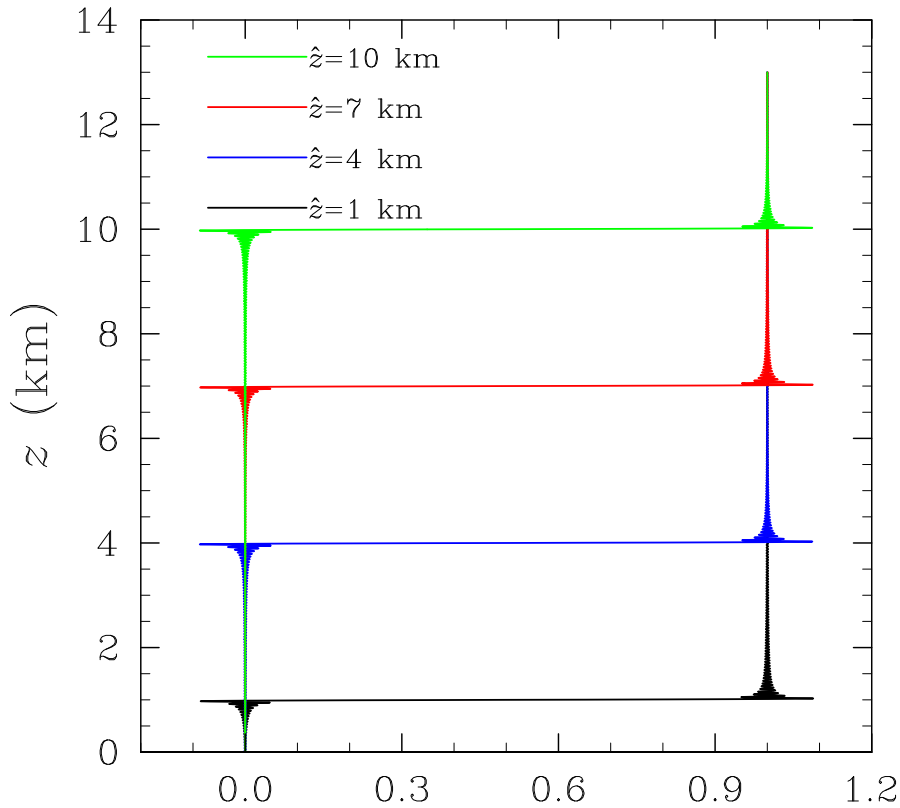


FIG. B.1. Four plots of the left hand side of (B.15) for the choices $\hat{z} = 1$ km (black), $\hat{z} = 4$ km (blue), $\hat{z} = 7$ km (red), and $\hat{z} = 10$ km (green). The two sums on the left hand side of (B.15) have been truncated at $m = 500$. These plots, and others with different truncations, demonstrate that the left hand side of (B.15) converges in the mean to the right hand side of (B.15), thereby confirming the completeness of the basis functions $\mathcal{Z}_m(z)$ for the case of constant N .

To numerically confirm the completeness relation (A10) for the case of constant N , first we write it in the form

$$\begin{aligned}
& [1 + \delta(z')] \mathcal{Z}_0(z') \mathcal{Z}_0(\hat{z}) \\
& + [1 + \delta(z')] \sum_{m=1}^{\infty} \mathcal{Z}_m(z') \mathcal{Z}_m(\hat{z}) = \delta(z' - \hat{z}),
\end{aligned} \tag{B.14}$$

where, for notational convenience, \hat{z} replaces z . The numerical confirmation of (B.14) is simpler if (B.14) is converted to an integrated form because then the two delta functions will not appear. Thus, integrating (B.14) over z' from zero to z , making use of (B.13), and finally multiplying by N^2/g results in

$$\begin{aligned}
& \frac{A_0 N^2 z_T}{g \mu_0} \mathcal{Z}_0(\hat{z}) \{ \cosh(\mu_0) - \cosh[\mu_0(1 - z/z_T)] \} \\
& + \sum_{m=1}^{\infty} \frac{B_m N^2 z_T}{g \nu_m} \mathcal{Z}_m(\hat{z}) \{ \cos[\nu_m(1 - z/z_T)] - \cos(\nu_m) \} \\
& + \sum_{m=0}^{\infty} \mathcal{Z}_m(0) \mathcal{Z}_m(\hat{z}) = \begin{cases} 1 & \text{if } z > \hat{z} \\ 0 & \text{if } z < \hat{z}. \end{cases}
\end{aligned} \tag{B.15}$$

Figure B.1 shows plots of the left hand side of (B.15) when $\hat{z} = 1, 4, 7, 10$ km and when 500 terms are used in the summation over m . Plots similar to Fig. B.1, but for different truncations of the sums, confirm that, although the Gibbs phenomenon occurs near $z = \hat{z}$, the left hand side of (B.15) converges (in the mean) to the unit step function as the number of terms is increased. This is numerical confirmation that (B.14) is valid and therefore that the basis functions (B.13) form a complete set in the special case of constant N .

APPENDIX C

Characteristic form

Equations (5.1)–(5.5) constitute a quasi-linear first order system, i.e., the system is linear in the first derivatives but the coefficients of these derivatives are functions of the dependent variables u and v . In the absence of the horizontal diffusion terms, these equations constitute a hyperbolic system, which means that it can be rewritten in characteristic form. Knowledge of the characteristic form allows for a deeper understanding of the way that characteristics can intersect and thereby produce discontinuities in u and v and singularities in w and ζ . To derive the characteristic form we shall rearrange (5.1) and (5.2) in such a way that all the terms involving the derivatives $(\partial u/\partial t)$, $(\partial u/a\partial\phi)$, $(\partial v/\partial t)$, $(\partial v/a\partial\phi)$ appear on the left-hand sides and all the other terms appear on the right-hand sides. This procedure requires splitting the w terms. In regions where $w \geq 0$, the w terms in (5.1) and (5.2) vanish. In regions where $w < 0$, the w terms do not vanish, in which case these terms need to be expressed in terms of $(\partial v/a\partial\phi) - (v \tan \phi)/a$, and then the $(\partial v/a\partial\phi)$ parts need to be kept on the left-hand sides of (5.1) and (5.2) while the $(v \tan \phi)/a$ parts need to be brought over to the right-hand sides. This procedure is easily accomplished by noting that the mass continuity equation in (5.3) yields

$$w = -h \left(\frac{\partial v}{a\partial\phi} - \frac{v \tan \phi}{a} \right) \quad (\text{C.1})$$

which allows (5.1) and (5.2) to be written in the form

$$\frac{\partial u}{\partial t} + v \frac{\partial u}{a\partial\phi} + (1 - \alpha)(u - u_g) \frac{\partial v}{a\partial\phi} = F_1, \quad (\text{C.2})$$

$$\frac{\partial v}{\partial t} + (2 - \alpha)v \frac{\partial v}{a \partial \phi} = F_2, \quad (\text{C.3})$$

where

$$F_1 = \frac{(1 - \alpha)(u - u_g)v \tan \phi}{a} + \left(2\Omega \sin \phi + \frac{u \tan \phi}{a} \right) v - c_D U \frac{u}{h}, \quad (\text{C.4})$$

$$F_2 = \frac{(1 - \alpha)v^2 \tan \phi}{a} - \left(2\Omega \sin \phi + \frac{u \tan \phi}{a} \right) u - \frac{1}{\rho} \frac{\partial p}{a \partial \phi} - c_D U \frac{v}{h}. \quad (\text{C.5})$$

The forms (C.2) and (C.3) are convenient because the nonlinearities associated with spatial derivatives are on the left-hand side while all the other linear and nonlinear terms are on the right-hand side. The classification of the system (C.2) and (C.3) as a hyperbolic system and the determination of the characteristic form of this system depends on finding the eigenvalues and left eigenvectors of the matrix A , which is defined by

$$A = \begin{pmatrix} v & (1 - \alpha)(u - u_g) \\ 0 & (2 - \alpha)v \end{pmatrix} \quad (\text{C.6})$$

(see Chapter 5 of Whitham (1974)). Note that the matrix A is composed of the coefficients of the $(\partial u / a \partial \phi)$ and $(\partial v / a \partial \phi)$ terms on the left-hand sides of (C.2) and (C.3). For $n = 1, 2$, let $(\ell_1^{(n)} \ell_2^{(n)})$ be the left eigenvector of A corresponding to the eigenvalue $\lambda^{(n)}$, i.e.,

$$(\ell_1^{(n)} \ell_2^{(n)}) \begin{pmatrix} v & (1 - \alpha)(u - u_g) \\ 0 & (2 - \alpha)v \end{pmatrix} = \lambda^{(n)} (\ell_1^{(n)} \ell_2^{(n)}). \quad (\text{C.7})$$

As is easily checked by direct substitution into (C.7), the two eigenvalues and the two corresponding left eigenvectors are

$$\begin{aligned}\lambda^{(1)} = v &\iff \ell_1^{(1)} = -v, \ell_2^{(1)} = u - u_g, \\ \lambda^{(2)} = (2 - \alpha)v &\iff \ell_1^{(2)} = 0, \ell_2^{(2)} = 1.\end{aligned}\tag{C.8}$$

Since the eigenvalues $\lambda^{(1)}$ and $\lambda^{(2)}$ are real and the corresponding left eigenvectors are linearly independent, the system (C.2)–(C.3) is hyperbolic and can be rewritten in characteristic form. To obtain this characteristic form, we next take the sum of $\ell_1^{(n)}$ times (C.2) and $\ell_2^{(n)}$ times (C.3) to obtain

$$\ell_1^{(n)} \left\{ \frac{\partial u}{\partial t} + v \frac{\partial u}{a \partial \phi} \right\} + \ell_2^{(n)} \left\{ \frac{\partial v}{\partial t} + \left[(2 - \alpha)v + (1 - \alpha)(u - u_g) \frac{\ell_1^{(n)}}{\ell_2^{(n)}} \right] \frac{\partial v}{a \partial \phi} \right\} = \ell_1^{(n)} F_1 + \ell_2^{(n)} F_2.\tag{C.9}$$

Using the eigenvector components given in (C.8), equation (C.9) becomes (for $n = 1$ and $n = 2$)

$$v \left(\frac{\partial u}{\partial t} + v \frac{\partial u}{a \partial \phi} \right) - (u - u_g) \left(\frac{\partial v}{\partial t} + v \frac{\partial v}{a \partial \phi} \right) = v F_1 - (u - u_g) F_2,\tag{C.10}$$

$$\frac{\partial v}{\partial t} + (2 - \alpha)v \frac{\partial v}{a \partial \phi} = F_2.\tag{C.11}$$

Since (C.11) is identical to (C.3), we conclude that (C.3) is already in characteristic form. We now write (C.10) and (C.11) in the form

$$v \frac{du}{dt} - (u - u_g) \frac{dv}{dt} = v F_1 - (u - u_g) F_2 \quad \text{on} \quad a \frac{d\phi}{dt} = v,\tag{C.12}$$

$$\frac{dv}{dt} = F_2 \quad \text{on} \quad a \frac{d\phi}{dt} = (2 - \alpha)v.\tag{C.13}$$

Equations (C.12) and (C.13) constitute the characteristic form of the original system (C.2) and (C.3). An advantage of (C.12) and (C.13) is that, along each family of characteristic curves, the partial differential equations have been reduced to ordinary differential equations. It is interesting to note that, in regions of subsidence (i.e., where $\alpha = 0$), information on v is carried along characteristics given by $a(d\phi/dt) = 2v$, while information on a combination of u and v is carried along characteristics given by $a(d\phi/dt) = v$. Thus, in regions of subsidence there are two distinct families of characteristics. In contrast, for regions of boundary layer pumping (i.e., where $\alpha = 1$), the two families of characteristics become identical.

Although in practice the forcing terms F_1 and F_2 are too complicated to allow analytical solution of (C.12) and (C.13), the numerical solution of these ordinary differential equations can serve as the basis of the shock-capturing methods described by Leveque (2002). In sections 5.6 and 5.7 we have adopted the simpler approach of solving (5.1)–(5.3) using standard finite differences with the inclusion of horizontal diffusion to control the solution near shocks. Although this approach has some disadvantages (e.g., unphysical oscillation near a shock), it provides a useful guide to the expected results when full-physics hurricane models can be run at the high horizontal resolution used here.

In regions where $w < 0$, we have $\alpha = 0$ and the characteristic forms (C.12) and (C.13) distinguish two families of characteristics, one given by $a(d\phi/dt) = v$ and one given by $a(d\phi/dt) = 2v$. In regions where $w \geq 0$, we have $\alpha = 1$ and there is only one family of characteristics, given by $a(d\phi/dt) = v$. In that case, (C.13) can be used to eliminate (dv/dt) in (C.12), which leads to the conclusion that $(du/dt) = F_1$ and $(dv/dt) = F_2$ on $a(d\phi/dt) = v$. This case of only one family of characteristics is the one explored analytically in sections 3 and 4, with the forcing terms F_1 and

F_2 set to zero in section 3, and with these forcing terms representing linear surface drag in section 4.

In passing we note that there is a less formal, more intuitive route from (C.2) and (C.3) to the characteristic forms (C.12) and (C.13). This intuitive route results from simply noting that (C.3) is already in characteristic form and can be directly written as (C.13), while the characteristic form (C.12) can be simply obtained by combining (C.2) and (C.3) in such a way as to eliminate terms containing the factor $(1 - \alpha)(\partial v/a\partial\phi)$.